Applications of nonlinear magneto-photonics at the nanoscale

Ngoc Minh Tran

UNIVERSITE MATIERE BRETAGNE MOLECULES LOIRE ET MATERIAUX

Le Mans Université

THESE DE DOCTORAT DE

LE MANS UNIVERSITE
COMUE UNIVERSITE BRETAGNE LOIRE

ECOLE DOCTORALE N° 596
Matière Molécules et Matériaux
Spécialité : *Ondes et Matériaux*

Par

Ngoc Minh TRAN

Applications of nonlinear magneto-photonics at the nanoscale

Thèse présentée et soutenue au Mans, le 13 décembre 2018
Unité de recherche : Institut des Molécules et Matériaux du Mans (IMMM) – Le Mans Université
Thèse N° : 2018LEMA1029

Rapporteurs avant soutenance :

Michael Farle	Prof., Universität Duisburg-Essen
Peter Gaal	Prof., INF - Universität Hamburg

Composition du Jury :

Michael Farle	Prof., Universität Duisburg-Essen
Peter Gaal	Prof., INF - Universität Hamburg
Ulrike Woggon	Prof., IOAP - Technische Universität Berlin
Béatrice Dagens	DR, C2N - Université Paris-Saclay
Directeur de thèse	
Vasily Temnov	CNRS CRCN, IMMM CNRS 6283
Encadrant de thèse	
Gwenaëlle Vaudel	CNRS IR1, IMMM CNRS 6283

UNIVERSITE MATIERE BRETAGNE MOLECULES LOIRE ET MATERIAUX

Le Mans Université

Titre : Application de la magneto-photonique non-linéaire à l'échelle nanométrique

Mots clés : magneto-plasmonique, génération de seconde harmonique, nanostructures hybrides métal/ferromagnétiques, géométrie Kretschmann, réseaux de diffraction magnétique, modèles phénoménologiques d'optique non-linéaire.

Résumé : La génération de seconde harmonique magnétique (mSHG pour magnetic Second Harmonic Generation) est un phénomène physique très sensible apparaissant grâce aux brisures de symétrie aux niveaux des surfaces et interfaces des structures métalliques magnétiques. Elle constitue donc un outil puissant pour explorer ce type d'interfaces et des nanostructures. Dans ce travail, nous nous intéressons aux couplages et interactions entre la mSHG et les ondes électromagnétiques pouvant se propager en surface des matériaux. Un intérêt spécifique est porté sur l'excitation de (i) plasmon polaritons de surfaces (SPP) dans des films métalliques en structures multicouches, (ii) d'anomalies de diffraction (dîtes de Wood) dans des nanostructures métalliques périodiques. Pour étudier l'influence de l'excitation linéaire et non-linéaire des SPP sur la mSHG, l'intensité du signal réfléchi par génération de seconde harmonique (SH) et le contraste magnétique lié à ce signal ont été mesurés par la technique de l'effet Kerr magnéto-optique transverse (MOKE) en fonction de l'angle d'incidence. Via l'utilisation de sources lasers femtosecondes émettant dans le proche infrarouge, domaine spectral où les variations de la dispersion des SPP et du coefficient d'amortissement sont significatives, nous avons pu distinguer les différentes contributions linéaires et non-linéaires aux processus d'excitation. Ce travail de thèse a ainsi permis de montrer que l'accord de phase entre la mSHG et les ondes électromagnétiques de surface peuvent contribuer très efficacement à l'augmentation des signaux SH et de contraste magnétique associé. Ces résultats sont très importants pour le contrôle de la réponse non-linéaire magnéto-optique des matériaux et peuvent trouver leurs applications dans le développement de composants pour le stockage magnétique des données, de biocapteurs sans marquage, ou de bascules magnéto-optiques non-linéaires.

Title : Applications of nonlinear magneto-photonics at the nanoscale

Keywords : magneto-plasmonics, magnetic second harmonic generation, hybrid metal-ferromagnet nanostructures, magnetic diffractions gratings, Kretschmann configuration, phenomenological models in nonlinear optics.

Abstract : Owing to surface and interface sensitivity, the magnetic Second Harmonic Generation (mSHG) represents a useful tool to probe magnetic interfaces and nanostructures. This work investigates the coupling and interaction of the mSHG with electromagnetic waves propagating along the surface. Two types of surface waves have been studied: (i) surface plasmon polaritons (SPP) at surfaces of metallic thin films and multilayers, and (ii) the diffraction anomaly at the surface of periodically arranged metallic nanostructures. To study influence of linear and nonlinear excitation of surface waves on the mSHG, the reflected second harmonic (SH) intensity and the magnetic SH contrast in the transverse magneto-optical geometry were measured as a function of the angle of incidence. The use of different femtosecond light sources in the near-infrared optical range, where the SPP dispersion and damping exhibit significant variations, made it possible to disentangle linear and nonlinear contributions to the excitation of surface waves. In this thesis, it is proven that phase-matching of the mSHG and surface electromagnetic waves can lead to the enhancement of both the SH yield and the nonlinear magneto-optical signal. These results are important for controlling of the nonlinear magneto-optical response and could impact the development of magnetic storage devices, label-free biosensors and nonlinear magneto-optical switches.

Abstract

Owing to surface and interface sensitivity, the magnetic Second Harmonic Generation (mSHG) represents a useful tool to probe magnetic interfaces and nanostructures. This work investigates the coupling and interaction of the mSHG with electromagnetic waves propagating along the surface. Two types of surface waves have been studied: (i) surface plasmon polaritons (SPP) at surfaces of metallic thin films and multilayers, and (ii) the diffraction anomaly at the surface of periodically arranged metallic nanostructures. To study influence of linear and nonlinear excitation of surface waves on the mSHG, the reflected second harmonic (SH) intensity and the magnetic SH contrast in the transverse magneto-optical geometry were measured as a function of the angle of incidence. The use of different femtosecond light sources in the near-infrared optical range, where the SPP dispersion and damping exhibit significant variations, made it possible to disentangle linear and nonlinear contributions to the excitation of surface waves. In this thesis, it is proven that phase-matching of the mSHG and surface electromagnetic waves can lead to the enhancement of both the SH yield and the nonlinear magneto-optical signal. These results are important for controlling of the nonlinear magneto-optical response and could impact the development of magnetic storage devices, label-free biosensors and nonlinear magneto-optical switches.

The coupling of the collective oscillation of electrons at the metallic surface and electromagnetic wave results in the SPPs, in which the electromagnetic field is highly concentrated within a sub-wavelength volume near the surface. Employing Kretschmann configuration, SPPs can be excited in hybrid metal-ferromagnet multilayers. Here, two sets of distinct structures have been inspected: Au/Co bilayers and Au/Co/Ag trilayers. In both types of structures, it has been proven that the strong plasmonic field enhancement at the fundamental frequency is the main reason for the characteristic peak in the angular dependence of the SH output. In contrast, the large-angle SH dip originates from the interference of the non-resonant SH field and the radiative SPP at the doubled SH frequency. Comparison of the experimental data with the phenomenological model reveals the fingerprints of linear SPP and second-harmonic SPP in the magnetic SH contrast, where the Lorentzian phase-matching function represents the basic result in nonlinear magneto-plasmonics. Thus, the angular dependence of the far-field mSHG response can be utilized as a measure of the excitation efficiency of SPPs. Also, it has been shown that upon the excitation of the nonlinear SPP, the mSHG signal can be enhanced up to 60%.

Nonlinear magneto-photonics on periodic structures has been performed in a different regime where grating effects dominate over the plasmonic ones. Periodic arrays of nickel nanodimers on a silicon substrate were fabricated by electron lithography in such a way that their low surface filling factor ruled out the SPP excitation. In this case, surface electromagnetic waves can be generated under conditions of Wood's anomaly, when the diffraction order emerging at the surface depletes the energy of other diffraction orders. The observation of Wood's anomaly depends on the ratio of the fundamental optical wavelength λ to the grating period $\Lambda > \lambda/2$. In the case of nonlinear-optical excitation, multiple harmonics become involved making the phenomenon of such mixed Wood's anomaly very complicated. However, in the case of

SH generation and the grating period falling within the range of $\lambda/4 < \Lambda < \lambda/2$, the excitation of the nonlinear Wood's anomaly is allowed exclusively at the SH wavelength while the linear one is prohibited. From the comparison of the angular dependencies of the linear reflectivity and the mSHG response, the redistribution of energy between different diffractions orders in the nonlinear regime is about one order of magnitude higher than that in the linear regime. Furthermore, the angular spectrum of the SH magnetic contrast clearly shows the fingerprints of the nonlinear diffraction anomaly.

List of Figures

2.1 Comparison of the dielectric function of silver estimated by Drude model and measured experimentally 11
2.2 Three configurations of magneto-optical Kerr effects 13
2.3 Comparison of harmonic and anharmonic potential 14
2.4 Illustration for the anharmonic oscillation of a free electron 18
2.5 Phasor diagram of the non-magnetic and magnetic SH fields 20
2.6 Boundary conditions for p-polarized light at the interface between metal and dielectric 21
2.7 Real and imaginary parts of dielectric functions of silver, gold and cobalt 22
2.8 Vector field of SPP localized at gold/air interface at wavelength 1560 nm 23
2.9 Dispersion relations of SPP at silver/air interface 24
2.10 Different geometries where SPP is excited by prism coupling 26
2.11 Excitation of SPP by a diffraction grating. 27
2.12 Comparison between the angular dependence of linear reflectivity measured experimentally and simulated using MTM 28
2.13 Propagation length and skin depth of the SPP field excited at metal/air surface in different structures 29

3.1 Kretschmann configuration applied for the metal/ferromagnet bilayers and trilayers 32
3.2 Scheme of a linear magneto-plasmonic setup employing Kretschmann configuration 34
3.3 Top-view of a SH nonlinear magneto-plasmonic setup based on Kretschmann geometry. 35
3.4 Dependence of magnetic field strength on distance from the pole of a Neodymium permanent magnet 35
3.5 Fluence dependence of the signal detected by the PMT 36
3.6 An example of the counting scheme 37
3.7 Angular dependence of linear transversal MOKE measured on the bilayers at the wavelength 633 nm 39
3.8 Angular dependences of the linear reflectivity, SH intensity and magnetic contrast for the bilayer (20 nm)Au/ (30 nm)Co 40
3.9 Angular dependences of the linear reflectivity, SH intensity and magnetic contrast for the set of trilayers 41

3.10 Illustration of nonlinear excitation of SPP by SHG in bilayer (20 nm)Au/ (30 nm)Co employing Kretschmann configuration 42
3.11 The phasor diagram of non-magnetic and magnetic SHG fields in a hybrid structure 46
3.12 Angular dependence of electric field $|E|$ components at different interfaces of the trilayer 49
3.13 Illustration for the electric field components in reflection. 50
3.14 Forward approach: comparison between experimental and simulated SH intensity and magnetic contrast 51
3.15 Reverse approach: fit the newly-defined magnetic contrast ϕ to estimate the Lorentzian function 52
3.16 Dispersion of the Lorentzian function 54
3.17 Angular dependence of the conventional magnetic contrast ρ at different wavelengths 55
3.18 Angular dependence for the bilayer (20 nm)Au/ (30 nm)Co excited at the fundamental wavelength 1560 nm 56
3.19 Angular dependence of the SH intensity and magnetic contrasts of trilayer (5 nm)Au/(10 nm)Co/(25 nm)Ag excited at the fundamental wavelength 1200 nm. 58
3.20 The nonlinear Lorentzian function and SH fields for trilayers with different Ag thicknesses. 59
3.21 Illustration of a charge at the boundary between two conducting media Co and Au 60
3.22 The trajectory of electrons in the Au and in the Co bulk 61

4.1 Illustrations of linear and nonlinear diffraction orders in reflection on a grating 64
4.2 Schematic for the co-excitation of linear and nonlinear Wood's anomalies, and the structure of periodic arrays of nickel dimers 66
4.3 The top-view of the experimental setup for nonlinear Wood's anomaly in the periodic structures. 67
4.4 Angular dependence of the linear reflectivity, the SH intensity and magnetic contrast in the dimer arrays at the fundamental wavelength 820 nm 68
4.5 Normalized linear reflectivity and SH intensity for the dimer arrays at different wavelengths 70
4.6 Dispersion of the Wood's anomalies excited in the two-dimensional nanoarrays 73
4.7 False-color images of the SH magnetic contrast at different grating constants 74

5.1 Angular dependence of the mSHG intensity and the SH magnetic contrast in the bilayer and the trilayer at different pump powers 78
5.2 Angular scan of the linear reflectivity for the bilayer and the trilayer at different pump powers 80
5.3 A simplified schema for the setup of the magneto-plasmonic auto-correlation 81

5.4 Non-resonant and resonant SH pulses in the Kretschmann configuration 82
5.5 Time-integrated measurements of linear reflectivity, the mSHG outputs and the SH magnetic contrast for the trilayer (5 nm)Au/ (10 nm)Co/ (15 nm)Ag 85
5.6 Intensity auto-correlation in the layer (5 nm)Au/ (10 nm)Co/ (15 nm)Ag employing the Kretschmann configuration 86
5.7 Time-resolved second-harmonic magnetic contrast ρ of the trilayer (5 nm)Au/ (10 nm)Co/ (15 nm)Ag. 87
5.8 The mSHG cross-correlation on the Kretschmann configuration. 88
5.9 A simplified scheme for the cross-correlation of mSHG on the Kretschmann geometry. 89
5.10 Spectrally-resolved linear cross-correlation of a reference wave with the mSHG signal at different fixed time delays 90

A.1 Spectra of the fundamental and reference (local oscillator) radiations for the cross-correlation experiment in Konstanz. 98

B.1 Power dependence of the TH output in the trilayer 102
B.2 Angular dependence of the TH intensity in the trilayer (5 nm) Au/(10 nm) Co/(15 nm) Ag 102

List of Tables

2.1 Interband transition threshold and plasmon energy of common plasmonic metals 9
2.2 Dielectric tensors, reflectivity matrix and reflected signal for three different MOKE configurations 13

3.1 Set of samples used in this work 33
3.2 The non-zero second-order nonlinear susceptibility components for p-polarized fundamental radiation. 43
3.3 The roles of different SH susceptibilities in the multilayer structure of Au/Co/Ag/glass. 50
3.4 Parameters used for the simulation of mSHG in bilayer Au/Co 55
3.5 Dominant SH field components assumed for the mSHG in trilayer Au/ Co/ Ag 57

A.1 Estimation of relative thicknesses between different layers in the hybrid structure employing the SPP 97
A.2 Techinical specification of Toptica fiber laser for nonlinear magneto-plasmonic setup 98
A.3 Technical specifications of the photon counting regime 98

Contents

Abstract **I**

List of Figures **V**

List of Tables **IX**

Contents **XI**

1 Introduction and Motivation **1**

2 Light matter interaction **5**
2.1 Light propagation in matters 5
2.2 Linear magneto-optical responses 8
2.2.1 Drude model and optical properties of metals 9
2.2.2 Linear magneto-optical effects 11
2.2.3 Magneto-optical Kerr effect (MOKE) 12
2.3 Nonlinear magneto-optical responses 14
2.3.1 Model of anharmonic oscillation and SHG 14
2.3.2 Magnetization-induced Second Harmonic Generation 19
2.4 Surface plasmons 20
2.4.1 Propagating surface plasmon polaritons 20
2.4.2 Excitation of SPP 24
2.4.3 Simulation of SPPs in multilayer structures 27
2.4.4 Magneto-plasmonics 30

3 Nonlinear magneto-plasmonics on Kretschmann configuration **31**
3.1 Measurements of Kretschmann magneto-plasmonics 31
3.1.1 Samples 31
3.1.2 Setup 33
3.1.3 Light source 37
3.2 Results 38
3.2.1 Bilayer structure of Au/Co 38
3.2.2 Trilayer structure of Au/Co/Ag 40
3.3 Theoretical description 42
3.3.1 Radiative nonlinear surface plasmon polaritons 43
3.3.2 Calculate SHG magnetic contrast (abcd-model) 45

3.4 Simulation methods . . . 47
3.4.1 Forward approach . . . 48
3.4.2 Reverse approach . . . 50
3.4.3 Conclusion about two simulation approaches . . . 53
3.5 Dispersion of Lorentzian function . . . 53
3.6 Discussion . . . 54
3.6.1 Bilayer structures . . . 54
3.6.2 Trilayer structures . . . 57
3.6.3 SHG due to instantaneous change of damping constant . . . 59
3.7 Conclusion . . . 60

4 Nonlinear magneto-optics in diffraction anomalies 63
4.1 Nonlinear Wood's anomaly . . . 63
4.1.1 Diffraction on grating . . . 63
4.1.2 Wood's anomaly . . . 65
4.2 Experimental methods . . . 65
4.3 Results and discussions . . . 68
4.3.1 Nonlinear Wood's anomaly and MOKE in nanodimers . . . 68
4.3.2 Spectral analysis . . . 69
4.3.3 Specifying the order of Wood's anomaly . . . 71
4.3.4 Impact of Wood's anomaly on nonlinear MOKE . . . 72
4.4 Conclusion . . . 74

5 Femtosecond time-resolved nonlinear magneto-plasmonic cross-correlation measurements 77
5.1 Fluence dependence of the mSHG . . . 77
5.2 Magneto-plasmonic auto-correlation . . . 80
5.2.1 Magneto-plasmonics auto-correlation setup . . . 81
5.2.2 Results and discussion . . . 85
5.3 Magneto-plasmonic cross-correlation . . . 88
5.3.1 Magneto-plasmonic cross-correlation setup . . . 88
5.3.2 Results and discussion . . . 89
5.4 Conclusion . . . 90

6 Summary and conclusion 93

Appendix A Technical specifications 97
A.1 Verify film thickness using ATIR . . . 97
A.2 Technical specifications . . . 97

Appendix B Third-harmonic generation in metallic thin film 99
B.1 Estimation of Third-harmonic generation (THG) in Au film . . . 99
B.2 Third-harmonic magneto-plasmonics . . . 102

Abbreviations 104

List of publications **105**

Bibliography **107**

Chapter 1

Introduction and Motivation

Observed for the first time by Wood[1] in 1902, electromagnetic surface waves propagating on metallic surface, specifically surface plasmon polaritons and Wood's anomalies, have been employed in a lot of research topics and applications. They are one of the main subjects in the field of nano-photonics, where the excitation of these electromagnetic surface waves on metallic nanostructure enhances significantly the optical properties, such as magneto-optics, nonlinear optics, extraordinary transmission, etc.

Surface plasmons (SPs) refer to the oscillations of free electrons at metallic surfaces. The coupling of an electric field at optical frequencies with the SPs, known as surface plasmon polaritons (SPP), results in a strong electric field localization in the vicinity of the metallic surface. SPPs enhance a multitude of optical phenomena in metallic nanostructures [2], including magneto-optical effects [3], second-harmonic generation (SHG) [4, 5] and the combination of these two effects, i.e. the magnetization-induced SHG (mSHG) [6, 7].

Magneto-plasmonics[3] is an emerging concept which attempts to improve the magneto-optical properties employing SPs and, conversely, to control the SPs using an external magnetic field. It can be applied to design and improve the performance of all-optical magnetic data storage, optical switches, label-free sensors [2]. Magneto-plasmonics structures must couple magnetic properties and SP possible excitation. Owing to the low optical absorption in the visible spectral range, noble metals (gold, silver, copper) have been used as efficient media for the excitation of SPs. However, these metals are non-magnetic and exhibit measurable magneto-optical properties only under strong external magnetic fields [8–10]. In contrast, ferromagnetic transition metals (iron, cobalt, nickel) show sizable magneto-optical effects, but have high optical losses. One solution is to combine ferromagnetic and noble metals in a single hybrid metal/ferromagnet structure. For example, a thin ferromagnetic film sandwiched between two noble metals has demonstrated a strong enhancement of both linear [3, 11–14] and nonlinear [6, 7, 15] magneto-optical effects induced by the propagating surface plasmon polaritons (SPP) in Kretschmann configuration. Apart from continuous thin films, far-field radiation can be coupled to the SPPs in nanostructured metallic media, forming a class of magneto-plasmonic crystals. For example, a gold grating on top of magnetic dielectric [16–18] enables the phase-matched SPP excitation by taking advantages of the periodic corrugations. Another interesting approach

makes use of extraordinary optical transmission in subwavelength hole arrays [19–23] featuring SPP excitation at the surface of a magnetic film [24, 25]. Further, perforated transition metal layers have shown enhanced magneto-optical effects [26–28] and SPP-induced phase shifts between the magnetic and the nonmagnetic second harmonic (SH) fields [29]. Besides, metal/ferromagnet heterostructures have been exploited extensively in the of ultrafast acoustics [30], exchanged-coupled magnonics [31], spintronics [32, 33] and terahertz emission [34, 35]. Thus, we can envision the consolidation of plasmonics with the ultrafast effects [7] in a single metallic device.

The mSHG refers to the SH signals that are sensitive to the magnetization. They are generated from the magnetization-odd second-order nonlinear susceptibility, which is high in ferromagnetic metals. In most metals, the mSHG in magnetic multilayer structures occurs exclusively at surfaces and interfaces [36–39], where the spatial inversion symmetry is broken [40–42]. The measurement of mSHG has been applied to study magnetic phenomena in hybrid thin films, such as magnetization dynamics [43] and spin-dependent effects [33].

The combination of the advantages of SPP and mSHG gives rise to the nonlinear magneto-plasmonics, a sensitive technique to inspect the magnetic interfaces. The excitation of SPP on hybrid thin films of noble-metal (NM)/ ferromagnet (FM) has usually been performed using conventional Kretschmann configuration due to the setup simplicity. Inherited from the researches in linear regime [3], the trilayer of NM/FM/NM has usually been employed for the nonlinear magneto-plasmonics [6, 15]. In fact, the plasmonic enhancement of the mSHG has been observed in a mono-layer of iron [44], where the coupling to SPP is not supposed to be efficient. To fill in the gap, it is necessary to investigate the bilayer NM/FM as well, even though it has been disregarded in the field of linear magneto-plasmonics [3]. In this work, both the bilayer NM/FM and the trilayer NM/FM/NM will be inspected, in order to explain the interplay between plasmonics and magneto-optics in the nonlinear regime. The experiments will be interpreted within the framework of simplified theoretical models.

Merging functionalities of plasmonic materials [19] with the optical properties of diffraction gratings and periodic structures with a sub-wavelength periodicity, i.e. optical meta-surfaces [45–50], is also an attractive approach. These systems are often discussed in the context of plasmonics [21–23] and magneto-plasmonics [16–18, 24, 25, 51], if one of the ingredients displays magneto-optical properties.

In plasmonics, spectrally narrow resonances, commonly referred to as surface lattice resonances (SLRs) [46, 47, 52, 53], arise from an unusual interplay between the localized surface plasmon resonance (LSPR) and the emerging diffraction orders under the condition of Wood's anomaly. The latter describes redistribution of the light energy between different diffracted beams upon opening of a new diffraction order propagating along the grating surface [1].

In magneto-plasmonics, the excitation of Wood's anomalies in two-dimensional arrays of ferromagnetic nanodisks resulted in the enhancement of the magneto-optical effects [53, 54]. While one can expect a weak LSPR field from a single optically-lossy nanodisk [55], bringing two disks closer (thus forming a dimer) boosts the nanoantenna

effect in the air gap. The MOKE signals show a clear dependence on the dimer size, that is, distance between the pair of the nickel disks, enabling a ruler at the nanoscale [56]. In these structures, plasmonic effects have been enabled either by a high relative content of the metal resulting in the excitation of propagating surface plasmon-polaritons (even despite high optical losses in ferromagnetic transition metals), or LSPRs in the nanosized metallic objects.

A conventional diffraction grating requires the grating period Λ to be larger than a half of the optical free space wavelength λ ($\Lambda > \lambda/2$) to ensure the presence of at least one diffraction order. In contrast, optical meta-surfaces are usually characterized by a much smaller periodicity $\Lambda \ll \lambda$ [50, 57, 58]. Overcoming this frontier, an intriguing crossover regime can be explored within the realms of nonlinear optics, where the wavelength λ of the fundamental radiation is converted to λ/n by means of a nonlinear-optical process of the order $n > 1$. In this case, the same periodic structure can serve as a meta-surface for the fundamental light at λ, and as a regular grating for the outgoing radiation with the wavelength λ/n. Although the condition for this transition regime $\lambda \gg \Lambda > \lambda/2n$ is relatively easy to fulfill in the visible and near-infrared optical range, the nonlinear-optical properties of such hybrid gratings remain up to date unexplored.

Despite the large amount of research on magneto-photonic crystals in general, the studies of nonlinear magnetization-induced Wood's anomalies are very scarce. In particular, the role and the impact of the Wood's anomalies in ferromagnetic arrays on the SH generation remains widely unexplored. To fill this gap, this work studies the Wood's anomaly, i.e. the intrinsic property of an optical grating, in the aforementioned nonlinear transition regime. The angle-dependent SH spectroscopy is performed with tunable femtosecond laser source on a rectangular array of nickel dimers featuring a nanoscale gap, similar to that studied in Ref. [46]. Taking advantage of the unequal periodicity of the array in two orthogonal in-plane directions, one can identify the frontiers of the novel crossover regime for nonlinear Wood's anomaly, i.e. when the structure exhibits grating properties exclusively at the SH wavelength $\lambda/2$ but not at the fundamental wavelength λ. Our experiments represent the first step towards the application of nonlinear optics for understanding the transition between optical diffraction gratings and meta-surfaces, extending the concept of Wood's anomaly [59, 60] to the nonlinear regime.

This thesis consists of six chapters. **Chapter 2** introduces the theoretical basis for the following chapters. I try to derive the optical phenomena by classical model without quantum optics. The linear optical response of metals, including the magneto-optical Kerr effect, will be derived using Drude model. Then the second-harmonic generation (SHG) will be described by the model of an anharmonic oscillator. The magnetization-induced SHG will be as well discussed in the section of nonlinear optical response. A part is also devoted to the SPP, a solution of the Maxwell's equations, and the methods to excite it. The formulation of the magneto-plasmonics in the linear regime is introduced.

Chapter 3 discusses the nonlinear magneto-plasmonics employing the Kretschmann geometry. The samples, measurements method and preliminary results will be pre-

sented in details. Two sets of samples are examined: the trilayer Au/Co/Ag and the bilayer Au/Co. A simplified theoretical model is then developed, based on which the mSHG and the SH magnetic contrast in the trilayer and the bilayer can be simulated in high agreement with the experimental data. The features in the angular dependence of mSHG and the SH magnetic contrast can be explained by the coupling of the fields to SPP.

Chapter 4 explores the nonlinear Wood's anomaly on two-dimensional arrays of nickel nanodimers. The surface waves in this case is no longer SPP, but the excitation method is similar to that using periodic grating. The chapter will revise the definition of Wood's anomaly, a less common term compared to SPP, in the linear and the nonlinear regime. It will be shown that the excitation of the linear and nonlinear Wood's anomalies at different transversal and longitudinal periodicities of the rectangular arrays, which are $\lambda/4 < \Lambda_T < \lambda/2$ and $\Lambda_L > \lambda/2$ respectively, demonstrates experimentally the transition regime speculated for the nonlinear diffraction. The effects of the nonlinear Wood's anomaly on the mSHG and the magnetic contrast will be discussed in details. The possibility to couple the Wood's anomaly with the LSPR within the nanodimer gap to form the hybrid SLR will also be considered.

Chapter 5 includes miscellaneous experiments related to the nonlinear magnetoplasmonics in Kretschmann multilayers. Three main parts in this chapter are (i) the demagnetization of the SH magnetic contrast at high power, (ii) the influence of SPPs on the magnetically-controlled auto-correlations and (iii) the spectrally-resolved cross-correlation of the mSHG induced by SPPs. The thesis is concluded in **Chapter 6** with a brief summary of the work and an overlook.

Chapter 2

Light matter interaction

Light has wave-particle dualitiy. But usually the wave properties of light is sufficient to describe the light-matter interaction. In this chapter, the linear optical responses of materials, the optical-nonlinear generation and the surface plasmons will be derived from the classical descriptions of the electromagnetic waves.

2.1 Light propagation in matters

Interaction of electromagnetic waves and matter are described by four Maxwell's equations in S.I. units [61, 62]

$$\begin{aligned} \nabla \times \boldsymbol{E}(\boldsymbol{r},t) &= -\frac{\partial \boldsymbol{B}(\boldsymbol{r},t)}{\partial t} \\ \nabla \times \boldsymbol{H}(\boldsymbol{r},t) &= \frac{\partial \boldsymbol{D}(\boldsymbol{r},t)}{\partial t} + \boldsymbol{j}(\boldsymbol{r},t) \\ \nabla \cdot \boldsymbol{D}(\boldsymbol{r},t) &= \rho(\boldsymbol{r},t) \\ \nabla \cdot \boldsymbol{B}(\boldsymbol{r},t) &= 0 \end{aligned} \tag{2.1}$$

where $\boldsymbol{E}$ is the electric field, $\boldsymbol{H}$ is the magnetic field, $\boldsymbol{D}$ is the electric displacement, $\boldsymbol{B}$ is the magnetic induction, ρ is the charge density and $\boldsymbol{j}$ is the current density. The bold letters show vector quantities, which depend on position and time, such as $\boldsymbol{E}(\boldsymbol{r},t)$. The conservation of charge requires that $\nabla \cdot \boldsymbol{j} = -\dfrac{\partial \rho}{\partial t}$.

For a monochromatic field, the time-dependent electric field can be presented as

$$\boldsymbol{E}(\boldsymbol{r},t) = \Re\big\{\boldsymbol{E}(\boldsymbol{r})e^{-i\omega t}\big\} = \frac{1}{2}\big[\boldsymbol{E}(\boldsymbol{r})e^{-i\omega t} + \boldsymbol{E}^{*}(\boldsymbol{r})e^{i\omega t}\big] \tag{2.2}$$

where $\boldsymbol{E}(\boldsymbol{r})$ is the complex spatial component of a harmonic electric field oscillating in time at a fixed frequency ω. For plane waves, we have $\boldsymbol{E}(\boldsymbol{r}) = \boldsymbol{E}_0 e^{\pm i\boldsymbol{k}\cdot\boldsymbol{r}}$, where $\boldsymbol{k}$ is the wavevector with $|\boldsymbol{k}| = \omega/c\sqrt{\mu\varepsilon}$. As a homogeneous solution of the Maxwell's equations when $\rho = 0$ and $\nabla \cdot \boldsymbol{D}(\boldsymbol{r},t) = 0$, plane waves also require that $\boldsymbol{k} \cdot \boldsymbol{E}_0 = 0$ and $\boldsymbol{H}_0 = \frac{1}{\omega\mu_0}(\boldsymbol{k} \times \boldsymbol{E}_0)$.

In general, the spectrum of a time-dependent field $\boldsymbol{E}(\boldsymbol{r},t)$ is defined by the Fourier transform

$$\hat{\boldsymbol{E}}(\boldsymbol{r},\omega)=\frac{1}{\sqrt{2\pi}}\int_{-\infty}^{+\infty}\boldsymbol{E}(\boldsymbol{r},t)e^{-i\omega t}dt \tag{2.3}$$

and the inverse Fourier transform gives time-dependent field from its spectrum

$$\boldsymbol{E}(\boldsymbol{r},t)=\frac{1}{\sqrt{2\pi}}\int_{-\infty}^{+\infty}\hat{\boldsymbol{E}}(\boldsymbol{r},\omega)e^{i\omega t}d\omega \tag{2.4}$$

Applying the Fourier transform[1], Maxwell's equations in Eq. 2.1 can be written in the frequency domain

$$\begin{aligned}\nabla\times\hat{\boldsymbol{E}}(\boldsymbol{r},\omega)&=i\omega\hat{\boldsymbol{B}}(\boldsymbol{r},\omega)\\ \nabla\times\hat{\boldsymbol{H}}(\boldsymbol{r},\omega)&=-i\omega\hat{\boldsymbol{D}}(\boldsymbol{r},\omega)+\hat{\boldsymbol{j}}(\boldsymbol{r},\omega)\\ \nabla\cdot\hat{\boldsymbol{D}}(\boldsymbol{r},\omega)&=\hat{\rho}(\boldsymbol{r},\omega)\\ \nabla\cdot\hat{\boldsymbol{B}}(\boldsymbol{r},\omega)&=0\end{aligned} \tag{2.5}$$

Consider a structure consisting of two media, indicated by the indices p and q, where the material properties in each medium is independent on position $\boldsymbol{r}$. The subdomains p and q are homogeneous, but the whole structure, including the boundary pq between the two media, is inhomogeneous. In this case, instead of solving the wave equations for an inhomogeneous medium, it is more convenient to find the solutions in each subdomain separately, then combine them by boundary conditions. Using separation of variables, the Helmholtz equations below can be derived from Maxwell's equations[2] and represent for the wave equations in medium p.

$$\begin{aligned}\left(\nabla^2+k_p^2\right)\boldsymbol{E}_p&=-i\omega\mu_0\mu_p\boldsymbol{j}_p+\frac{\nabla\rho_p}{\epsilon_0\epsilon_p}\\ \left(\nabla^2+k_p^2\right)\boldsymbol{H}_p&=\nabla\times\boldsymbol{j}_p\end{aligned} \tag{2.6}$$

where the wavenumber $k_p=|\boldsymbol{k}_p|=\frac{\omega}{c}\sqrt{\mu_p\epsilon_p}$. The Helmholtz equations become homogeneous when ρ_p and $\boldsymbol{j}_p=0$.

To guarantee the continuity of the electromagnetic field across the boundary pq, it is necessary to take integral forms of Maxwell's equations[3], which leads to the following conditions at the interface [62]

$$\begin{aligned}\boldsymbol{n}\times(\boldsymbol{E}_p-\boldsymbol{E}_q)&=0\\ \boldsymbol{n}\times(\boldsymbol{H}_p-\boldsymbol{H}_q)&=K\\ \boldsymbol{n}\cdot(\boldsymbol{D}_p-\boldsymbol{D}_q)&=\sigma\\ \boldsymbol{n}\cdot(\boldsymbol{B}_p-\boldsymbol{B}_q)&=0\end{aligned} \tag{2.7}$$

[1] One can replace the time derivative and integral by a factor: $\frac{\partial}{\partial t}\xrightarrow{F.T}i\omega$ and $\int dt\xrightarrow{F.T}\frac{1}{i\omega}$

[2] with the identity $\nabla\times\nabla\times=-\nabla^2+\nabla\nabla\cdot$

[3] It means to take surface integral for $\boldsymbol{E}(\boldsymbol{r},t)$, $\boldsymbol{H}(\boldsymbol{r},t)$, and volume integral $\boldsymbol{D}(\boldsymbol{r},t)$, $\boldsymbol{B}(\boldsymbol{r},t)$ across the boundary pq.

where $\boldsymbol{n}$ is the normal vector at the interface, K is the surface current density, and σ is the conductivity of the medium. Fresnel reflection and transmission coefficients [61] are the results of the boundary conditions applied for plane wave incident on a planar interface. The boundary condition is essential for the description of surface plasmon field in section 2.4.

In the macroscopic regime, the response of the material to an electromagnetic field is included in the polarization $\boldsymbol{P}$ and magnetization $\boldsymbol{M}$, which are the volume density of electric and magnetic dipole moments, respectively.

$$\begin{aligned} \boldsymbol{D}(\boldsymbol{r},t) &= \varepsilon_0 \boldsymbol{E}(\boldsymbol{r},t) + \boldsymbol{P}(\boldsymbol{r},t) \\ \boldsymbol{H}(\boldsymbol{r},t) &= \frac{1}{\mu_0}\boldsymbol{B}(\boldsymbol{r},t) - \boldsymbol{M}(\boldsymbol{r},t) \end{aligned} \tag{2.8}$$

where $\varepsilon_0 = 8.854\times10^{-12}$ F/m is the permittivity of free space, and $\mu_0 = 4\pi\times10^{-7}$ H/m is the vacuum permeability. These two constants are related by $\varepsilon_0\mu_0 = 1/c^2$, where $c = 2.998 \times 10^8$ m/s is the speed of light. In a conducting medium, the conduction current density depends on the electric field with $\boldsymbol{j} = \sigma\boldsymbol{E}$, where σ is the conductivity.

Inserting Eq. 2.8 into Eq. 2.1 gives the wave equations in a medium

$$\begin{aligned} \nabla\times\nabla\times\boldsymbol{E} + \frac{1}{c^2}\frac{\partial^2\boldsymbol{E}}{\partial t^2} &= -\mu_0\frac{\partial}{\partial t}\Big(\boldsymbol{j} + \frac{\partial\boldsymbol{P}}{\partial t} + \nabla\times\boldsymbol{M}\Big) \\ \nabla\times\nabla\times\boldsymbol{H} + \frac{1}{c^2}\frac{\partial^2\boldsymbol{H}}{\partial t^2} &= \nabla\times\boldsymbol{j} + \nabla\times\frac{\partial\boldsymbol{P}}{\partial t} + \mu_0\frac{\partial\boldsymbol{M}}{\partial t} \end{aligned} \tag{2.9}$$

Here $\boldsymbol{E}(\boldsymbol{r},t)$ is denoted as $\boldsymbol{E}$ for simplicity. This set of equations describes the propagation of an electromagnetic wave in a medium having polarization $\boldsymbol{P}$ and magnetization $\boldsymbol{M}$. Similar to Eq. 2.6, these wave equations become homogeneous in the case of no free charge ($\rho = 0$) and non-conducting ($\boldsymbol{j} = 0$) medium.

In general, $\boldsymbol{P}$ can be expressed as a power series of the electric field $\boldsymbol{E}$ as following [40]

$$\begin{aligned} \boldsymbol{P} &= \epsilon_0\Big[\chi^{(1)}\boldsymbol{E} + \chi^{(2)}\boldsymbol{E}^2 + \chi^{(3)}\boldsymbol{E}^3 + \dots\Big] \\ &= P^{(1)} + P^{(2)} + P^{(3)} + \dots \end{aligned} \tag{2.10}$$

where $\chi^{(1)}$ is the linear(first-order) susceptibility. In the linear optics, the expansion stops at the first-order polarization $P^{(1)}$, which is proportional to the incident electric field $\boldsymbol{E}$. In that case, the electric displacement given in Eq. 2.8 is written as

$$\begin{aligned} \boldsymbol{D} &= \varepsilon_0\boldsymbol{E} + \boldsymbol{P} \\ &= \epsilon_0\big[1 + \chi^{(1)}\big]\boldsymbol{E} = \epsilon_0\epsilon\boldsymbol{E} \end{aligned} \tag{2.11}$$

where the dielectric function is denoted as $\epsilon = 1 + \chi^{(1)}$. When the electric field is written in the vector form $\boldsymbol{E} = \big(E_x, E_y, E_z\big)$, the dielectric function and the linear susceptibility expand into 3-by-3 tensors. Eq. 2.11 can thus be written in the matrix form

$$\begin{bmatrix} D_x \\ D_y \\ D_z \end{bmatrix} = \epsilon_0 \begin{bmatrix} \epsilon_{xx} & \epsilon_{xy} & \epsilon_{xz} \\ \epsilon_{yx} & \epsilon_{yy} & \epsilon_{yz} \\ \epsilon_{zx} & \epsilon_{zy} & \epsilon_{zz} \end{bmatrix} \begin{bmatrix} E_x \\ E_y \\ E_z \end{bmatrix} \tag{2.12}$$

In isotropic homogeneous non-magnetic media, the off-diagonal elements of the ϵ tensor vanish, and the diagonal components are equal $\epsilon_{xx} = \epsilon_{yy} = \epsilon_{zz} = \epsilon$, making the dielectric function ϵ a constant. The off-diagonal components become non-zero in magnetic media, which will be discussed in later section.

Note that the relation between the complex dielectric function $\epsilon = \epsilon' + i\epsilon''$ and the optical refractive index $n = n' + in''$ of the medium is as following

$$\begin{aligned} \epsilon &= n^2 = (n' + in'')^2 \\ \epsilon' &= n'^2 - n''^2 \\ \epsilon'' &= 2n'n'' \end{aligned} \tag{2.13}$$

Back to Eq. 2.10, in nonlinear optics, the power series of $\boldsymbol{P}$ can be extended to the second-order nonlinear polarization $P^{(2)} = \epsilon_0\chi^{(2)}\boldsymbol{E}^2$, the third-order nonlinear polarization $P^{(3)} = \epsilon_0\chi^{(3)}\boldsymbol{E}^3$ and so on. $\chi^{(2)}$ and $\chi^{(3)}$ are called the second-order and third-order nonlinear susceptibility, respectively. It is expected for condensed matter that the linear susceptibility $\chi^{(1)}$ is of the order of unity, $\chi^{(2)} \propto \chi^{(1)/E_{at}}$ and $\chi^{(3)} \propto \chi^{(1)/E_{at}^2}$ [40], where E_{at} is the atomic electric field strength[4]. As the power of the electric field increases, the rank of the susceptibility tensor rises accordingly. For example, $\chi^{(1)}$ is a second-rank tensor with $3^2 = 9$ components, $\chi^{(2)}$ is a third-rank tensor with $3^3 = 27$ components. However, in later section, it will be shown that the symmetry can reduce significantly the number of tensor components.

2.2 Linear magneto-optical responses

As mentioned in the previous section, the dielectric function and susceptibility represent for the optical responses of materials. Several models have been developed to characterize these properties, such as the classical Lorentz [63, 64] and Drude [65, 66] models. The difference between these two models is that Lorentz model concerns the interaction of bound electrons or lattice with the electromagnetic field, while Drude model considers only the unbound electrons. Drude model is used to describe the interaction of light and metals or plasma, where free electrons dictate the optical properties. Based on this model, the dielectric function ϵ can be derived from the equation of motion of a free electron driven by an external electromagnetic field. Following this strategy, the magneto-optical properties of ferromagnetic metals, the nonlinear generations at metallic interfaces and the plasmonic properties of noble metals can also be explained, as discussed in the following sections. Drude model can accurately predict the optical properties of metals in the infrared/terahertz spectral range, where there is only intraband transition between states within the sp-band and the electrons are unlocalized. In the visible regime, one has to take into account the interband transitions, where the incident photon has enough energy to excite an electron from occupied states in d-band to unoccupied states in sp-band, which is higher than Fermi level. For example, the interband transition threshold[5] of gold occurs at around 2.4 eV [5, 67]

[4] $E_{at} = \frac{q}{4\pi\epsilon_0 a_0^2} = 5.14 \times 10^11$ V/m, where a_0 is the Bohr radius of the hydrogen atom.

[5] Transition threshold is the lowest energy between an occupied state in a lower band and an unoccupied state in an upper conduction band.

(or 516 nm, which is the reason for its color in bulk state). In our research, both the fundamental excitation (0.8 eV) and second harmonic generation (1.6 eV) are far below interband transition threshold of noble metals (see Table. 2.1). Drude model, concerning only the low-frequency intraband transition, is thus applicable.

Metal	$\boldsymbol{E_{inter}}$ (eV)	$\boldsymbol{\lambda_{inter}}$ (nm)	$\boldsymbol{\hbar\omega_p}$ (eV)
Gold	2.4	516	8.55-8.99
Silver	4.0	310	8.9-9.0
Copper	2.17	571	7.4-7.9
Aluminium	1.55	800	14.7

Table 2.1 – The second and third columns are the interband transition thresholds of plasmonic metals in term of photon energy E_{inter} (eV) and wavelength λ_{inter} (nm) [5, 67–71]. The fourth column shows plasmon energy $\hbar\omega_p$ (eV) of these metals [72–76].

2.2.1 Drude model and optical properties of metals

Imagine that free electron gas is driven by an external electric field $\boldsymbol{E}$ and shifts to one side of the material. This causes a difference in electron density and thus an induced electric field to pull the electron sea back to equilibrium. This is a harmonic oscillation which can be described by solving the equation of motion of an unbound electron in a time-dependent electric field.

$$m\frac{\partial^2 \boldsymbol{r}}{\partial t^2} + \gamma m\frac{\partial \boldsymbol{r}}{\partial t} = -q\boldsymbol{E}(t) \tag{2.14}$$

where m is the effective mass of electron, $\boldsymbol{r}$ is the electron trajectory, q is the elementary charge, γ is the damping constant and $\boldsymbol{E}(t)$ is the external electric field[6]. Here the magnetic component of the incident electromagnetic field is disregarded, since its effect is negligible compared to the electric component.

Driven by the electric field, the free electron travels at Fermi velocity v_F until it collides with a phonon or another electron [77–80]. The time between two collisions is called scattering time or relaxation time $\tau_{sc} = l/v_F$, where l is the mean free path of electron. τ_{sc} contributes to Eq. 2.14 through the damping constant $\gamma = 1/\tau_{sc}$. For plasma, electrons travel without collision, thus there is no scattering $\gamma = 0$. For noble metals, such as gold, silver and copper, the electron mean free path at room temperature is very long, ≈40-50 nm[81]. The motion of electron is π out-of-phase to the driving electric field $\boldsymbol{E}(t)$.

The oscillation of an electron gives an electric dipole moment $\boldsymbol{\mu}(t) = -q\boldsymbol{r}(t)$. In macroscopic regime, polarization corresponds to the volume density of dipole moments

$$\boldsymbol{P}(t) = N\boldsymbol{\mu}(t) = -Nq\boldsymbol{r}(t) \tag{2.15}$$

[6]This is the difference between the Lorentz and Drude models. In Lorentz model, there is a restoring force from positively charged lattice site $F_{restoring} = m\omega_0^2\boldsymbol{r}(t)$ acting on the bound electron with a resonant frequency ω_0.

where N is the volume electron density. Combining Eq. 2.14 and 2.15, the equation of motion can be rewritten to:

$$\frac{\partial^2 \boldsymbol{P}}{\partial t^2} + \gamma \frac{\partial \boldsymbol{P}}{\partial t} = \epsilon_0 \omega_p^2 \boldsymbol{E}(t) \tag{2.16}$$

where the plasma frequency is introduced $\omega_p = \sqrt{\frac{Nq^2}{\epsilon_0 m}}$, with ϵ_0 the electric permittivity of free space. Note that ω_p is the resonance frequency of the natural oscillation of free electron gas, so-called plasma, when there is no external driving force[7]. The plasma frequency sets a barrier to incident radiations, known as screening effect. This involves that electromagnetic waves having frequency shorter than plasma frequency ω_p will be reflected by the electron cloud, only those having higher frequencies can be transmitted through. The plasma frequency ω_p (rad/s) is usually represented via plasmon energy $\hbar\omega_p$ (eV), as listed in Table. 2.1 for common plasmonic metals.

In frequency domain, Eq. 2.16 becomes

$$\begin{aligned} \frac{\partial^2 [\boldsymbol{P}(\omega) e^{-i\omega t}]}{\partial t^2} + \gamma \frac{\partial [\boldsymbol{P}(\omega) e^{-i\omega t}]}{\partial t} &= \epsilon_0 \omega_p^2 \boldsymbol{E}(\omega) e^{-i\omega t} \\ -\omega^2 \boldsymbol{P}(\omega) - i\omega\gamma \boldsymbol{P}(\omega) &= \epsilon_0 \omega_p^2 \boldsymbol{E}(\omega) \end{aligned}$$

And finally, we obtain:

$$\boldsymbol{P}(\omega) = \epsilon_0 \frac{\omega_p^2}{-\omega^2 - i\gamma\omega} \boldsymbol{E}(\omega) = \epsilon_0 \chi^{(1)} \boldsymbol{E}(\omega) \tag{2.17}$$

with the frequency-dependent linear susceptibility $\chi^{(1)} = \omega_p^2/(-\omega^2 - i\gamma\omega)$. The dielectric function is thus expressed as

$$\epsilon(\omega) = 1 + \chi^{(1)} = 1 + \frac{\omega_p^2}{-\omega^2 - i\gamma\omega} = 1 + \frac{\omega_p^2}{G_D} \tag{2.18}$$

where $G_D = -\omega^2 - i\gamma\omega$ denotes the Drude oscillation term [8].

Eq. 2.18 allows to calculate the dielectric function ϵ from the frequency of the incident field ω. In Fig. 2.1, the dielectric function of silver ϵ_{Ag} measured by Johnson and Christy [74] (solid lines) is compared with ϵ_D, a dielectric function calculated based on Eq. 2.18 using plasmon energy $\hbar\omega_p$=8.9 eV [72] and scattering time τ_{sc}=40 fs [74]. It is seen that the Drude model well estimates the dielectric function of silver in the infrared spectral range (<1.5 eV). However, the deviation between the model and the experiment increases in the visible range, especially for the real part of the dielectric function Re(ϵ_{Ag}). The simple Drude model also fails to illustrate the interband transition in silver, which occurs at 4 eV. Other complex oscillation terms must be included to simulate the interband transition.

[7] Plasma frequency is found by solving the equation of motion of electron without external driving force and scattering: $m\frac{\partial^2 x}{\partial t^2} = -qE$, where x is the displacement of electron and $E = \frac{Nqx}{\epsilon_0}$ is the electric field generated by the charged slab Nqx.

[8] Another difference between Lorentz and Drude models. In the Lorentz model, the oscillation term becomes $\omega_0^2 - \omega^2 - i\gamma\omega$ with the resonant frequency ω_0.

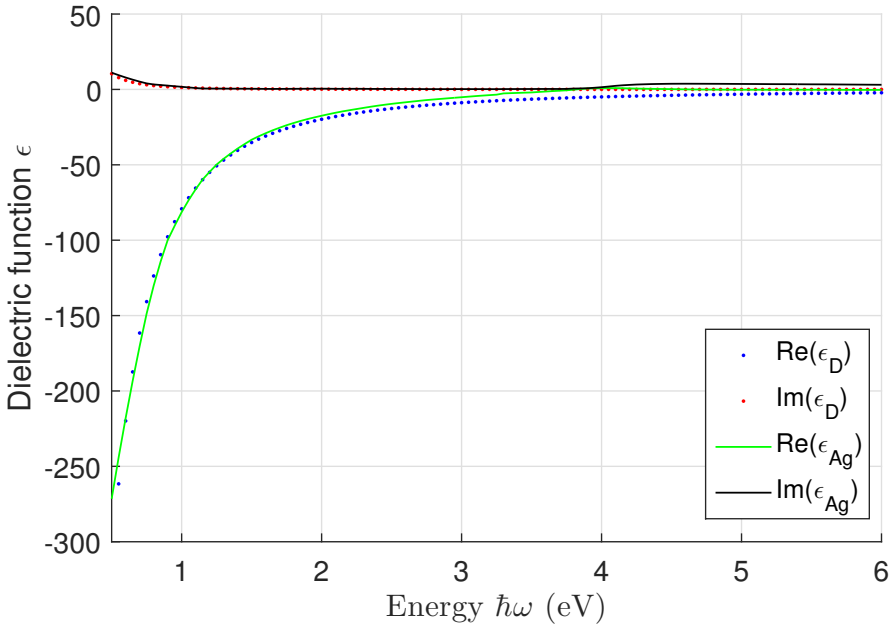

Figure 2.1 – Comparison of the dielectric function of silver estimated by Drude model (dots) and that measured experimentally on a 30 nm silver thin film (solid lines) [74]

2.2.2 Linear magneto-optical effects

Here the Drude model is used to describe linear magneto-optical effects for magnetized metallic interfaces. While the magnetic field component of the incident electromagnetic field hardly produces any optical effect, a strong external magnetic field $\boldsymbol{B}_{ext}$ can exert a Lorentz force on the moving electrons, and hence introduce an additional term to the equation of motion of a free electron according to the Drude model [82]:

$$-\frac{q}{m}\left[\boldsymbol{E}(t)+\frac{d\boldsymbol{r}}{dt}\times\boldsymbol{B}\right]=\frac{d^2\boldsymbol{r}}{dt^2}+\gamma\frac{d\boldsymbol{r}}{dt} \tag{2.19}$$

In Cartesian coordinates, this equation extends into:

$$\begin{aligned}
&\frac{\partial^2 x}{\partial t^2}+\gamma\frac{\partial x}{\partial t}+\frac{q}{m}\left(\frac{\partial y}{\partial t}B_z+\frac{\partial z}{\partial t}B_y\right)=-\frac{q}{m}E_x e^{-i\omega t}\\
&\frac{\partial^2 y}{\partial t^2}+\gamma\frac{\partial y}{\partial t}+\frac{q}{m}\left(\frac{\partial z}{\partial t}B_x+\frac{\partial x}{\partial t}B_z\right)=-\frac{q}{m}E_y e^{-i\omega t}\\
&\frac{\partial^2 z}{\partial t^2}+\gamma\frac{\partial z}{\partial t}+\frac{q}{m}\left(\frac{\partial x}{\partial t}B_y+\frac{\partial y}{\partial t}B_x\right)=-\frac{q}{m}E_z e^{-i\omega t}
\end{aligned} \tag{2.20}$$

We look for the solution in the form $\boldsymbol{r}(t)=(x_0,y_0,z_0)e^{-i\omega t}$, where $x_0=L_x/L_0$, $y_0=L_y/L_0$ and $z_0=L_z/L_0$ [82]. We have thus:

$$L_0=G_D\left[G_D^2-\left(\frac{\omega q}{m}\right)^2(B_x^2+B_y^2+B_z^2)\right] \tag{2.21}$$

and

$$\begin{aligned} L_x = \frac{q}{m}\Big\{ & \Big[G_D^2 - \Big(\frac{\omega q}{m}B_x\Big)^2\Big]E_x \\ & - \Big[iG_D\frac{\omega q}{m}B_z - \Big(\frac{\omega q}{m}\Big)^2 B_xB_y\Big]E_y \\ & - \Big[iG_D\frac{\omega q}{m}B_y - \Big(\frac{\omega q}{m}\Big)^2 B_xB_z\Big]E_z\Big\} \end{aligned} \tag{2.22}$$

where G_D is the Drude coefficient defined in section 2.2.1. L_y and L_z can be written in a similar manner by cyclic permutation.

In a magnetic medium, the off-diagonal components in the linear susceptibility tensor $\chi^{(1)}$ become non-zero and depends on $\boldsymbol{B} = (B_x, B_y, B_z)$, with the symmetry $\chi_{ij}(B_x, B_y, B_z) = -\chi_{ji}(B_x, B_y, B_z)$ [83]. Thus we have the polarization which can be written as

$$\begin{bmatrix} P_x \\ P_y \\ P_z \end{bmatrix} = \epsilon_0 \begin{bmatrix} \chi_{xx} & \chi_{xy}(B_z) & \chi_{xz}(B_y) \\ -\chi_{xy}(B_z) & \chi_{yy} & \chi_{yz}(B_x) \\ -\chi_{xz}(B_y) & -\chi_{yz}(B_x) & \chi_{zz} \end{bmatrix} \begin{bmatrix} E_x \\ E_y \\ E_z \end{bmatrix} \tag{2.23}$$

As the polarization is a volume density of electric dipole moments, shown in Eq. 2.15, the tensor components of the susceptibility $\chi^{(1)}$ can be derived from $\boldsymbol{r} = (x_0, y_0, z_0)$. For example, when a constant external magnetic field $\boldsymbol{B} = (B_x, B_y, B_z)$ is applied, the three non-zero tensor components in the first row are

$$\begin{aligned} \chi_{xx} &= \frac{Nq^2}{\epsilon_0 m L_0}\Big[G_D^2 - \Big(\frac{\omega q}{m}B_x\Big)^2\Big] \\ \chi_{xy} &= \frac{Nq^2}{\epsilon_0 m L_0}\Big[-iG_D\frac{\omega q}{m}B_z - \Big(\frac{\omega q}{m}\Big)^2 B_xB_y\Big] \\ \chi_{xz} &= \frac{Nq^2}{\epsilon_0 m L_0}\Big[iG_D\frac{\omega q}{m}B_y - \Big(\frac{\omega q}{m}\Big)^2 B_zB_x\Big] \end{aligned} \tag{2.24}$$

The other tensor elements can be written in the same manner. We see that besides the plasma frequency $\omega_p = \sqrt{Nq^2/(\epsilon_0 m)}$ and the Drude oscillation term $G_D = -\omega^2 - i\gamma\omega$, the off-diagonal element χ_{ij} also depends on the cyclotron frequency $\omega_L = qB/m$, which makes the change of sign ($\omega_L \longrightarrow -\omega_L$) upon the reversal of the external magnetic field $\boldsymbol{B} \longrightarrow -\boldsymbol{B}$.

2.2.3 Magneto-optical Kerr effect (MOKE)

Eq. 2.24 reveals that by an external magnetic field, the polarization or intensity of light can be modified. For light reflected on a magnetized surface, the phenomenon refer to the magneto-optical Kerr effect (MOKE) [84]. The similar magneto-optical effect observed in transmission is called Faraday effect [85].

In general, there are three configurations of MOKE, according to the mutual orientations of the magnetization $\boldsymbol{M}$, surface and the plane of incidence. Fig. 2.2 shows the magneto-optical configurations in Cartesian coordinates: (a) polar MOKE, where M_z is normal to the magnetized surface (b) longitudinal MOKE, where the in-plane M_x

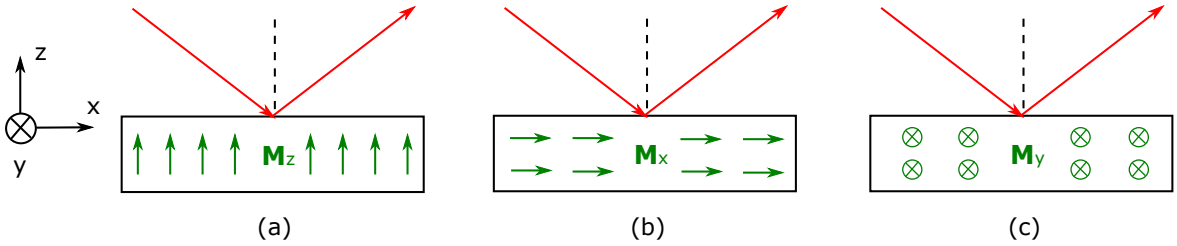

Figure 2.2 – Three configurations of magneto-optical Kerr effects: (a) polar, (b) longitudinal and (c) transversal. Plane of incidence is the xz plane.

is parallel to the plane of incidence, and (c) transversal MOKE, where M_y is perpendicular to the plane of incidence. A table for the dielectric tensors $\boldsymbol{\epsilon}(\omega)$ in each case is presented in Tab. 2.2. The non-magnetic diagonal component ϵ remains regardless of the magnetization $\boldsymbol{M}$. The magnetic off-diagonal components are written as the first approximation with respect to M, for example $\epsilon_{xy}M_z$. In the polar and longitudinal MOKE, the polarization changes and is quantified by the complex Kerr rotation $\Phi = \Phi' + i\Phi''$, where Φ' is the real part of Kerr rotation and Φ'' is the ellipticity. The Kerr rotation angle in the polar configuration is about one order of magnitude larger than that in the longitudinal geometry [86]. The notation of the reflectivity, r_{ps} for example, stands for the reflectivity of a s-polarized light which initially has incident polarization p. In the polar configuration, $r_{sp} = r_{ps}$. In contrast, $r_{sp} = -r_{ps}$ in the longitudinal MOKE [87]. In the transversal geometry, only r_{pp} depends on M, thus gives the magnetization-induced change in the intensity of reflectivity. Besides these three MOKE geometries, hybrid cases occur when $\boldsymbol{M}$ is tilted. In such cases, both the polarization and intensity of reflected light could change upon the reversal of $\boldsymbol{M}$.

	Polar	**Longitudinal**	**Transversal**
$\boldsymbol{\epsilon}(\omega)$	$\begin{bmatrix} \epsilon & \epsilon_{xy}M_z & 0 \\ -\epsilon_{xy}M_z & \epsilon & 0 \\ 0 & 0 & \epsilon \end{bmatrix}$	$\begin{bmatrix} \epsilon & 0 & 0 \\ 0 & \epsilon & \epsilon_{yz}M_x \\ 0 & -\epsilon_{yz}M_x & \epsilon \end{bmatrix}$	$\begin{bmatrix} \epsilon & 0 & \epsilon_{xz}M_y \\ 0 & \epsilon & 0 \\ -\epsilon_{xz}M_y & 0 & \epsilon \end{bmatrix}$
$\boldsymbol{M}_r$	$\begin{bmatrix} r_{pp} & r_{ps}(M_z) \\ r_{sp}(M_z) & r_{ss} \end{bmatrix}$	$\begin{bmatrix} r_{pp} & r_{ps}(M_x) \\ r_{sp}(M_x) & r_{ss} \end{bmatrix}$	$\begin{bmatrix} r_{pp}(M_y) & 0 \\ 0 & r_{ss} \end{bmatrix}$
Signal	$\Phi = \frac{r_{ps}(M_z)}{r_{pp}}$	$\Phi = \frac{r_{ps}(M_x)}{r_{pp}}$	$\frac{\Delta R_{pp}(M_y)}{R_{pp}}$

Table 2.2 – The dielectric tensors $\boldsymbol{\epsilon}(\omega)$, reflectivity matrix $\boldsymbol{M}_r$ and reflected signal for three different configurations of MOKE. The off-diagonal components of the dielectric tensor $\boldsymbol{\epsilon}(\omega)$ depend linearly on magnetization M. The table is adapted from Ref. [3]

2.3 Nonlinear magneto-optical responses

The previous section has shown that the motion of electrons driven by an external electromagnetic field determine the optical responses of the materials. Following this approach, the nonlinear optical responses can be attributed to a nonlinear motion of electrons. It is analog to an anharmonic oscillation of a swing or a pendulum, where strong driving force results in nonlinearity.

2.3.1 Model of anharmonic oscillation and SHG

Perturbation of potential

To illustrate for the anharmonic oscillation, let us start with a simple example of a spring oscillating along z direction. The restoring force in this case is $F_{\text{restoring}} = -Kz$, where K is the spring constant. The harmonic binding potential is thus:

$$V(z) = -\int F_{\text{restoring}} dz = \frac{1}{2}Kz^2 = \frac{1}{2}m\omega_0^2 z^2 \tag{2.25}$$

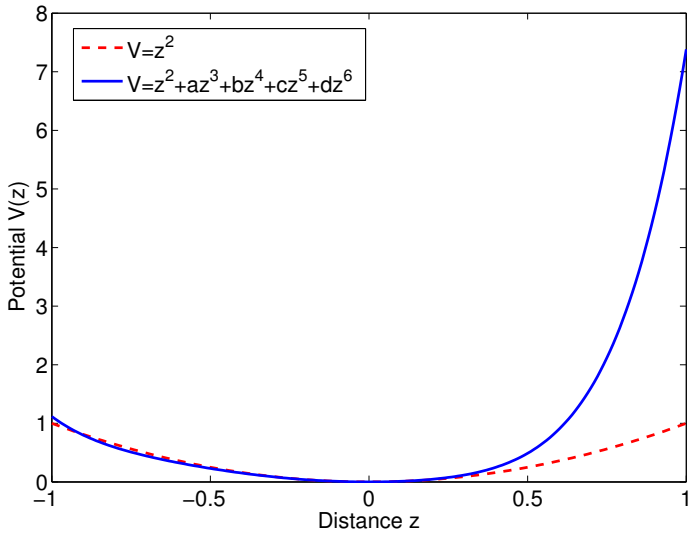

Figure 2.3 – Illustrations of the harmonic potential (red dashed line) and the power expansion of the potential (blue solid line). For large positive z, the blue line deviates from the parabolic curve and approaches the case of a potential wall.

When the oscillation encounters a potential wall, $V(z)$ deviates from the parabolic shape and can be approximated by the power series

$$V(z) = \frac{1}{2}m\omega_0^2 z^2 + \frac{1}{3}maz^3 + \frac{1}{4}mbz^4 + \dots \tag{2.26}$$

where a and b are the perturbation factors. Fig. 2.3 illustrates the parabolic potential $V(z) \propto z^2$ of a harmonic oscillation, and the potential of an anharmonic oscillation

approximated by power expansion. The force in this case is

$$F(z) = -\frac{\partial V(z)}{\partial z} = -m\omega_0^2 z - maz^2 - mbz^3 - \dots \tag{2.27}$$

We can note that the inversion center in centrosymmetric crystals[40] causes the spatial symmetry in potential $V(z) = V(-z)$. Eq. 2.26 and 2.27 show that the symmetry of potential happens only if

$$\begin{aligned} V(z) &= \frac{1}{2}m\omega_0^2 z^2 + \frac{1}{4}mbz^4 + \dots \\ \text{and} \quad F(z) &= -\frac{\partial V(z)}{\partial z} = -m\omega_0^2 z - mbz^3 \end{aligned} \tag{2.28}$$

meaning that the even-order anharmonic oscillations (z^2, z^4, etc.) vanish. In contrast, non-centrosymmetric structures permit both even and odd harmonics of the fundamental frequency.

Anharmonic oscillation of a free electron

The motion of a free electron, driven by an external electric field and stopped by a surface (potential wall), is written in Eq. 2.29 below [88]. The charge is free, so there is no resonant frequency ω_0 and the restoring force in Eq.2.27 is reduced to perturbation force $F_{\text{perturbation}} = -amz^2$. Thus the motion equation of a free electron gives:

$$\begin{aligned} m\frac{\partial^2 z}{\partial t^2} &= F_{\text{driving}} + F_{\text{damping}} + F_{\text{perturbation}} \\ &= -qE - \gamma m\frac{\partial z}{\partial t} - amz^2 \end{aligned} \tag{2.29}$$

where γ is the damping constant, an inversion of scattering time τ_{sc}, and a the perturbation constant. Thus, Eq. 2.29 can be rewritten as:

$$-\frac{q}{m}E = \frac{\partial^2 z}{\partial t^2} + \gamma\frac{\partial z}{\partial t} + az^2 \tag{2.30}$$

According to Euler's formula, a monochromatic time-dependent oscillation $z_\omega(t) = z(\omega)\cos(-\omega t)$ with real $z(\omega)$ is written as:

$$\begin{aligned} z_\omega(t) &= \frac{1}{2}z(\omega)\mathrm{e}^{-i\omega t} + \frac{1}{2}z(\omega)\mathrm{e}^{i\omega t} \\ &= \frac{1}{2}z(\omega)\mathrm{e}^{-i\omega t} + c.c. \end{aligned} \tag{2.31}$$

where *c.c.* denotes the complex conjugate. For the case of anharmonic oscillation, what we look for is a solution $z(t)$ which is a linear combination of oscillations at fundamental frequency ω and its harmonics 2ω, 3ω, etc. Thus we can write the series of $z(t)$ as

$$\begin{aligned} z(t) &= \Lambda z_\omega(t) + \Lambda^2 z_{2\omega}(t) \\ z(t) &= \Lambda\Big[\frac{1}{2}z(\omega)\mathrm{e}^{-i\omega t} + c.c.\Big] + \Lambda^2\Big[\frac{1}{2}z(2\omega)\mathrm{e}^{-i2\omega t} + c.c.\Big] \end{aligned} \tag{2.32}$$

where Λ is a scaling factor applied on the external electric field $E(t) = \Lambda E_\omega(t)$. The scaling factor helps to separate the terms related to the first-order polarization ($P(\omega) \propto \Lambda E(\omega)$), the second-order polarization ($P(2\omega) \propto \Lambda^2 E(\omega)$), the third-order polarization ($P(3\omega) \propto \Lambda^3 E(\omega)$) and so on. Putting Eq. 2.32 into Eq. 2.30 gives:

$$\begin{aligned} -\frac{q}{m}\Lambda E_\omega(t) = \Lambda\frac{\partial^2 z_\omega(t)}{\partial t^2} + \Lambda\gamma\frac{\partial z_\omega(t)}{\partial t} \\ + \Lambda^2\frac{\partial^2 z_{2\omega}(t)}{\partial t^2} + \Lambda^2\gamma\frac{\partial z_{2\omega}(t)}{\partial t} + a\Lambda^2 z_\omega^2(t) \\ + \Lambda^3 ... + \Lambda^4 ... \end{aligned} \tag{2.33}$$

In the next part, we will separate the terms scaling with Λ and Λ^2, which respectively correspond to the linear and the second-order oscillations.

Scaling with Λ - Linear harmonic oscillation

Based on Eq. 2.33, the following terms are scaled with factor Λ:

$$-\frac{q}{m}E_\omega(t) = \frac{\partial^2 z_\omega(t)}{\partial t^2} + \gamma\frac{\partial z_\omega(t)}{\partial t}$$

similar to the equation of motion Eq. 2.14 in section 2.2.1. In the frequency domain, this equation becomes:

$$\begin{aligned} -\frac{q}{m}E(\omega) &= -\omega^2 z(\omega) - i\omega\gamma z(\omega) \\ &= z(\omega)[-\omega^2 - i\gamma\omega] \end{aligned} \tag{2.34}$$

and finally we have the frequency-dependent solution:

$$z(\omega) = -\frac{q}{m} \times \frac{E(\omega)}{-\omega^2 - i\gamma\omega} \tag{2.35}$$

From Eq. 2.35 and Eq. 2.15, we can deduce the relation between the linear polarization $P(\omega)$ and the oscillation of electron $z(\omega)$:

$$P(\omega) = -Nqz(\omega) = N\frac{q^2}{m} \times \frac{E(\omega)}{-\omega^2 - i\gamma\omega} \tag{2.36}$$

where N is the volume density of electrons. Eq. 2.36 presents the same linear polarization $P(\omega)$ as in Eq. 2.17. Recall that the relation between $P(\omega)$ and $E(\omega)$ is expressed by the Lorentzian complex function of linear optical susceptibility $\chi^{(1)} = \frac{\omega_p^2}{-\omega^2 - i\gamma\omega} = \frac{\omega_p^2}{G(\omega)}$, where $G_D(\omega)$ is the frequency-dependent Drude oscillation term.

Scaling with Λ^2 - Second-order anharmonic oscillation

The terms scaled with factor Λ^2 in Eq. 2.33 include:

$$-az_\omega^2(t) = \frac{\partial^2 z_{2\omega}(t)}{\partial t^2} + \gamma\frac{\partial z_{2\omega}(t)}{\partial t} \tag{2.37}$$

where the term $z_\omega^2(t)$ can be derived from Eq. 2.31

$$z_\omega^2(t) = \frac{1}{4}z^2(\omega)\mathrm{e}^{i2\omega t} + \frac{1}{4}z^2(\omega)\mathrm{e}^{-i2\omega t} + \frac{1}{2}z^2(\omega) \tag{2.38}$$

For the oscillation at the double-frequency 2ω, we consider only the part with $\mathrm{e}^{-i2\omega t}$. The other components correspond to other second-order nonlinear processes; for example, the DC term $1/2z^2(\omega)$ is related to the rectification effect. Thus, we put $z_{2\omega}(t) = \frac{1}{2}z(2\omega)\mathrm{e}^{-i2\omega t}$ and $z_\omega^2(t) \approx \frac{1}{4}z^2(\omega)\mathrm{e}^{-i2\omega t}$ into Eq. 2.37 to have:

$$-\frac{a}{4}z^2(\omega) = -2\omega^2 z(2\omega) - i\gamma\omega z(2\omega) \tag{2.39}$$

With $z(\omega)$ from the linear oscillation in Eq. 2.35, Eq. 2.39 becomes:

$$\begin{aligned} -\frac{a}{4}z^2(\omega) &= -\frac{a}{4} \times \frac{q^2}{m^2} \times \frac{E^2(\omega)}{(-\omega^2 - i\gamma\omega)^2} \\ &= \frac{1}{2}(-4\omega^2 - i\gamma 2\omega)z(2\omega) = \frac{1}{2}G(2\omega)z(2\omega) \end{aligned} \tag{2.40}$$

where the Drude term at the double frequency is $G_D(2\omega) = -4\omega^2 - i\gamma 2\omega$. The solution for the second-order oscillation $z(2\omega)$ is thus given by

$$z(2\omega) = -\frac{a}{2} \times \frac{q^2}{m^2} \times \frac{E^2(\omega)}{G_D^2(\omega)G_D(2\omega)} \tag{2.41}$$

In the macroscopic regime, the Taylor expansion of the polarization is:

$$P = \Lambda P(\omega) + \Lambda^2 P(2\omega) + \dots \tag{2.42}$$

The second-order nonlinear polarization $P(2\omega)$ relates to the dipole moment at the double frequency 2ω and is written as:

$$P(2\omega) = -Nqz(2\omega) = \epsilon_0\chi^{(2)}E^2(\omega) \tag{2.43}$$

where the second-order nonlinear susceptibility $\chi^{(2)}$ is expressed by

$$\chi^{(2)} = \frac{a}{2} \times \frac{q}{m} \times \frac{\omega_p^2}{G_D^2(\omega)G_D(2\omega)} \tag{2.44}$$

Fig. 2.4 illustrates the trajectory of a free electron oscillating anharmonically with the external electric field. One can see that the second-order harmonics at double frequency $z(2\omega)$ (Eq. 2.41) is smaller than the oscillation at the fundamental frequency $z(\omega)$ (Eq. 2.35) by a factor of $\frac{aqE(\omega)}{2mG_D(\omega)G_D(2\omega)}$. Thus the nonlinear process is eligible only when the perturbation factor a and the driving field $E(\omega)$ are relatively large. That is why ultrashort laser pulses with high peak power are required in nonlinear optical generation processes.

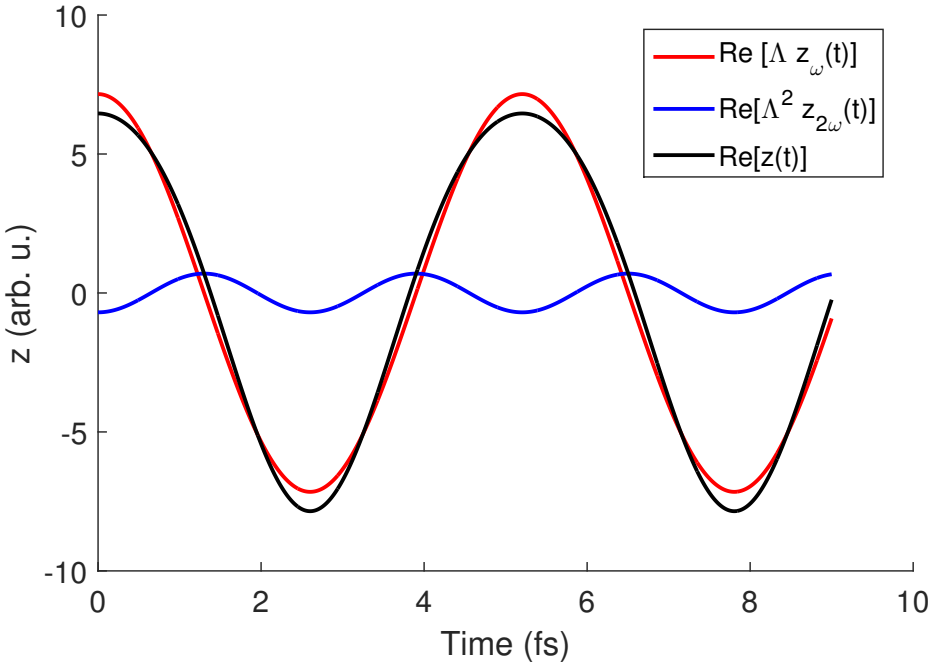

Figure 2.4 – Illustration for the anharmonic oscillation of a free electron. The trajectory of the electron has the form $z(t) = \Lambda z_\omega(t) + \Lambda^2 z_{2\omega}(t)$

SHG at the surface and interfaces

According to the electric dipole approximation above, second-order nonlinear optical processes (second harmonic generation - SHG, different harmonic generation - DFG, sum frequency generation - SFG) are prohibited in structures having center of inversion. Many metals have centrosymmetric cubic crystal structures. For example, the crystal structure of Au, Ag, Al, Cu, Ni is face-centered cubic (fcc), while Fe crystal is body-centered cubic (bcc) at room temperature. In these structures, SHG is supposed to be allowed exclusively where the inversion of spatial symmetry is broken, i.e. at the metallic surface and interfaces. However, besides the surface-limited SHG, there is a relatively weak SH emission occurring within the metallic bulks, which can only be explained by quadrupole mechanism[89–91]. In general, the SH polarization $\boldsymbol{P}(2\omega)$ in a centrosymmetric medium includes both the dipole surface term and the quadrupole bulk term [29, 92]

$$\begin{aligned} \boldsymbol{P}(2\omega) &= \boldsymbol{P}_{surf}(2\omega) + \boldsymbol{P}_{bulk}(2\omega) \\ &= \chi^{(2)}_{surf}\boldsymbol{E}(\omega)\boldsymbol{E}(\omega) + \chi^{(2)}_{bulk}\boldsymbol{E}(\omega)\nabla\boldsymbol{E}(\omega) \end{aligned} \tag{2.45}$$

where $\chi^{(2)}_{surf}$ and $\chi^{(2)}_{bulk}$ correspond to the surface and bulk second-order susceptibilities. The surface contribution $\boldsymbol{P}_{surf}(2\omega)$ occurs exclusively at the surface and interfaces of metal. In contrast, the nonlocal bulk source of SHG $\boldsymbol{P}_{bulk}(2\omega)$ is located within the metallic medium and proportional to the gradient of fundamental field $\nabla\boldsymbol{E}(\omega)$. The surface and bulk contributions depend on the shape of structures and the field distri-

bution. In thin films of gold, the surface contribution dominates over the bulk term [93]. In cobalt perforated layers, the strong field gradient caused by the surface plasmon polariton results in a significant bulk contribution in the magnetization-induced SHG [29]. Throughout this work, the dipole-allowed $\boldsymbol{P}_{surf}(2\omega)$ is considered the main source of SH emission.

2.3.2 Magnetization-induced Second Harmonic Generation

In space, the second-harmonic polarization is

$$P_i(2\omega) = \epsilon_0 \chi^{(2)}_{ijk} E_j(\omega) E_k(\omega) \tag{2.46}$$

where i, j, k denote Cartesian coordinates. Since $\chi^{(2)}_{ijk} = \chi^{(2)}_{ikj}$ due to the permutation symmetry, the susceptibility tensor in this case is a 3×6 tensors [86]:

$$\begin{pmatrix} P_x \\ P_y \\ P_z \end{pmatrix} = \epsilon_0 \begin{pmatrix} \chi_{xxx} & \chi_{xyy} & \chi_{xzz} & \chi_{xzy} & \chi_{xzx} & \chi_{xxy} \\ \chi_{yxx} & \chi_{yyy} & \chi_{yzz} & \chi_{yzy} & \chi_{yzx} & \chi_{yxy} \\ \chi_{zxx} & \chi_{zyy} & \chi_{zzz} & \chi_{zzy} & \chi_{zzx} & \chi_{zxy} \end{pmatrix} \begin{pmatrix} E_x E_x \\ E_y E_y \\ E_z E_z \\ 2E_y E_z \\ 2E_x E_z \\ 2E_x E_y \end{pmatrix} \tag{2.47}$$

Due to the geometry, among 18 components of $\chi^{(2)}$ tensor, there are 13 components that are odd to magnetization, i.e. $\chi^{odd}(-M) = -\chi^{odd}(M)$. The asymmetry leads to magnetization-induced change in the second-order polarization $\boldsymbol{P}(2\omega)$. The odd components χ^{odd} depend on M [37, 38], and they vanish if the structures are non-magnetic. The other $\chi^{(2)}$ components are even to magnetization, $\chi^{even}(M) = \chi^{even}(-M)$, and indifferent to the reversal of magnetization vector $\boldsymbol{M}$. The magnetic (odd) and non-magnetic (even) components of $\chi^{(2)}$ are

$$\begin{bmatrix} \chi_{xxx}(M_y) & \chi_{xyy}(M_y) & \chi_{xzz}(M_y) & \chi_{xzy}(M_z) & \chi_{xzx} & \chi_{xxy}(M_x) \\ \chi_{yxx}(M_x) & \chi_{yyy}(M_x) & \chi_{yzz}(M_x) & \chi_{yzy} & \chi_{yzx}(M_z) & \chi_{yxy}(M_y) \\ \chi_{zxx} & \chi_{zyy} & \chi_{zzz} & \chi_{zzy}(M_x) & \chi_{zzx}(M_y) & \chi_{zxy}(M_z) \end{bmatrix} \tag{2.48}$$

The SH output from a magnetized interface is the interference of non-magnetic and magnetic SH fields, denoted as $\boldsymbol{E}^{nm}_{2\omega}$ and $\boldsymbol{E}^{mag}_{2\omega}$, respectively.

$$\begin{aligned} I_{2\omega}(\pm M) &= \left| \boldsymbol{E}^{nm}_{2\omega} \pm \boldsymbol{E}^{mag}_{2\omega} \right|^2 \\ &= |\boldsymbol{E}^{nm}_{2\omega}|^2 + |\boldsymbol{E}^{mag}_{2\omega}|^2 \pm 2|\boldsymbol{E}^{nm}_{2\omega} \cdot \boldsymbol{E}^{mag}_{2\omega}| \cos\varphi \end{aligned} \tag{2.49}$$

where φ is the phase difference between the complex $\boldsymbol{E}^{nm}_{2\omega}$ and $\boldsymbol{E}^{mag}_{2\omega}$, as shown in the phasor diagram in Fig. 2.5. To measure the influence of the magnetization on the nonlinear emission, a nonlinear magnetic contrast [6, 7, 15] is defined as

$$\begin{aligned} \rho &= \frac{I_{2\omega}(+M) - I_{2\omega}(-M)}{I_{2\omega}(+M) + I_{2\omega}(-M)} \\ &= \frac{2|\boldsymbol{E}^{nm}_{2\omega} \cdot \boldsymbol{E}^{mag}_{2\omega}| \cos\varphi}{|\boldsymbol{E}^{nm}_{2\omega}|^2 + |\boldsymbol{E}^{mag}_{2\omega}|^2} \end{aligned} \tag{2.50}$$

The formulations of $I_{2\omega}(\pm M)$ and ρ above show how the far-field magnetization-induced SH signals depends on the phase φ. The SH magnetic contrast ρ becomes null when the phase difference $\varphi = \pi/2$, i.e. when $\boldsymbol{E}_{2\omega}^{nm}$ and $\boldsymbol{E}_{2\omega}^{mag}$ are orthogonal on the phase diagram.

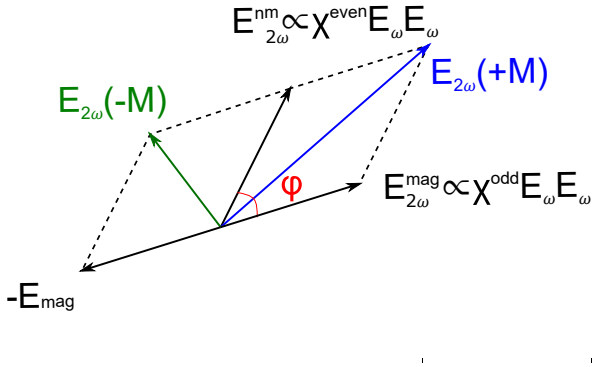

Figure 2.5 – Phasor diagram of the non-magnetic and magnetic SH fields, denoted as $\boldsymbol{E}_{2\omega}^{nm}$ and $\boldsymbol{E}_{2\omega}^{mag}$ respectively, and their interference $\boldsymbol{E}_{2\omega}(\pm M)$.

2.4 Surface plasmons

As we have seen in sections 2.2 and 2.3, the oscillation of free electrons driven by an electromagnetic field results in optical properties in metals. After having described magneto-optic properties, we now concentrate in surface plasmon excitation, and its coupling with electromagnetic surface waves, namely SPP[9]. In this section, the SPP field will be described as a solution of Maxwell's equations at the interface of metal and dielectric.

2.4.1 Propagating surface plasmon polaritons

Let us consider a system consisting of two semi-infinite media: metal ($\epsilon_m = \epsilon'_m + i\epsilon''_m$) and dielectric ($\epsilon_d$ real) in Fig. 2.6. SPP field is an electromagnetic field localized at the interface of these media, thus it follows Maxwell's equations (Eq. 2.1) and the material responses in (Eq. 2.8). When $\rho = 0$, we have the following homogeneous equations

$$\begin{aligned} \nabla \times \boldsymbol{E}_j &= -\mu_j \frac{\partial \boldsymbol{H}_j}{\partial t} \\ \nabla \times \boldsymbol{H}_j &= \epsilon_j \frac{\partial \boldsymbol{E}_j}{\partial t} \\ \nabla \cdot (\epsilon_j \boldsymbol{E}_j) &= 0 \\ \nabla \cdot \boldsymbol{H}_j &= 0 \end{aligned} \tag{2.51}$$

[9]The surface plasmon is different from the bulk plasmon, which is a longitudinal oscillation and can not be coupled to the transversal optical electromagnetic wave.

It is considered that $\mu_j = 1$ in the optical spectral range.

If the incident wave is p-polarized (TM), the field components in material j[10] is defined by:

$$\begin{aligned} \boldsymbol{E}_j &= \big(E_{j,x}, 0, E_{j,z}\big) e^{i(k_{j,x}x + k_{j,z}z - \omega t)} \\ \boldsymbol{H}_j &= \big(0, H_{j,y}, 0\big) e^{i(k_{j,x}x + k_{j,z}z - \omega t)} \end{aligned} \tag{2.52}$$

where $k_{j,x}^2 + k_{j,z}^2 = k_j^2 = \epsilon_j k_0^2 = \epsilon_j \big(\frac{\omega}{c}\big)^2$.

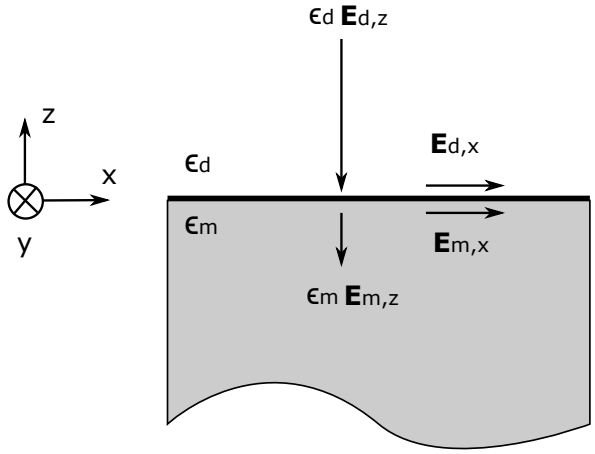

Figure 2.6 – The boundary conditions in the case of p-polarized electromagnetic fields at the interface between metal (ϵ_m) and dielectric (ϵ_d).

As there is no source in either medium, we consider the surface current density $K = 0$ and the conductivity $\sigma = 0$. The boundary conditions in Eq. 2.7 become:

$$\begin{aligned} E_{m,x} &= E_{d,x} \\ H_{m,y} &= H_{d,y} \\ \epsilon_m E_{m,z} &= \epsilon_d E_{d,z} \\ k_{m,x} &= k_{d,x} = k_x \end{aligned} \tag{2.53}$$

It is seen that while the tangential components E_x and H_y are continuous across the interface, the normal component E_z experiences a jump by a ratio of the two dielectric functions.

For plane waves, $\boldsymbol{k}_j \cdot \boldsymbol{E}_j = 0$, or we have

$$\begin{aligned} k_x E_{m,x} + k_{m,z} E_{m,z} &= 0 \\ k_x E_{d,x} + k_{d,z} E_{d,z} &= 0 \end{aligned} \tag{2.54}$$

Along with 2.53, we have

$$\frac{k_{d,z}}{\epsilon_d} = \frac{k_{m,z}}{\epsilon_m} \tag{2.55}$$

[10]The subscription j indicates the medium, either m if metal, or d if dielectric.

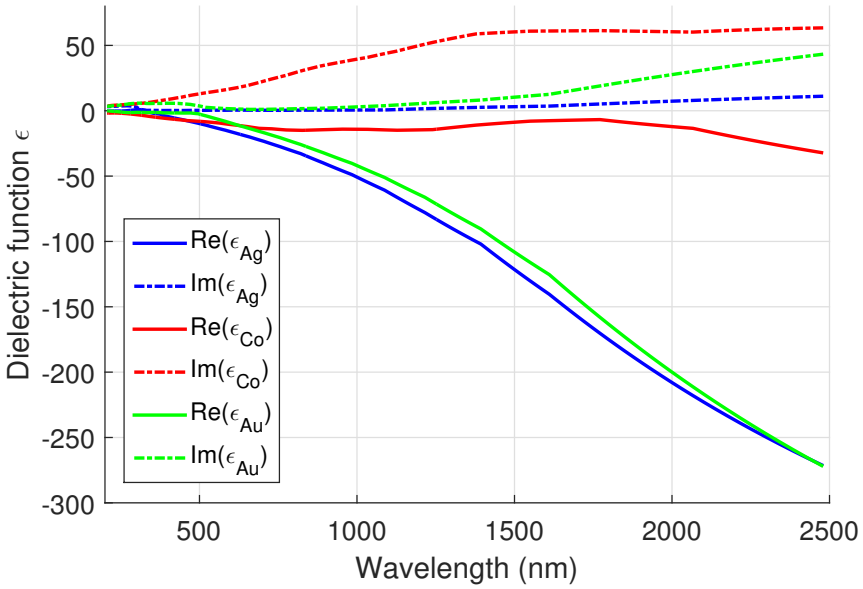

Figure 2.7 – The real and imaginary parts of the dielectric functions of silver (blue), gold (green) [74] and cobalt (red) [94], the three metals used extensively in this work.

By definition, we have

$$k_x^2 + k_{m,z}^2 = \epsilon_m k_0^2$$
$$k_x^2 + k_{d,z}^2 = \epsilon_d k_0^2$$

Subtracting the two equations above and applying the relation in Eq. 2.55, we have the dispersion relations for k_z

$$\begin{aligned} k_{m,z} &= \frac{\omega}{c} \cdot \frac{\epsilon_m}{\sqrt{\epsilon_m + \epsilon_d}} \\ k_{d,z} &= \frac{\omega}{c} \cdot \frac{\epsilon_d}{\sqrt{\epsilon_m + \epsilon_d}} \end{aligned} \tag{2.56}$$

and for k_x

$$k_x = \frac{\omega}{c} \sqrt{\frac{\epsilon_m \epsilon_d}{\epsilon_m + \epsilon_d}} \tag{2.57}$$

Since $\epsilon_m = \epsilon_m' + i\epsilon_m''$ is complex, we have the complex wavevector components $k_x = k_x' + ik_x''$ and $k_z = k_z' + ik_z''$. Fig. 2.7 shows the dielectric functions of silver, gold and cobalt, the three metals used extensively in this work. The dielectric function of noble metals [74], such as gold and silver, have large negative real part ϵ_m' and low positive imaginary part ϵ_m'' in the visible and near-infrared spectral range, making $k_x > \omega/c$ and $k_{m,z}$, $k_{d,z}$. As a metal, cobalt also has negative real part of dielectric function [94], but the large imaginary part makes it lossy in the optical region.

One can describe the behaviour of the SPP field from the SPP wavevector components in Eq. 2.56 and 2.57. The SPP field propagates along the interface of metal/dielectric with inplane wavevector $k_{spp} = k_x = n_{sp} k_0$, where n_{sp} is the effective refractive in-

dex of SPP. The SPP wavelength is $\lambda_{spp} = 2\pi/k'_x$, and the propagation length[11] is $L_{spp} = 1/k''_x$. Along the normal direction, SPP field decays into both media by a factor $\big(\exp -|k_{j,z}|z\big)$, leading to a "bound" mode, where the field is strongly concentrated near the interface. The $1/e$ decay length of the field into metal, called "skin depth", is $\delta_{skin} = 1/|k_{m,z}|$, and the decay length into the dielectric medium is $\delta_d = 1/|k_{d,z}|$. It is noteworthy that the penetration depth of power into metals is a half of the skin depth $\delta_p = \delta_{skin}/2 = 1/2|k_{m,z}|$. Inserting these notations to Eq. 2.52, we can write out the SPP fields in metal

$$\begin{aligned} \boldsymbol{E}_m &= \Big(E_0, 0, -\frac{k_x}{k_{m,z}} E_0\Big) e^{ik'_x x - i\omega t} e^{-\frac{x}{L_{spp}} - \frac{z}{\delta_{skin}}} \\ \boldsymbol{H}_m &= \Big(0, \frac{\omega}{c} \cdot \frac{\epsilon_m}{k_{m,z}} E_0, 0\Big) e^{ik'_x x - i\omega t} e^{-\frac{x}{L_{spp}} - \frac{z}{\delta_{skin}}} \end{aligned} \tag{2.58}$$

Similarly, the SPP fields in dielectric can be written replacing ϵ_m by ϵ_d, $k_{m,z}$ by $k_{d,z}$, and δ_{skin} by δ_d. Fig. 2.8 shows the vector field of SPP at gold/air interface at the wavelength 1560 nm.

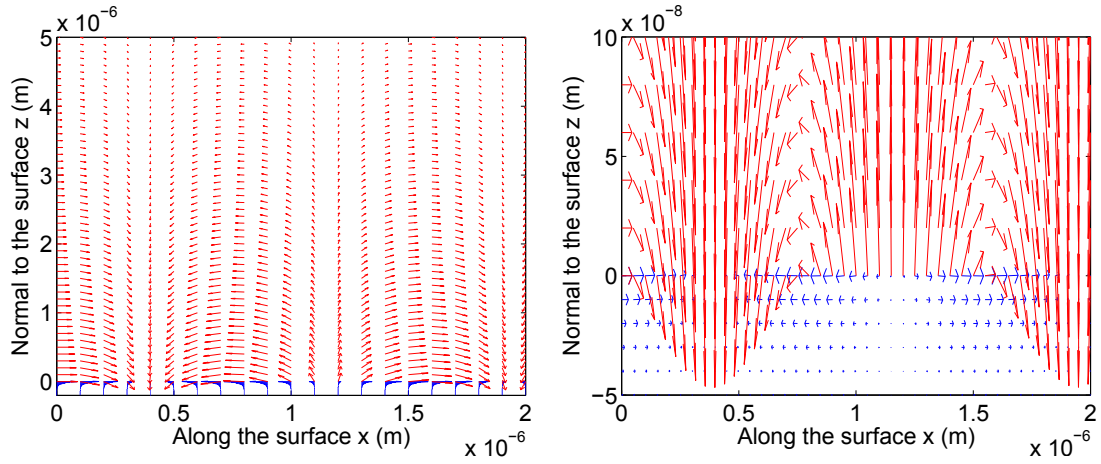

(a) (b)

Figure 2.8 – The vector field of SPP localized at gold/air interface ($z = 0$) at the wavelength 1560 nm. The red vectors illustrate SPP field in the air. The blue vectors are SPP in gold. (a) The extension of SPP in both media. The skin depth for electric field is twice higher than the penetration depth of intensity. (b) A zoom-in to the interface shows the flow of electric field.

If the incident electromagnetic wave is s-polarized (TE), E_y is continuous across the boundary, and we can no longer derive the dispersion relation in Eq. 2.53. Equivalent conditions can be achieved for H_x and H_z only if one of the material has negative real part of μ.

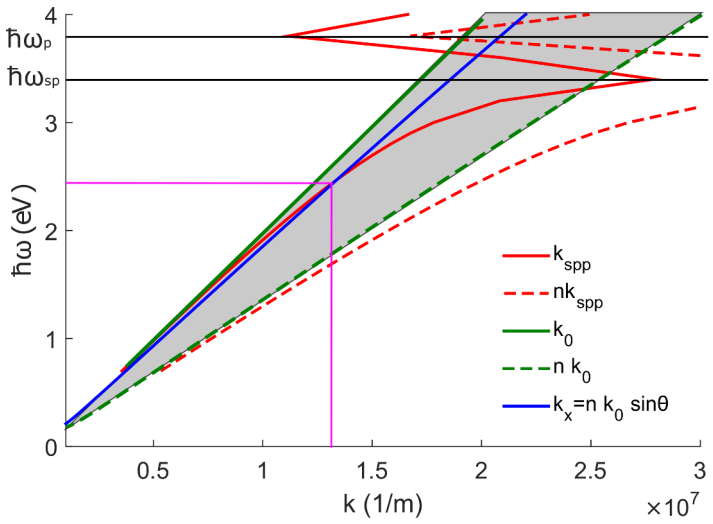

Figure 2.9 – Dispersion relations of k_{spp} at silver/air interface (red solid line), nk_{spp} at silver/substrate interface (red dashed line), light line k_0 in the air (green solid line), light line nk_0 in the substrate (green dashed line) and the inplane wavevector k_x at the angle of incidence $\theta = 47$ deg (blue line). Magenta lines mark the coupling between the incident k_x and the k_{spp} at silver/air interface.

2.4.2 Excitation of SPP

The dispersion relation in Eq. 2.53 is plotted in Fig. 2.9. To the right of the light line $n_d k_0 = \sqrt{\epsilon_d} k_0$, which is simply k_0 in the air (green solid line), it is the region for non-radiative mode. To the left of the light line, the mode is radiative (leaky) [2, 95]. The dispersion relation of SPP is presented by the red solid curve of $k_{spp} = \sqrt{\epsilon_m \epsilon_d/(\epsilon_m + \epsilon_d)} k_0$. We note a situation when $\epsilon_m + \epsilon_d \longrightarrow 0$ in Eq. 2.57, $k_{spp} = k_x$ becomes very large. In this case, the replacement of $\epsilon_m \approx \epsilon'_m \approx -\epsilon_d$ into $\omega^2 = \omega_p^2/(1 - \epsilon_m)$ in the Drude model[12] will give $\omega \longrightarrow \omega_{sp} = \omega_p/\sqrt{1 + \epsilon_d}$. ω_{sp} is called surface plasma frequency, and is recognized by a bend backwards of k_{spp} (red solid line) at $\hbar\omega_{sp} = 3.4$ eV. ω_{sp} shows the limit of the wavevector k_{spp} achievable in an experiment[13]. Beyond this value, the mode is strongly localized inside metal and the loss is high. When the frequency increases further, reaching the plasma frequency ω_p, the mode is called Brewster mode. It is no longer a surface mode [62, 96] and the frequency is not in the optical range. Thus, we will limit the discussion to the low-energy branch of the k_{spp}.

Within the range of low frequency $\omega < \omega_{sp}$, k_{spp} is always larger than the light line k_0, thus it is impossible to directly couple the incident light to the surface plasmons. In order to excite surface plasmon by light, it is essential to compensate the difference between the light line and the k_{spp}. Here I discuss two main approaches that will be applied in our measurements, prism coupling and grating coupling.

[11] The propagation length for the intensity (or power) is $1/2k''_x$.

[12] Eq. 2.18 when the damping constant $\gamma = 0$

[13] In reality, the interband transition and non-zero damping constant $\gamma \neq 0$ bring down the asymptote of k_{spp}, i.e. $\omega_{sp} < \omega_p/\sqrt{1 + \epsilon_d}$

Prism coupling

Since a prism (or substrate) has dielectric constant ϵ_s larger than ϵ_d in Eq. 2.53, the light line will be tilted by $\sqrt{\epsilon_s/\epsilon_d}$, or simply $n = \sqrt{\epsilon_s}$ if $\epsilon_d = 1$. In Fig. 2.9, the tilted light line nk_0 is marked by the green dashed line. The grey region between the light line in the air k_0 and the light line in prism nk_0 shows the range of available k_{spp}. At a certain angle of incidence θ, the inplane component of incident wavevector $k_x = nk_0 \sin\theta$ (blue solid line) can match with the SPP wavevector k_{spp}, giving us

$$\begin{aligned} k_x &= k_{spp} \\ n\sin\theta &= \sqrt{\frac{\epsilon_m \epsilon_d}{\epsilon_m + \epsilon_d}} \end{aligned} \tag{2.59}$$

Based on this principle, several geometries have been deployed, such as Kretschmann configuration [97], Otto configuration [98], near-field objective (modified Kretschmann configuration) [2, 62, 99], as shown in Fig. 2.10. Regardless of the incident medium, the inplane wavevector k_x is preserved in these geometries, and only matched to the wavevector of the SPP field localized at the interface of metal/open-space (air) as in Eq. 2.59. It is impossible to couple to the SPP wave at metal/substrate interface because its wavevector nk_{spp} (red dashed line) is always to the right of the light line in the substrate nk_0 (green dashed line), as shown in Fig. 2.9. The limit of these geometries is the distance between the incident surface, where the incident light is reflected, and the surface where SPP is excited. In both conventional and modified Kretschmann configurations, this distance is the thickness of the metallic film, which allows efficient contact between the evanescent fields of the incident light and the SPP within the metal. Thus Kretschmann geometries cannot excite SPP in thick metallic films. The optimal thickness of the film is around 50 nm for the case of gold and silver [62, 95]. In contrast, in Otto arrangement, the limiting distance is the open-space gap between the prism and the metal film, which is within a few μm [62]. Otto configuration can be used to excite SPP at the surface of thick metallic films, but it requires precise mechanical adjustments.

The conventional Kretschmann-Raether geometry is used extensively in this work. In a general structure comprising three different media dielectric/metal/air with a sufficiently thin metallic layer, there are SP fields at both the metal/dieletric and the metal/air interfaces. The hybridization of these two SP fields gives rise to four SP modes [100, 101]. In the particular case of Kretschmann configuration, two symmetric modes [14, 101] are accessible within the metallic film, a bound mode and a leaky mode. The bound mode is non-radiative, meaning that the energy from substrate and air flows into the metallic film and gets absorbed. In contrast, the leaky mode can radiate towards the transparent substrate, causing radiative loss. Inspecting the angular dependence of the light going through the prism and reflected on the studied metallic layer, a drop of reflectivity is observed near the angle of total internal reflection[14]. This

[14]The total internal reflection angle here is meant for the transition from the dielectric to air, regardless of the metallic layer.

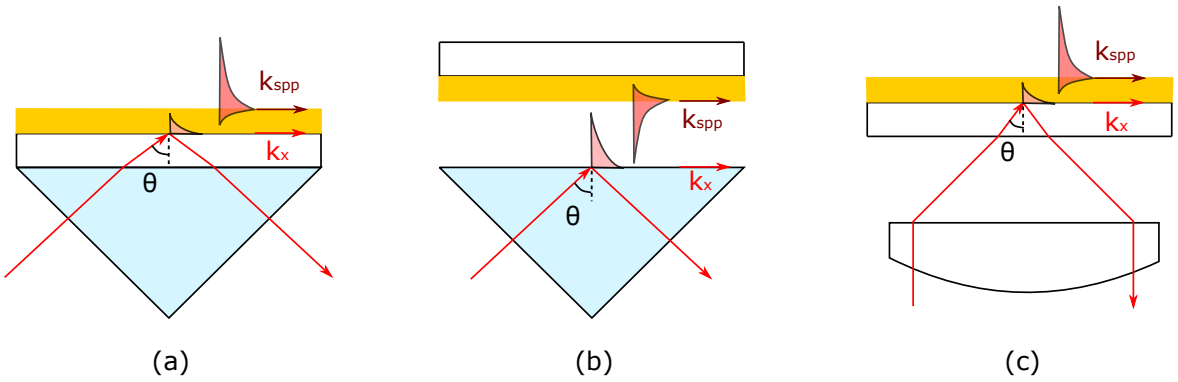

Figure 2.10 – Different geometries where SPP is excited by prism coupling: (a) conventional Kretschmann configuration (b) Otto configuration (c) modified Krestchmann configuration.

configuration is also called “attenuated total internal reflection" (ATIR) measurement. The dip in the angular spectrum of reflectivity is the result of the destructive interference of the aforementioned leaky (radiative) mode and the reflected light from the metal[2, 95].

When a thin film made of plasmonic metals is irradiated at the infrared spectral range, the minimum in the angular dependence of reflectivity is usually utilized as an indicator for the excitation of SPP field at the interface of metal/air. However, in cases of high optical loss, such as non-noble metals at high optical frequencies, the dip of reflectivity broadens and no longer signifies the SPP field enhancement [101, 102]. If one puts a near-field detector close to the open-surface (air side) of the metallic film and a far-field detector at the output of the prism, the angle where the near-field detector sees the highest SPP intensity is different from the angle where the far-field detector observes the minimal reflected light. This phenomenon can be seen using electromagnetic field simulations and has been proven experimentally [102]. It is explained by the discrepancy between the absorptive mode and SPP mode when the dispersion is significant.

A scan over the angles of incidence, i.e. the inplane wavevector k_x, helps to determine the phase-matching conditions of not only the linear SPP (as in Eq. 2.59) but also the nonlinear SPPs [6, 7, 15, 99, 103]. In the visible/infrared spectral range, the excitations of these SPPs occur at different angles because of the dispersion of the substrate. Thus, the SPPs excited in different regimes become distinguishable. This will be discussed in more details in chapter 3. Besides the applications in nanophotonics [3, 7, 30], the Kretschamnn geometry has also been employed for label-free sensing [104, 105], in which a minus change of refractive index of the environment above the metallic interface n_d is detected via a shift of k_x, namely the shift in either the angle of incidence or the incident wavelength.

Diffraction grating

Using a diffraction grating, we bridge the gap between the inplane wavevector by a multiple m of grating wavevector $G = 2\pi/\Lambda_G$, where Λ_G is the grating periodicity. Thus we have

$$\begin{aligned} k_x \pm mG &= k_{spp} \\ k_0 n \sin\theta_m \pm m\frac{2\pi}{\Lambda_G} &= k_0\sqrt{\frac{\epsilon_m\epsilon_d}{\epsilon_m+\epsilon_d}} \end{aligned} \tag{2.60}$$

with m is an integer. In this case, there can be several m and corresponding angles θ_m, where the k-matching condition is satisfied. An illustration of the SPP excitation using grating coupler is shown in Fig. 2.11. Similar principle can be applied to excite Wood's anomaly in periodic structures, which will be discussed in chapter 4. Unlike the prism coupling, grating coupling allows optical excitation of SPP from the air, which avoids the dispersion of the substrate. On the other hand, the fabrication of metallic gratings is more complicated than the continuous thin film.

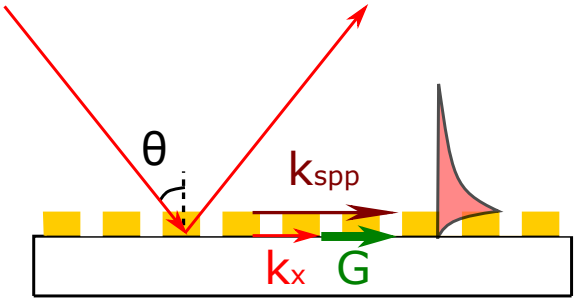

Figure 2.11 – Excitation of SPP by a diffraction grating.

2.4.3 Simulation of SPPs in multilayer structures

Matrix-Transfer-Method

Matrix-Transfer-Method (MTM) is a numerical method to solve Maxwell's equations for one-dimensional structures [61, 106–108], from which the optical responses (modes, reflectance, transmittance) are derived. In case of multilayer structures, the dielectric function $\epsilon(z)$ varies along z, normal to the film surface, and remains constant along x and y. The multilayer thin films are thus considered as 1D optical devices and can be well simulated using the MTM.

For 1D structure along z, k_x and k_y are continuous, while k_z is not. The transfer matrix M_j of each individual layer j describes the propagation of the (forward and backward) modes through the thickness L_j, taking into account the boundary conditions. In general, M_j is a 4×4 matrix; but for isotropic non-magnetic medium, it can be reduced to a 2×2 matrix as below.

$$\begin{bmatrix} E(z+L_j) \\ H(z+L_j) \end{bmatrix} = M_j \begin{bmatrix} E(z) \\ H(z) \end{bmatrix} \tag{2.61}$$

where

$$M_j = \begin{bmatrix} \cos(k_{z_j} L_j) & -i\frac{\epsilon_j k_0}{k_{z_j}} \sin(k_{z_j} L_j) \\ -i\frac{k_{z_j}}{\epsilon_j k_0} \sin(k_{z_j} L_j) & \cos(k_{z_j} L_j) \end{bmatrix} \tag{2.62}$$

The global transfer matrix for a system consisting of N_z layers is:

$$M_{global} = \prod_{j=1}^{N_z} M_j$$

and formulated as

$$M_{global} = \begin{bmatrix} M_{11} & M_{12} \\ M_{21} & M_{22} \end{bmatrix}$$

The amplitude transmittance t and reflectance r coefficients are then:

$$\begin{aligned} t &= 2k_R \frac{1}{(M_{11} + M_{12}k_T)k_R + M_{21} + M_{22}k_T} \\ r &= (\frac{M_{11} + M_{12}k_T)k_R - M_{21} + M_{22}k_T}{(M_{11} + M_{12}k_T)k_R + M_{21} + M_{22}k_T} \end{aligned} \tag{2.63}$$

where $k_R = \frac{k_{r,z}}{\epsilon_r k_0}$ and $k_T = \frac{k_{t,z}}{\epsilon_t k_0}$, with $k_{r,z}$ and $k_{t,z}$ respectively the z-coordinated wave vectors in reflection region (dielectric constant ϵ_r) and transmission region (dielectric constant ϵ_t). For a structure consisting of a single metallic layer, MTM describes Fabry-Pérot interferometer[109]. Regarding Eq. 2.61 and the boundary conditions in Eq. 2.53 that E_x, H_y and ϵE_z are continuous across the interface, the fields at the boundary between any two layers can be calculated.

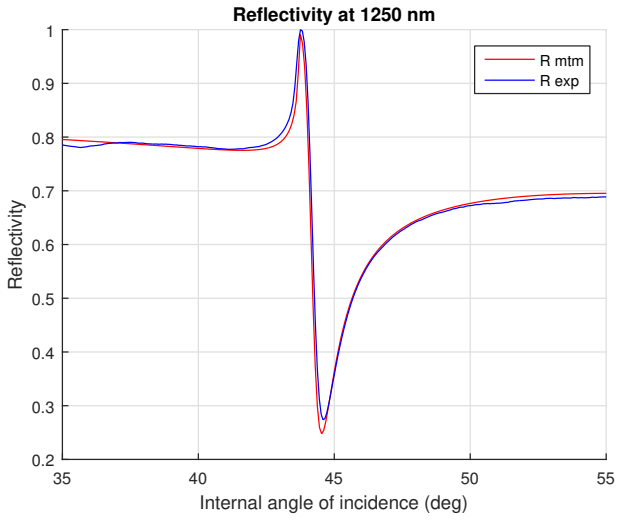

Figure 2.12 – Comparison between the experimental angular dependence of linear reflectivity (blue solid) and the one simulated using MTM (red solid). The structure is (4nm)Au/(10nm)Co/(15nm)Ag.

Simulating the linear reflectivity using MTM

With the MTM described above, the reflectivity $R = |r|^2$ at each angle of incidence can be obtained since k_z depends on the angle. If the refractive index and the thickness of each individual layer are known, the simulated angular dependence of reflectivity should be consistent with the experimental data. Employing the known database for the refractive indices of gold, silver [74] and cobalt [94], one can fit the experimental and MTM-simulated linear reflectivity, as shown in Fig. 2.12. The method helps to estimate the relative thickness between layers and can also be used as a quick check for the quality of the metallic film (see Appendix A). However, this SPP-based approach only works well for the p-polarized light at the infrared wavelength, where the low dispersion of SPP gives a sharp dip in the reflectivity. For shorter wavelengths, the dispersive SPP and lossy metallic layers broaden the angular dip, and the method is no longer reliable.

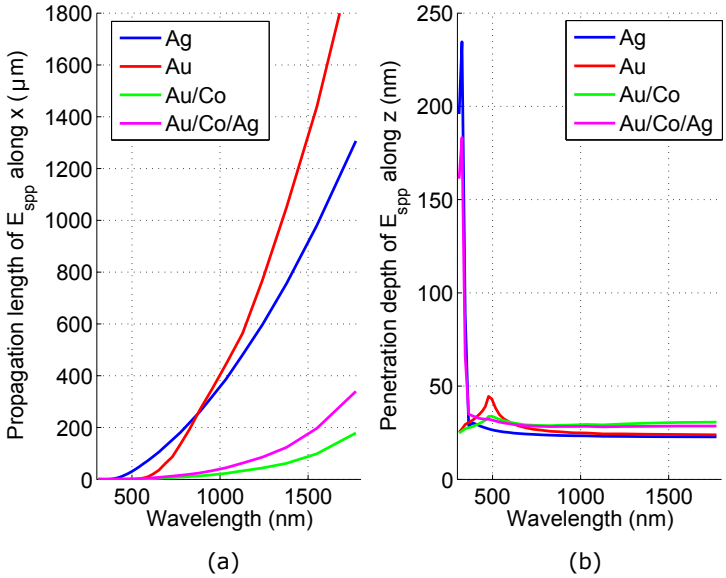

Figure 2.13 – Propagation length and skin depth of the SPP field excited at metal/air surface in different structures: monolayer of Ag (blue), monolayer of Au (green), bilayer of (20 nm)Au/(30 nm)Co, trilayer of (5 nm)Au/(10 nm)Co/(25 nm)Ag.

Effective medium approximation

The effective dielectric function of a metallic multilayer structure can be approximated by an integral of $\epsilon(z)$ within the penetration depth δ_p of an electromagnetic radiation into the metal [7, 12]:

$$\epsilon_{eff} = \frac{1}{\delta_p} \int_0^\infty \epsilon(z) \mathrm{e}^{-z/\delta_p} dz \tag{2.64}$$

Besides MTM, effective medium approximation is a useful tool to predict the optical properties of metallic multilayers. For examples, one can apply Eq. 2.64 to calculate

the effective dielectric function of a (20 nm)Au/ (30 nm)Co bilayer and a (5 nm)Au/ (10 nm)Co/ (25 nm)Ag trilayer (Au on top). Then replace ϵ_m in Eq. 2.57 by ϵ_{eff} to find the wavevector k_{spp} of the SPP field excited at the surface of Au/air. Fig. 2.13 shows the propagation length and skin depth of the SPP fields excited in the hybrid metal/ferromagnet thin films (the bilayer and the trilayer) and compare them with the SPPs excited in the monolayer of Ag and Au. It can be seen that the ferromagnetic layer introduces optical losses to the system and reduces significantly the propagation length of the SPP. However, the skin depth of the SPP field into the metals remains around 24 nm at long wavelengths, not much different from the pure monolayer.

2.4.4 Magneto-plasmonics

Magneto-plasmonics refer to the magneto-optical effects in metallic nanostructures where the coupled mode of surface plasmons and incident light can be activated. Furthermore, in the hybrid metal/ferromagnet thin films, the magnetization in the ferromagnetic layer causes non-zero off-diagonal components of the dielectric function, as we have seen in Table. 2.2. For example, in the transversal MOKE configuration, the effective dielectric tensor has the form

$$\hat{\epsilon}_{eff}(\omega) = \begin{pmatrix} \epsilon_{eff} & 0 & \epsilon^{xz}_{eff} M_y \\ 0 & \epsilon_{eff} & 0 \\ -\epsilon^{xz}_{eff} M_y & 0 & \epsilon_{eff} \end{pmatrix} \tag{2.65}$$

The tensor component ϵ_{xz} leads to a magnetization-induced modulation Δk_{mp} in the wavevector of a SPP excited at metal/air interface [3, 7, 12, 14, 25, 110]

$$\begin{aligned} k_{spp}(\pm M) &= k_{spp,0} \pm \Delta k_{mp} \\ &= k_0 \sqrt{\frac{\epsilon_{eff}}{\epsilon_{eff}+1}} \Big(1 \pm \frac{i\epsilon^{xz}_{eff} M}{1 - \big(\epsilon^2_{eff}\big)\sqrt{\epsilon_{eff}}}\Big) \end{aligned} \tag{2.66}$$

where ϵ^{xz}_{eff} can be well approximated by effective medium approximation in Eq. 2.64 using the known $\epsilon^{xz}(z)$ of the ferromagnetic layer. The non-magnetic SPP wavevector $k_{spp,0}$ is close to that obtained in a single layer of noble metal, except a higher imaginary part $k''_{spp,0}$ representing for the losses. This model has been used to explain the decay of magneto-plasmonic signal as the magnetized layer is buried further from the open surface.

For the nonlinear magneto-plasmonics, the magnetic modulation of nonlinear emission can no longer be described by the magnetization-induced change of wavevector. In these cases, the complexity of the model escalates due to the involvement of different sources of SH emission inside the materials. In the simplest scenario, one must determine a dominant nonlinear susceptibility, i.e. a dominant SH polarization, and then calculate the corresponding SH fields, their interference with the SPP fields and the out-coupled Fresnel coefficients. The theoretical description and the simulation approaches will be present in chapter 3.

Chapter 3

Nonlinear magneto-plasmonics on Kretschmann configuration

While the idea of coupling SPP with the magneto-optical effects have attracted some attentions in recent years[3, 14], the researches related to the nonlinear magneto-plasmonics are scarce due to the complexity of the magnetization-induced second-harmonic emission at the surface and interfaces. While some phenomenological models have been developed [6, 7, 15], the coupling between SPP field and the SH polarizations is still unclear. This chapter is devoted for our experimental findings in this subject. Besides, it is demonstrated in this chapter that the nonlinear SPP coupling in the Kretschmann configuration can be described by classical theories, and the SH magnetic contrast is actually a measure for the SPP coupling efficiency.

3.1 Measurements of Kretschmann magneto-plasmonics

3.1.1 Samples

Following the discussion in section 2.4, in order to sustain the propagating SPP in the visible/infrared spectrum, the metal should have dielectric function with small imaginary part within this spectral range, which is the property of noble metals (gold, silver, copper). SPP mode can carry the information along the film surface with a propagation length up to several hundreds of microns [111], and then it can be coupled out to extract the optical signal. Our goal in this work was to control the propagating SPP by combining it with magneto-optical effect. The propagating SPP field can be tuned by an external magnetic field, but the magneto-optical effect of diamagnetic noble metal is rather small and thus impractical [8–10, 30]. So in order to have large magneto-optical response, ferromagnetic metals (nickel, cobalt, iron) are favorable since the in-plane magnetization of a thin (sub 30 nm) ferromagnetic layer can be switched with small external magnetic field (few millitesla) [7]. To combine the functionalities of magneto-optics and SPP, the simplest structure is a stack of metallic layers.

The simplest form one can think of is the bilayer of ferromagnetic/noble metal with

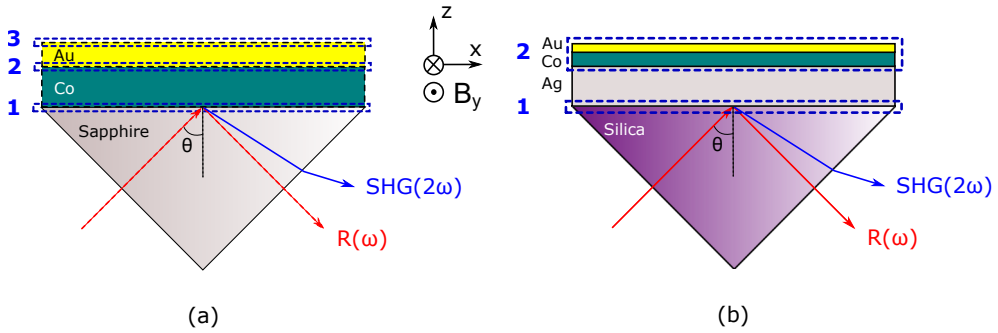

(a) (b)

Figure 3.1 – Kretschmann configuration applied for the metal/ferromagnet multilayers **(a)** Bilayer structure of Au/Co deposited on sapphire. **(b)** Trilayer structure of Au/Co/Ag deposited on fused-silica. The dashed rectangles mark the interfaces where SH emission is considered in the later simulation.

the noble metal exposing to the air, as depicted in Fig. 3.1a. However, the high optical loss of ferromagnetic metal (due to high imaginary part of dielectric function in the visible spectrum) causes the damping of the SPP propagating along Au/air surface, as shown in Fig. 2.13. Though it is not an effective magneto-plasmonic structure in linear regime, the simple bilayer is a good playground for fundamental research in nonlinear regime [32], especially when ultrafast acoustic can be integrated in the same structure. It has been shown in prior research that it is possible to probe the acoustic modulation in thin metallic films by the SPP excited in Kretschmann geometry [112] since the SPP wavevector k_{spp} is highly sensitive to the free-carrier density[1] within its skin depth [113]. The bilayer of gold/cobalt is chosen here because its dynamic properties have been well explored [31], and we can expect to combine acousto-magneto-plasmonics in a single structure.

The studied bilayer samples consist of hexagonal crystal structure Co(0001) and face-centered cubic Au(111) consecutively deposited on a 500 μm double-side epipolished sapphire substrate $Al_2O_3(0001)$[2] (Crystec GmbH) using dc-magnetron sputtering in a high vacuum chamber (base pressure 10^{-7} mbar) at temperature 250℃. Apart from the optical transparency needed for reflectivity measurement in the visible/infrared range, high melting point (2053 ℃) and thermal conductivity (42 W/m·K) of sapphire single crystal are essential in our measurement, where a large fluence of excitation is needed to have detectable nonlinear signals. Varying the thickness of gold layer on top of the 30 nm-thick cobalt, as in Table 3.1, is a way to tune the SPP field. Transversal linear and nonlinear MOKE will be performed on these samples.

In contrast to the bilayer, a trilayer structure, in which the ferromagnetic metal is sandwiched between two noble metals and buried within the SPP field skin depth, has shown superior magneto-plasmonic response in linear regime [3]. Previous systematic researches have identified that for the trilayer Au/Co/Au, cobalt thickness of approximately 6 nm will give optimum SPP-enhanced linear magneto-optical response [25]. Applying these knowledge for nonlinear magneto-plasmonics, we choose to study the

[1] which is proportional to the real part of dielectric function at frequency of probe photons
[2] c-axis is perpendicular to the substrate, with the tilt less than 0.3°

Structure	Thickness of layers
Bilayer	(20 nm)Au/(30 nm)Co/sapphire (30 nm)Au/(30 nm)Co/sapphire (40 nm)Au/(30 nm)Co/sapphire
Trilayer	(5 nm)Au/(10 nm)Co/(15 nm)Ag/fused silica (5 nm)Au/(10 nm)Co/(25 nm)Ag/fused silica (5 nm)Au/(10 nm)Co/(35 nm)Ag/fused silica

Table 3.1 – In this work, the linear magneto-plasmonic measurements were performed on the set of bilayer. The set of trilayer was used for the nonlinear magneto-plasmonic measurements.

structure of Ag/Co/Au trilayers, illustrated in Fig. 3.1b, for the reasons below:
i) the active layer for SPP excitation is silver layer, assuring that the photon energy of SHG (1.6 eV) and THG (2.4 eV) will not exceed the interband transition (4.0 eV) and nonlinear SPP will not be overdamped.
ii) the inplane magnetization of the 5 nm-thick cobalt layer can be switched by a small external magnetic field 20 mT.
iii) the magnetic SHG (mSHG) originated from both sides of cobalt layer, i.e. Ag/Co and Co/Au interfaces, will not destructively interfere, which might happen in Au/Co/Au structure.
Similar to the set of bilayers, varying the thickness of silver layer (Table. 3.1) will modify the efficiency of SPP excitation, and we can define the optimal condition for nonlinear magneto-plasmonic signal. In general, the trilayers have higher SH yield than the bilayers by one-order of magnitude, and thus are a better candidate for practical applications.

3.1.2 Setup

The used setup scheme is shown on Fig. 3.2. A right-angle prism and a detector are mounted on two co-axial motorized rotating stages (Newport PR50PP), in which the rotation angles of the two devices are θ and 2θ, respectively. The illuminated spot on the thin film is aligned to the rotation axis of motorized stages. The alignment is performed at angle of incidence 45° at the hypotenuse side of the prism, where the studied sample is installed. The incident beam is thus perpendicular to the square sides of the prism. This is the "reference angle", preset as zero angle of rotation. The prism can be rotated in the range of -30° to +25° around zero angle. The rotation angle of detector is twice as much as that of the prism. The rotation angle of prism is then recalculated into angle of incidence inside sample substrate applying Snell law[3]. After conversion, the maximum range of incident angle in the air is 20-75°, minimum angular increment 0.05°, unidirectional repeatability 0.05°. The overall goniometric motorized platform is compact, enabling multi-parameter measurements and can be

[3] $n_1 \sin\theta_1 = n_2 \sin\theta_2$, where n_1, n_2 are refractive indices of two transparent media 1 and 2. θ_1, θ_2 are the angles of the light beam in these media to the surface normal.

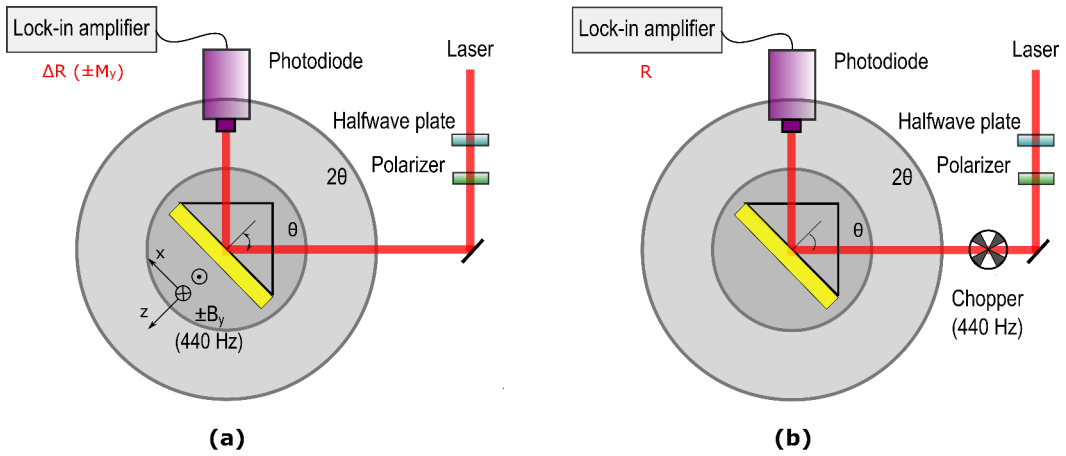

Figure 3.2 – Scheme of a linear magneto-plasmonic setup employing Kretschmann configuration. (a) Measurement of magnetization-induced variations in reflectivity $\Delta R(\pm M)$. (b) Measurement of the average reflectivity R. The ratio $\Delta R/R$ implies the normalized transversal MOKE signal.

used for various configurations, such as linear and nonlinear magneto-plasmonics in either Kretschmann geometry or diffraction grating.

Linear magneto-plasmonic measurements

For linear magneto-plasmonic measurements, an external magnetic field is applied. It is generated by an electromagnet, field switching frequency 440 Hz (resonance frequency of the registered LC circuit). A piece is cut from the ferrite ring magnet in order to have straight magnetic field lines between two ends. The prism is held free-standing between the two poles in such a way that the magnetic field is perpendicular to the plane of incidence (see B_y in Fig. 3.2a).

The (TM) p-polarized collimated beam is used to ensure that each angle of incidence corresponds to only one k_x and thus one k_{spp}, i.e. k-space measurement. A silicon photodiode is used for visible spectral range (400-1070 nm) and a germanium photodiode is used for the near-infrared spectrum (800-1700 nm). In the transversal MOKE configuration discussed in section 2.2.3, reversal of the external magnetic field results in the modulation of reflectivity $\Delta R/R$, so-called MOKE signal. Using the lock-in amplifier SR830, the tiny magnetization-induced change $\Delta R = R(+M) - R(-M)$ is measured through a reflectivity locked-in at the switching frequency of the magnetic field 440 Hz (see Fig. 3.2a). The signal is normalized to R, which is the reflectivity measured when the magnet is removed and the incident light is chopped at 440 Hz, as shown in Fig. 3.2b.

Nonlinear magneto-plasmonic measurements

In the nonlinear magneto-plasmonic setup, high magnetic field switching frequency is not necessary because of the long integration time of the photon counter and strong magnetic nonlinear signal. The external magnetic field is generated by Neodymium

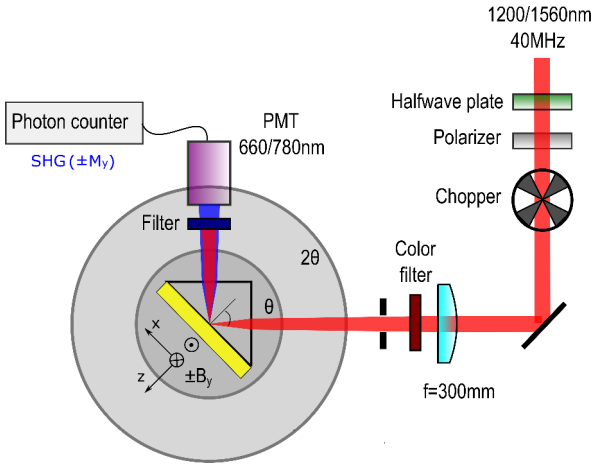

Figure 3.3 – Top-view of a SH nonlinear magneto-plasmonic setup based on Kretschmann geometry.

permanent magnets with field strength of ≈150 mT at the distance of 5 mm from the pole (see Fig. 3.4). The change of magnet poles is performed with a linear motorized level (Newport). Distance between the two magnets on the level is 34 mm, ensuring no stray magnetic field between two poles at the distance of 5 mm underneath the magnets. Sample holders are made of non-magnetic materials, like aluminium or teflon.

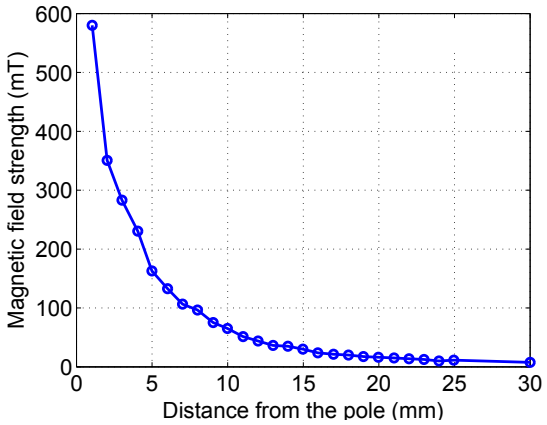

Figure 3.4 – The dependence of magnetic field strength on the distance from a pole of a Neodymium permanent magnet cube (each side 1.5 mm).

In nonlinear measurements (see Fig. 3.3), the p-polarized (TM) fundamental radiation is focused to the thin film by an uncoated plano-convex lens (Thorlabs) with the focal length f=300 mm. Focusing angle, calculated for the incident 3.5 mm-diameter collimated beam at wavelength 1560 nm, is 0.67° in the air, which becomes 0.45° inside glass prism and 0.35° inside sapphire substrate. This angle is less than the angular width[4] 0.8° of ATIR dip of trilayer structure. Focusing the incident light will increase

[4]full-width half maximum FWHM

the number of incident wave vectors, causing angular broadening. However, it is necessary to have a high excitation fluence in a small area for the generation of nonlinear signal. The choice of the focal length is thus a compromise between effective coupling to SPP modes and SH output.

A color filter is placed after the lens to filter possible radiations from the optical components, thus ensures pure fundamental radiation. Generated on the metallic thin films, the SH output is then spectrally separated by a color BG-39 filter (Schott) and recorded with a photomultiplier tube (PMT). The power dependence of the detected signal in Fig. 3.5 shows a quadratic behavior $I(2\omega) \propto I^2(\omega)$, assuring that the signal coming through the low-pass filters is second-harmonic generation.

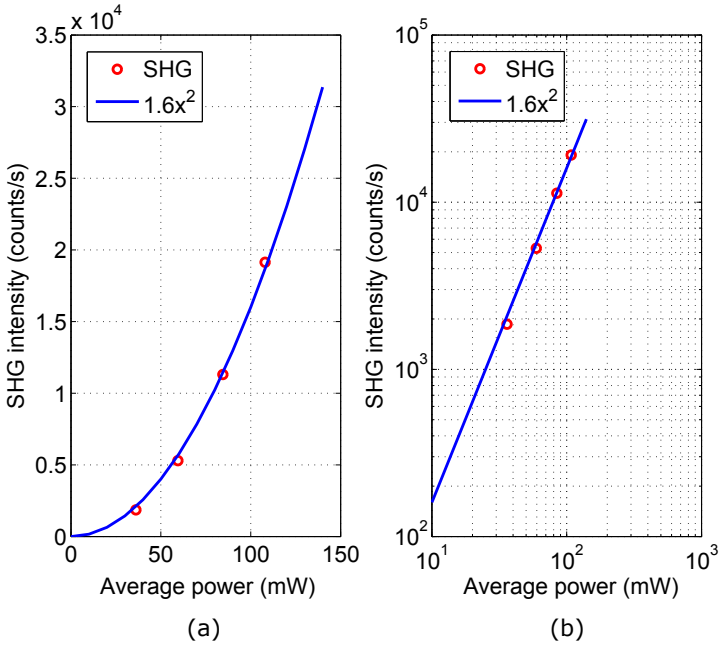

Figure 3.5 – The fluence dependence of the signal detected by the PMT. The quadratic behavior shown in (a) and the linear dependency in the logarithm plot (b) ensures that the detected signal is a second-harmonic generation.

To detect the optical nonlinear signals, the PMT (Hamamatsu R955) is utilized along with a two-channel gated photon counter (SR400). Generated at cathode based on photoelectric effect, the photocurrent is amplified in 9 dynodes of the PMT before reaching anode, with a typical gain of 10^7 at voltage 1000 V. The multialkali photocathode of the PMT allows wide spectral response 160-900 nm, with quantum efficiency of 3% and cathode radiance sensitivity 20 mA/W for wavelength 780 nm. At very low level of illumination, each photoelectron generated at PMT cathode is represented in the oscilloscope as an electric pulse with typical rise time 2.2 ns and transit time 22 ns. The pulse rate is proportional to the number of incident photons per second. To separate the dark current (typically 150 counts/s at supply voltage 900 V), the photon counter is set at gated regime, i.e. one channel counts the overall signal while the other channel concerns only the dark counts. It is performed by chopping

the excitation light, then use the chopping frequency as the trigger for the counting gates. High chopping frequency helps to reduce the heat accumulation in sample. The counting scheme is illustrated in Fig. 3.6. For the chopping frequency of 1.7 kHz, the trigger period is ≈590 μs. The temporal width of both counting gates is 230 μs (≈ 40% of trigger period), much larger than the PMT transition time. The signal is the difference of count rate between gate A and gate B. Integration time for each data point is 0.46 s. The detection of weak signals, like angular dependence of nonlinear magnetic contrast, usually requires high statistics. This detection scheme is limited by shot noise, which relates to the particle nature of photons, and thermal noise, which is the cause of dark counts.

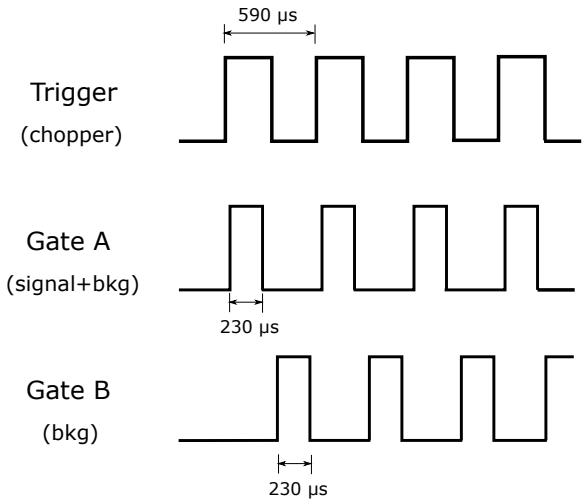

Figure 3.6 – An example of the counting scheme. The trigger frequency is set by the chopper. Gate A counts both the signal and the background (bkg) at the open phase of the chopper. Gate B counts the background when the chopper is close.

3.1.3 Light source

The choice of the light source is based on the dispersion relation of SPP (Fig. 2.9). In Kretschmann configuration, the light line is tilted by a factor of $n \sin\theta$ and thus allows the variation of incident wave vector within a grey cone for $\theta = 0 - 90\,\mathrm{deg}$. As it is clearly depicted in the dispersion relation, at a certain frequency ω only one angle can excite the corresponding SPP, represented as a sharp dip in the angular dependence of reflectivity. But in fact, there is always an angular broadening, due to the optical loss of SPP. The damping of SPP is particularly high when there is spectral overlap with interband transition (see Fig. 2.13).

The telecommunication wavelengths 1.3 μm (0.95 eV) and 1.56 μm (0.8 eV) are employed, which give SHG at the wavelengths 650 nm (1.9 eV) and 780 nm (1.55 eV), respectively. Both the fundamental and SH photon energies are far below the interband transition thresholds of noble metals (Table. 2.1). Due to the low dispersion, the SPPs excited at the infrared spectral range give sharp features in the angular spectrum. Furthermore, as shown in the dispersion relation in Fig. 2.9, the light line inside the

prism (substrate) at the fundamental frequency nk_0 (green dashed line) is very close to the SPP wavevector k_{spp} (red solid line) at small photon energy (< 2 eV), which means that without significant dispersion, a fundamental radiation having photon energy $\hbar\omega < 1$ eV can excite both the fundamental SPP with wavevector $k_{spp}(\omega)$ and the second-harmonic SPP with wavevector $k_{spp}(2\omega) \simeq 2k_{spp}(\omega)$. The wavelength 1.55 μm (0.8 eV) even allows us to inspect the nonlinear magneto-plasmonics at the third-harmonic generation (THG) at the wavelength 520 nm (see Appendix B), though the THG would be much more dispersive than the SHG.

A femtosecond Erbium-doped fiber laser (Toptica FemtoFiber pro NIR) installed at IMMM is used as the light source. The laser has two outputs, fundamental wavelength at 1560 nm and second-harmonic wavelength (generated by an integrated piece of periodically poled lithium niobate PPLN) at 780 nm. The pulse duration of both outputs is sub-120 fs, repetition rate 40 MHz.

Some nonlinear magneto-plasmonic measurements were performed at Department of Physics (University of Konstanz). There, the light source is a fiber laser operated at center wavelength 1200 nm with bandwidth of ≈400 nm. The pulse duration is sub-10 fs, and repetition rate 40 MHz.

3.2 Results

In this section, the priliminary results of the Au/Co bilayer and the Au/Co/Ag trilayer are shown to give a general look on the properties of magneto-plasmonics in multilayer structures. The experimental data will be discussed in more details and fitted with the numerical simulations in the next sections.

3.2.1 Bilayer structure of Au/Co

In the prior research [6, 7, 30], the magneto-plasmonics becomes effective in the metallic multilayer structures when the ferromagnetic layer is buried within the intensity penetration depth 12 nm from the open surface. However, in this work, I have shown that as long as the ferromagnetic layer is within the field skin depth, i.e. 24 nm from the open surface, reasonable magneto-plasmonics behaviors appear in both the linear and the nonlinear regimes.

Linear MOKE in the bilayers

Cobalt, with its high imaginary part of dielectric function ϵ'' in the visible spectrum, is the cause for optical loss in multilayer structures. It results in the significant reduction of the SPP propagation length along the surface of Au/air, as shown in Fig. 2.13 in the previous chapter. The bilayer Au/Co thus has been considered as an ineffective magneto-plasmonic structure, and people in the field prefer to work with the trilayer Au/Co/Au or Au/Co/Ag, where the SPP-induced MOKE is more pronounced. Despite the loss, I have observed the SPP-induced transversal MOKE on the bilayer of (20-30-40 nm)Au/(30 nm)Co at the wavelength 633 nm using HeNe laser source, shown in Fig. 3.7.

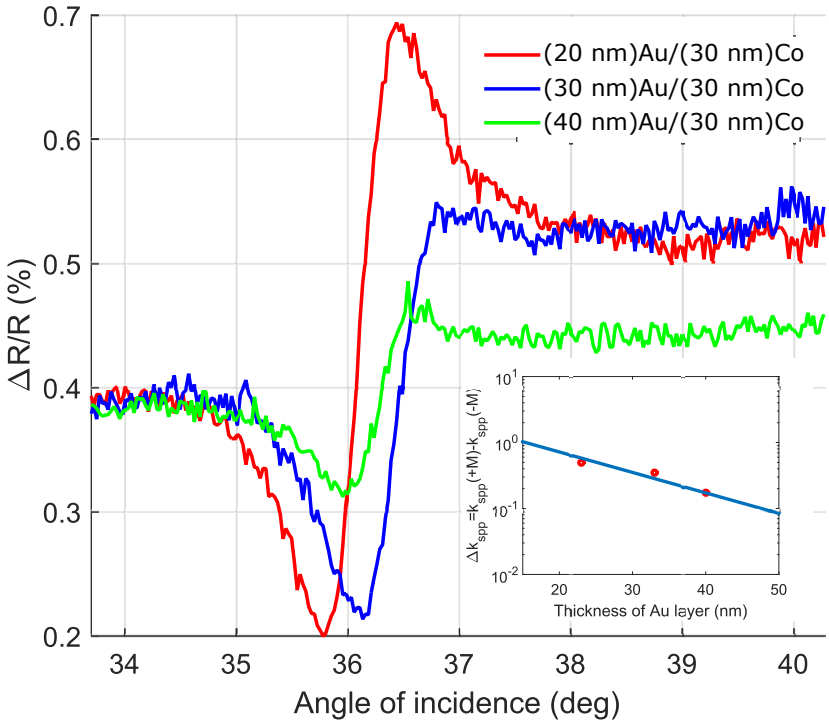

Figure 3.7 – Angular dependence of linear transversal MOKE measured on the bilayer (20-30-40 nm)Au/(30 nm)Co at the wavelength 633 nm.

As discussed in the section 2.4.4, the angular variation of MOKE signal represents for the magnetic modulation of the SPP wavevector, specifically $\Delta k_{spp} = k_{spp}(+M) - k_{spp}(-M)$, which originates from the variation of off-diagonal components $\epsilon^{xz}_{eff} M_y$ in the dielectric function of bilayer. The maximal variation of the MOKE response follows the decay of Δk_{spp} when the top Au layer is thicker, i.e. when the distance from cobalt layer to the open surface increases, shown in the inset of Fig. 3.7. This observation confirms the undeniable effect of SPP on the magneto-optics in bilayer.

Nonlinear magneto-plasmonics in the bilayer

Nonlinear Kretschmann ATR measurement on sample (20 nm)Au/ (30 nm)Co/ sapphire, in general, gives low SH output with the peak at only few hundreds counts/s. However, the effects of linear and nonlinear SPP modes shown on the k-spectrum of the SH intensity and the nonlinear magnetic contrast in the bilayer are very clear because the active interfaces (air/Au, Au/Co and Co/sapphire as shown in Fig. 3.1a) are well separated. Fig. 3.8 shows the angular dependence of the SH intensities (green and black solid lines) at opposite magnetizations and the corresponding magnetic contrast (magenta solid line). The linear reflectivity at the fundamental wavelength 1560 nm (red dashed line) and at the half-wavelength 780 nm (blue dashed line) mark the angles where the SPP at these wavelengths can be excited. In Fig. 3.8a, the SH intensity (green solid line) has a peak at 35.4° and a dip at 36.1°, which are in accordance with the angular minima of linear reflectivity at 1560 nm and 780 nm, where the SPP(ω)

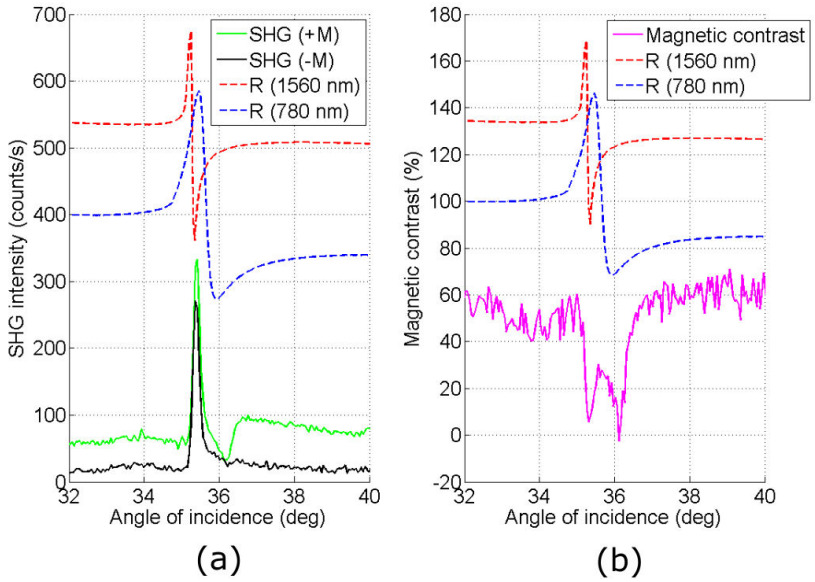

Figure 3.8 – (a) Angular dependence of SH output from the bilayer of (20 nm)Au/ (30 nm)Co measured at two different magnetizations (green and black solid lines). (b) The angular dependence of the SHG magnetic contrast (magenta solid line). The linear reflectivity (arbitrary unit) at fundamental (1560 nm) and SHG (780 nm) wavelengths are shown in (a) and (b) as dashed lines in order to mark the angles of incidence where SPP(ω) and SPP(2ω) are excited in the linear configuration.

and SPP(2ω) are supposed to be excited.

Similarly, the SH magnetic contrast in Fig. 3.8b has a double-dip feature, in which each dip occurs near the angular minimum of a linear reflectivity. Contradict to the linear magnetic contrast of <1%, the second-harmonic magnetic contrast can reach as high as 60%. If the angular dependence of linear contrast $\Delta R/R$ shows just one oscillator, the nonlinear magnetic contrast exhibits two modes resonant at different angles.

3.2.2 Trilayer structure of Au/Co/Ag

The peak of SH intensity in the case of trilayer can reach few thousands counts/s, an order-of-magnitude higher than that in the bilayer. Similar to the linear regime [3, 14], the nonlinear magneto-optical signals in metallic multilayers can be enhanced or damped by SPP field. To demonstrate that possibility, one can vary the thickness of Ag layer in the trilayer structures (5 nm)Au/ (10 nm)Co/ (15-25-35 nm)Ag. The linear reflectivity, SH intensity and nonlinear magnetic contrast of these three samples are shown in Fig. 3.9. Thinner silver layer supports stronger SPP modes, resulting in deeper reflectivity minima in Fig. 3.9a and stronger SHG output in Fig. 3.9b occurring at the same angle. The peak SH intensity at angle 44.5° represents for the second-harmonic signal generated at the surface Au/air. Its intensity thus follows the attenuation of an electromagnetic field at 780 nm in silver, plotted as the inset of

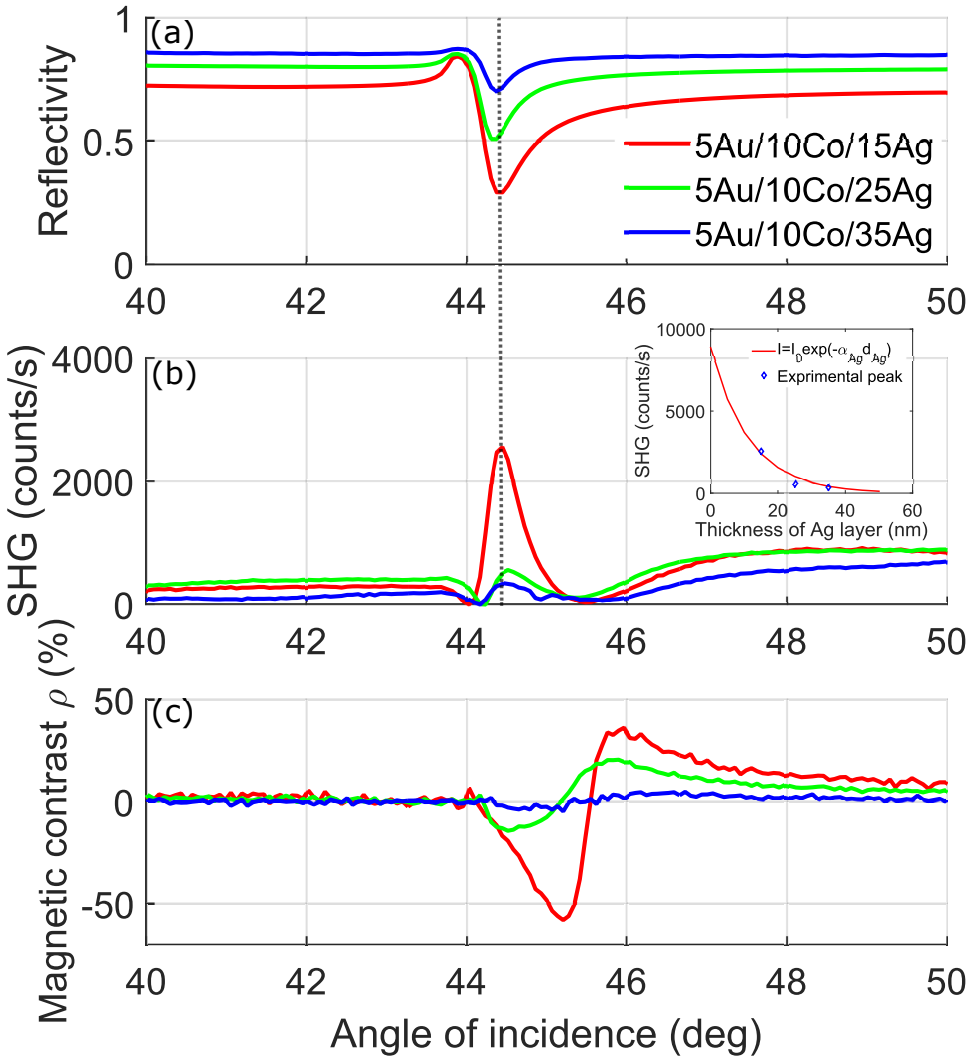

Figure 3.9 – Angular dependence of **(a)** linear reflectivity at 1560 nm, **(b)** SHG intensity at 780 nm and **(c)** transversal nonlinear magnetic contrast ρ in trilayer (5 nm)Au/(10 nm)Co/(15-25-35 nm)Ag. The SHG peak at 44.5 deg corresponds to the linear SPP(ω) mode, confirmed by the dip of linear reflectivity at the same angle.

Fig. 3.9b.

The magnetic contrast ρ in Fig. 3.9c also shows increasing value for samples with thinner layer. For the sample (5 nm)Au/ (10 nm)Co/ (15 nm)Ag, the SH contrast (red solid curve) varies from around -60% at angle 45.2° to 40% at angle 46°, higher than the reported data for a nonlinear magneto-plasmonic signal in a trilayer [6]. From the technical perspective, it means that the SH intensity can be amplified four times by a weak external magnetic field of a permanent magnet.

3.3 Theoretical description

As we have discussed in the section 2.3, the sources of SHG in metallic multilayer structures are limited to the surface and interfaces, according to the electric dipole approximation. The nonlinear polarizations at metal/dielectric interfaces have been described in Eq. 2.46

$$P_i(2\omega) = \epsilon_0 \chi_{ijk} E_j(\omega) E_k(\omega)$$

where χ_{ijk} is the second-order susceptibility tensor, and i, j, k denote Cartesian coordinates. These polarizations are sources of light at the double frequency (2ω), which radiate towards both the dielectric substrate and the air (see A_0 in Fig. 3.10). In Kretschmann configuration, the field of SPP(2ω) can be coupled when the SHG phase-matching condition $2k_x = k_{spp}(2\omega)$ is fulfilled, resulting in a nonlinear leaky (radiative) mode detectable at the far-field, A_{spp} in Fig. 3.10.

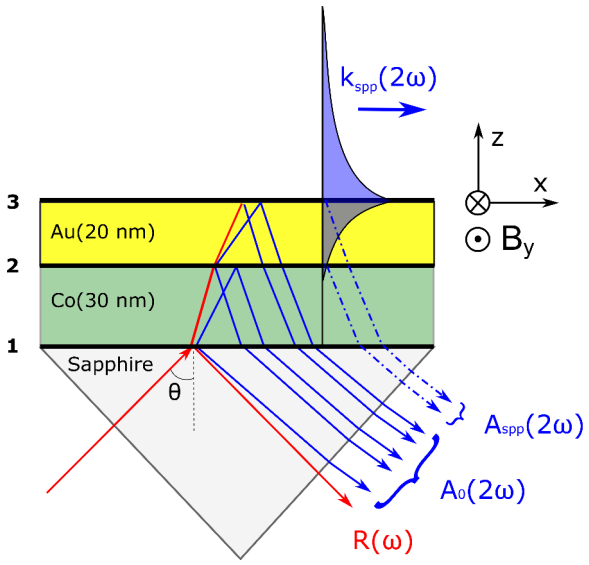

Figure 3.10 – Illustration of nonlinear excitation of SPP by SHG in bilayer (20 nm)Au/ (30 nm)Co employing Kretschmann configuration. External magnetic field is applied perpendicular to the plane of incidence. Incident field (red) generates nonlinear sheet polarizations and excite SPP(ω) at Au/air surface. Nonlinear polarization at each interface acts as radiative source of SHG (blue). $A_{spp}(2\omega)$ stands for the radiative SPP at 2ω, while $A_0(2\omega)$ denotes the non-resonant SHGs.

Within our concern, the fundamental excitation is p-polarized with the electric field components $E_x(\omega)$ and $E_z(\omega)$. The external magnetic field is perpendicular to the plane of incidence B_y, as in the tranversal MOKE configuration. Referring to section 2.3.2, six non-zero second-harmonic susceptibilities are valid in this case, and three among them are dependent on the magnetization, as listed in Table. 3.2. The resulting SH polarizations are either $P_x(2\omega)$ or $P_z(2\omega)$, i.e. p-polarized SHG.

Non-magnetic (even) $\chi^{(2)}$	**Magnetic (odd)** $\chi^{(2)}$
χ_{zzz}	χ_{xzz}
χ_{zxx}	χ_{xxx}
χ_{xzx}	χ_{zzx}

Table 3.2 – The non-zero second-order nonlinear susceptibility components for p-polarized fundamental radiation.

Now, the model of nonlinear surface plasmon polariton (SPP) excited in Kretschmann geometry will be introduced in the following. This section includes two parts: (i) the radiation of nonlinear SPP at 2ω excited in Kretschmann configuration, and (ii) the derivation of SHG magnetic contrast under the excitation of nonlinear SPP(2ω).

3.3.1 Radiative nonlinear surface plasmon polaritons

The amplitude $A_{spp,n}$ of the nonlinear SPP field $\overrightarrow{E_{spp}}(2\omega)$ launched by the nonlinear sheet polarization $\overrightarrow{P}(2\omega)$ at a certain interface n is the scalar (dot) product of those two:

$$\begin{aligned} A_{spp,n} &= \overrightarrow{P}(2\omega) \cdot \overrightarrow{E_{spp}}(2\omega) \\ &= P_x(2\omega)E_{spp,x}(2\omega) + P_z(2\omega)E_{spp,z}(2\omega) \end{aligned} \tag{3.1}$$

The total amplitude, as a result of the interference of scattered and reflected fields with amplitudes A_n, can be written:

$$A_{spp} \propto \iint P(2\omega)E^*_{spp}(2\omega)dzdx \tag{3.2}$$

In this equation, the second-order nonlinear polarization $P(2\omega)$ represents the sum of sources localized at N individual interfaces, each is located at $z = z_n$ ($z = 0$ at the open surface) and can be thus written

$$P(2\omega) \propto \sum_{n=1}^{N} P_n \delta(z - z_n) \exp[2ik_x(\omega)x - 2i\omega t]$$

This nonlinear polarization propagates along the surface with the phase velocity determined by $2k_x(\omega) = 2k_0(\omega)n(\omega)\sin\theta$, where $k_0(\omega)$ is vacuum wavevector, $n(\omega)$ is the refractive index of the dielectric substrate at the fundamental frequency, and θ denotes the angle of incidence.

The electric field of the co-propagating SPP(2ω), which decays along the normal (z) direction and propagates along the in-plane x direction, is written as

$$E_{spp}(2\omega) \propto \exp[-\frac{z}{\delta_{skin}} + ik_{spp}(2\omega)x - 2i\omega t]$$

where δ_{skin} is the field skin depth ($\approx$ 24 nm[5] in metals). As a consequence, Eq. 3.2 becomes:

$$\begin{aligned} A_{spp} &\propto \iint P(2\omega)E^*_{spp}(2\omega)dzdx = \\ &\propto \int \sum_{n=1}^{N} P_n \delta(z - z_n) \mathrm{e}^{-\frac{z}{\delta_{skin}}} dz \times \int \mathrm{e}^{-i[k_{spp}(2\omega) - 2k_x(\omega)]x} dx \\ &= \left(i \sum_{n=1}^{N} P_n \mathrm{e}^{-\frac{z_n}{\delta_{skin}}} \right) \frac{1}{k_{spp}(2\omega) - 2k_x(\omega)} \end{aligned} \tag{3.3}$$

$k_x(\omega)$ is real, but $k_{spp}(2\omega)$ is complex and can be written as $k_{spp} = k'_{spp} + ik''_{spp}$, where k'_{spp} and k''_{spp} denote the real and imaginary parts of the SPP wavevector. The second factor in Eq. 3.3 is then:

$$\frac{1}{k_{spp}(2\omega) - 2k_x(\omega)} = \frac{1}{[k'_{spp}(2\omega) - 2k_x(\omega)] + ik''_{spp}(2\omega)} \tag{3.4}$$

which has a shape of a Lorentzian complex function, coherent with the SPP theory. To work with a normalized and dimensionless function, Eq. 3.5 is multiplied by k''_{spp}:

$$L(k_x) = \frac{k''_{spp}(2\omega)}{[k'_{spp}(2\omega) - 2k_x] + ik''_{spp}(2\omega)} \tag{3.5}$$

This equation reaches the maximum when $k'_{spp}(2\omega) - 2k_x(\omega) = 0$, and thus one gets

$$k'_{spp}(2\omega) = 2k_0(\omega)n(\omega)\sin\theta \tag{3.6}$$

Eq. 3.6 describes the nonlinear phase-matching condition for the second-harmonic SPP(2ω). Linearizing $\sin\theta$ at the vicinity of the resonant angle θ_0 [6], Eq. 3.6 becomes:

$$\theta - \theta_0 = \frac{k'_{spp}(2\omega)}{2k_0(\omega)n(\omega)\cos\theta_0} - \tan\theta_0 \tag{3.7}$$

The complex Lorentzian function $L(k_x)$ can be then written in term of angle of incidence θ by dividing both the numerator and the denominator of Eq. 3.5 by $2k_0(\omega)n(\omega)\cos\theta_0$:

$$L(\theta) = \frac{\Gamma}{(\theta - \theta_0) + i\Gamma} \tag{3.8}$$

[5]The intensity penetration depth is $\frac{\delta_{skin}}{2}$=12 nm

[6]The linearization of $\sin(\theta)$ at angle θ_0 is: $\sin\theta_0 + \cos\theta_0 \times (\theta - \theta_0)$

in which the angular width is described by $\Gamma = \dfrac{k''_{spp}(2\omega)}{2k_0(\omega)n(\omega)\cos\theta_0}$ and $\big|L(\theta_0)\big| = 1$. The Lorentzian shape is kept consistent with the theory. As such, the resonant angle θ_0 represents the excitation condition of the nonlinear SPP(2ω), and the angular width Γ corresponds to the optical loss of the field via $k''_{spp}(2\omega)$.

The final form of the second-harmonic SPP field amplitude A_{spp} in Eq. 3.3 reads:

$$A_{spp}(\theta) \propto \left[i \sum_{n=1}^{N} P_n(\theta) \exp\big(- z_n/2\delta_{skin} \big) \right] L(\theta) \tag{3.9}$$

The approximation in Eq. 3.9 will be employed in our simulations of magnetic SHG generated in multilayer structures in the later section. Note that $\exp\big(- z_n/2\delta_{skin} \big)$ is a constant factor for each interface n, which is positioned at the depth z_n from the open surface.

To complete the story, the SHG observed at the far-field is the interference of non-resonant second-harmonic fields (denoted as $A_0 = P_0$) and the leaky nonlinear SPP field A_{spp} evoked by the polarizations located near metal/air surface, as summarized in Fig. 3.10. The detected SHG intensity is thus:

$$I_{2\omega} = |A_0 + A_{spp}|^2 \tag{3.10}$$

3.3.2 Calculate SHG magnetic contrast (abcd-model)

Based on the coupling with surface plasmons at the double-frequency 2ω, represented by the function $L(\theta)$ described in Eq. 3.8, one can distinguish the sources of SHG into the SPP non-resonant sources ($A_0 \propto E_{non-res}$) and the SPP resonant ones ($A_{spp} \propto LE_{res}$). The total SHG intensity is thus:

$$I_{2\omega} = |E_{non-res} + LE_{res}|^2 \tag{3.11}$$

where each of these components includes magnetic and non-magnetic parts:

$$\begin{aligned} E_{non-res} &= \tilde{a} + \tilde{b}m \\ E_{res} &= \tilde{c} + \tilde{d}m \end{aligned} \tag{3.12}$$

Here m denotes the in-plane magnetization. $\tilde{a}$ and $\tilde{c}$ are magnetization-independent, while the magnetic components $\tilde{b}$ and $\tilde{d}$ are considered to be very small. The total SHG intensity is:

$$I_{2\omega} = |(\tilde{a} + \tilde{b}m) + \tilde{L}(\tilde{c} + \tilde{d}m)|^2 \tag{3.13}$$

Note that the average SHG is the intensity at $m = 0$, which is:

$$I_{2\omega}(m = 0) = |\tilde{a} + \tilde{L}\tilde{c}|^2 \tag{3.14}$$

$\tilde{a}$, $\tilde{b}$, $\tilde{c}$, $\tilde{d}$ and $\tilde{L}$ are, in general, complex. For simplification, the tilde is removed from here on; for example, the complex component $\tilde{a}$ is denoted as a, and its complex

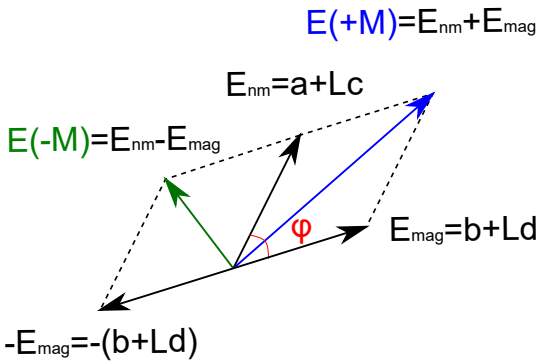

Figure 3.11 – The phasor diagram of non-magnetic and magnetic SHG fields, respectively E_{nm} and E_{mag}, taking account the non-resonant (a, b) resonant (c, d) SH components. Zero magnetic contrast, i.e. $E(+M) = E(-M)$, happens when the phase difference is $\varphi = \frac{\pi}{2}$

conjugation is a^*. The intensity $I_{2\omega}$ is fully expanded into:

$$\begin{aligned} I_{2\omega} &= [a + bm + L(c + dm)][a^* + b^*m + L^*(c^* + d^*m)] \\ &= |a|^2 + a^*bm + ab^*m + |b|^2m^2 + L(a^*c + a^*dm + cb^*m + db^*m^2) \\ &+ L^*(ac^* + c^*bm + ad^*m + bd^*m^2) + |L|^2(|c|^2 + c^*dm + cd^*m + |d|^2m^2) \end{aligned} \tag{3.15}$$

According to this, the change of SHG intensity depending on magnetization, assuming that m is very small, is:

$$\begin{aligned} \frac{\partial I_{2\omega}}{\partial m} &= a^*b + ab^* + 2|b|^2m + L(a^*d + cb^* + 2db^*m) \\ &+ L^*(c^*b + ad^* + 2bd^*m) + |L|^2(c^*d + cd^* + 2|d|^2m) \end{aligned} \tag{3.16}$$

The difference in SHG intensity upon the reversal of magnetization is approximately its derivative at $m = 0$, giving:

$$\begin{aligned} \Delta I_{2\omega}(\pm m) &= \frac{\partial I_{2\omega}}{\partial m}(m = 0) \\ &= a^*b + ab^* + L(a^*d + cb^*) + L^*(c^*b + ad^*) + |L|^2(c^*d + cd^*) \\ &= 2\Re\{(a^* + L^*c^*)(b + Ld)\} \\ &= 2\Re\{|a + Lc|e^{-i\varphi}|b + Ld|\} \end{aligned} \tag{3.17}$$

where φ is the phase difference between the non-magnetic $(a + Lc)$ and the magnetic $(b + Ld)$ components, as illustrated in Fig. 3.11, the phasor diagram of the SH fields.

Formulated in Eq. 2.50 in the previous chapter, the magnetic contrast ρ is usually used as a technical measure for the nonlinear magneto-optical effect. Here ρ can be written as

$$\rho = \frac{\Delta I_{2\omega}}{I_{2\omega}(m=0)} = \frac{2\Re\{|a+Lc|e^{-i\varphi}|b+Ld|\}}{|a+Lc|^2} = \frac{2\Re\{|b+Ld|e^{-i\varphi}\}}{|a+Lc|} \tag{3.18}$$

Noting that the magnetic components b and d are small, and L can be represented in term of angle of incidence $L(\theta)$, the angular dependence of the SH magnetic contrast $\rho(\theta)$ should imitate the shape of $\Re L(\theta)$.

Eq. 3.18 includes both the non-magnetic $|a+Lc|$ and the magnetic $|b+Ld|$ field components in the magnetic contrast. One can annihilate the non-magnetic parts in eq. 3.17 dividing the $\Delta I_{2\omega}$ by $\sqrt{I_{2\omega}(m=0)}$:

$$\phi = \frac{\Delta I_{2\omega}}{\sqrt{I_{2\omega}(m=0)}} = 2\Re\{|b+Ld|e^{-i\varphi}\} \tag{3.19}$$

This newly-defined magnetic contrast ϕ in Eq. 3.19 has simpler form than the conventional contrast ρ in Eq. 3.18, but it is not yet normalized. Thus, to quantify and to compare the nonlinear magneto-optical effects, it is still more convenient to use the original magnetic contrast ρ. The new contrast ϕ is adopted particularly in this chapter just to illustrate the influence of the nonlinear SPP excitation $L(\theta)$ on the SH magneto-optical signals, which is otherwise hidden by the non-magnetic component $|a+Lc|$ in the description of ρ. Throughout the text, both contrasts will be shown and compared.

In a structure where the plasmonic-active layer is thick; for example, the trilayer of (5 nm)Au/(10 nm)Co/(35 nm)Ag, the magnetic component of the non-resonant SHG, observed at low angle of incidence, is almost zero as shown in blue curve in the Fig. 3.9c, meaning $b \approx 0$. The SH magnetic contrasts in this case can be written as:

$$\begin{aligned} \rho &= \frac{\Delta I_{2\omega}}{I_{2\omega}(m=0)} = \frac{2\Re\{Lde^{-i\varphi}\}}{|a+Lc|} \\ \phi &= \frac{\Delta I_{2\omega}}{\sqrt{I_{2\omega}(m=0)}} = 2\Re\{Lde^{-i\varphi}\} \end{aligned} \tag{3.20}$$

The magnetic contrast ϕ now becomes a direct measure for the nonlinear SPP influence $L(\theta)$ in the magneto-plasmonic structures.

3.4 Simulation methods

This section shows how one can predict the SPP coupling efficiency L(θ). Two approaches will be presented (i) the forward approach, where one calculates the nonlinear L(θ) and magnetization-induced SHG using effective medium approximation and numerical tools, and (ii) the reverse approach, where the SPP coupling efficiency is directly obtained from the experimental magnetic contrast.

3.4.1 Forward approach

In order to attain the nonlinear SPP coupling efficiency $L(\theta)$ (Eq. 3.5) and the resonant second-harmonic field amplitude A_{spp} (Eq. 3.3), first we need to derive the SPP wavevector k_{spp}. It is thus necessary to know the effective dielectric functions of the plasmonic multilayer structure. This was done using Effective Medium Approximation [12], knowing that the SPP penetration depth δ_p at wavelength 1.56 μm is about 12 nm. By using Eq. 2.64, one can estimate the effective dielectric function ϵ_{eff} of a metallic multilayer structure. Then ϵ_{eff} can be used to calculate the SPP wavevector k_{spp}, based on Eq. 2.57

$$\begin{aligned} k_{spp}(x) &= k_0\sqrt{\frac{\epsilon_{eff}}{1+\epsilon_{eff}}} \\ k_{spp}(z) &= \sqrt{\epsilon_{eff}k_0^2 - k_{spp}^2(x)} = k_0\frac{\epsilon_{eff}}{\sqrt{1+\epsilon_{eff}}} \end{aligned} \tag{3.21}$$

With the complex $k_{spp}(x) = k'_{spp} + ik''_{spp}$, one can readily calculate the coupling efficiency of SPP in the linear regime:

$$\begin{aligned} L_{lin}(\omega) &= \frac{k''_{spp}(\omega)}{[k'_{spp}(\omega) - k_0(\omega)n(\omega)\sin\theta] + ik''_{spp}(\omega)} \\ L_{lin}(2\omega) &= \frac{k''_{spp}(2\omega)}{[k'_{spp}(2\omega) - k_0(2\omega)n(2\omega)\sin\theta] + ik''_{spp}(2\omega)} \end{aligned} \tag{3.22}$$

and in nonlinear regime, as in Eq. 3.5

$$L_{nl}(2\omega) = \frac{k''_{spp}(2\omega)}{[k'_{spp}(2\omega) - 2k_0(\omega)n(\omega)\sin\theta] + ik''_{spp}(2\omega)}$$

Note that the nonlinear Lorentzian function ($L_{nl}(2\omega)$) is different from the linear Lorentzian function at the frequency 2ω ($L_{lin}(2\omega)$) because of dispersion. Within the optical range, the refractive index of the substrate $n(2\omega)$ in $L_{lin}(2\omega)$, in general, differs from $n(\omega)$ in $L_{nl}(2\omega)$.

Disentangle $\chi^{(2)}$ components

Each interface in the multilayer structure is a source of SHG, which itself includes of SH fields generated with different $\chi^{(2)}$ components (referring to Table. 3.2). To simplify the model, we assume that there is a dominant $\chi^{(2)}$ component at each interface. They are distinguished based on their magnetic properties and the possibility to couple with SPP field. For example, in the structure of Au/Co/Ag/substrate mounted on the Kretschmann configuration, SPP fields cannot be excited at the Ag/substrate interface. And if the distance from this interface to the open surface is larger than the field skin depth, i.e. 24 nm, the SH polarization located at the Ag/substrate interface is non-resonant with the SPP excited in Au/air surface. This SH source is also non-magnetic, since it is not in contact with the ferromagnetic Co layer.

The field amplitude at each interface of the multilayer system can be resolved by the MTM. Fig. 3.12 shows the field distribution over angle of incidence in the sample (28 nm)Ag/ (10 nm)Co/ (5 nm)Au. In this simulation, the field at the metallic side of the interface is taken; for example, $E_z(\omega)$ and $E_x(\omega)$ at Au side in the interface of Au/air is taken for calculation of sheet polarization $P_x(2\omega) \propto \chi_{xzx} E_z(\omega) E_x(\omega)$. For the interfaces between ferromagnetic and non-magnetic metals, such as Co/Au and Ag/Co, the fields are taken at the ferromagnetic side. Due to the boundary condition, E_x is continuous across the interface, but E_z will differ by a ratio of two dielectric functions.

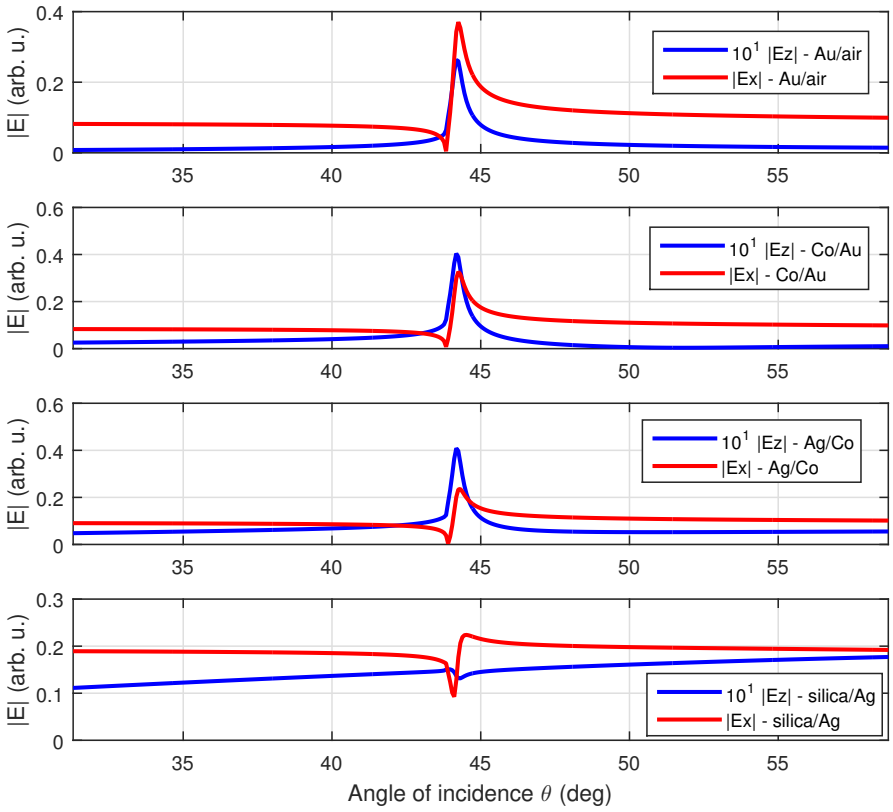

Figure 3.12 – Angular dependence of electric field $|E|$ components of p-polarized incident light, calculated at each interface using MTM method for the structure (25 nm)Ag/ (10 nm)Co/ (5 nm)Au doposited on fused-silica.

As can be seen in Fig. 3.12, the roles of E-fields at the interfaces of Co/Au and Ag/Co in the trilayer are similar. Thus the model can be further simplified by considering the Co/Au interface the only source of the magnetization-induced SHG. The dominant role of each metallic layer in the structure Au/Co/Ag is summarized in Table. 3.3 below.

In general, three non-magnetic susceptibilities (χ_{zzz}, χ_{zxx} and χ_{xzx}) at the interface Co/Au are non-zero, but they do not have as much influence compared to the interfaces

Interfaces (index)	Dominant $\chi^{(2)}$	Magnetic properties	SPP-resonance
Au/air (3)	χ_{xzx} or χ_{zxx}	no	yes
Co/Au (2)	χ_{xxx}	yes	yes
glass/Ag (1)	χ_{zzz}	no	no

Table 3.3 – The roles of different $\chi(2)$ susceptibilities in the multilayer structure of Au/Co/Ag/glass.

of metal/dielectric, such as interface 1 (glass/Ag) and interface 3 (Au/air).

Fit the SPP-induced magnetic SHG by numerical methods

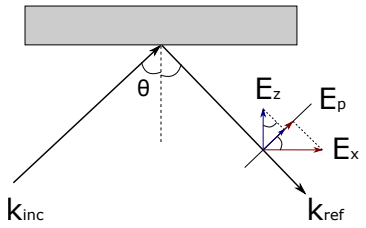

Figure 3.13 – Illustration for the electric field components in reflection.

The SPP-induced magnetic SHG in the trilayer of Au/Co/Ag above can be formulated as

$$\begin{aligned} I(2\omega)(\pm M) = \Big| & \chi_{zzz} E_{1z} E_{1z} \sin\theta \\ & + L_{nl}(2\omega)\big[\chi_{xzx} E_{3z} E_{3x} \cos\theta \\ & \pm \chi_{xxx} E_{2x} E_{2x} \cos\theta\big]\Big|^2 \end{aligned} \tag{3.23}$$

where χ_{zzz} is set as 1, and the other $\chi^{(2)}$ components, such as χ_{xzx} and χ_{xxx}, are complex factors relative to χ_{zzz}. $\sin\theta$ and $\cos\theta$ are respectively the projection of E_z and E_x field components to the reflected electric field, as seen in Fig. 3.13.

Including all the sources at different interfaces, the angular dependence of magnetization-induced SHG in the trilayer can be simulated numerically, as shown in Fig. 3.14. Comparing different sets of $\chi^{(}2)$-components, it is observed that χ_{xxx} always gives better angular consistency with the magnetic contrast, thus it could be the dominant magnetic (odd) susceptibility component.

3.4.2 Reverse approach

Eq. 3.19 suggests that from the experimental magnetic contrast ϕ, one can estimate the nonlinear SPP coupling efficiency $L_{nl}(2\omega)$ without the usage of effective medium approximation described in the forward approach. Recalling that χ_{xxx} is considered as the dominant magnetic second-order susceptibility, the non-resonant and resonant magnetic SHG sources can be formulated as $b = \chi_{xxx,1} E_x E_x$ and $d = \chi_{xxx,2} E_x E_x$, respectively. Thus, the new magnetic contrast ϕ can be re-written as:

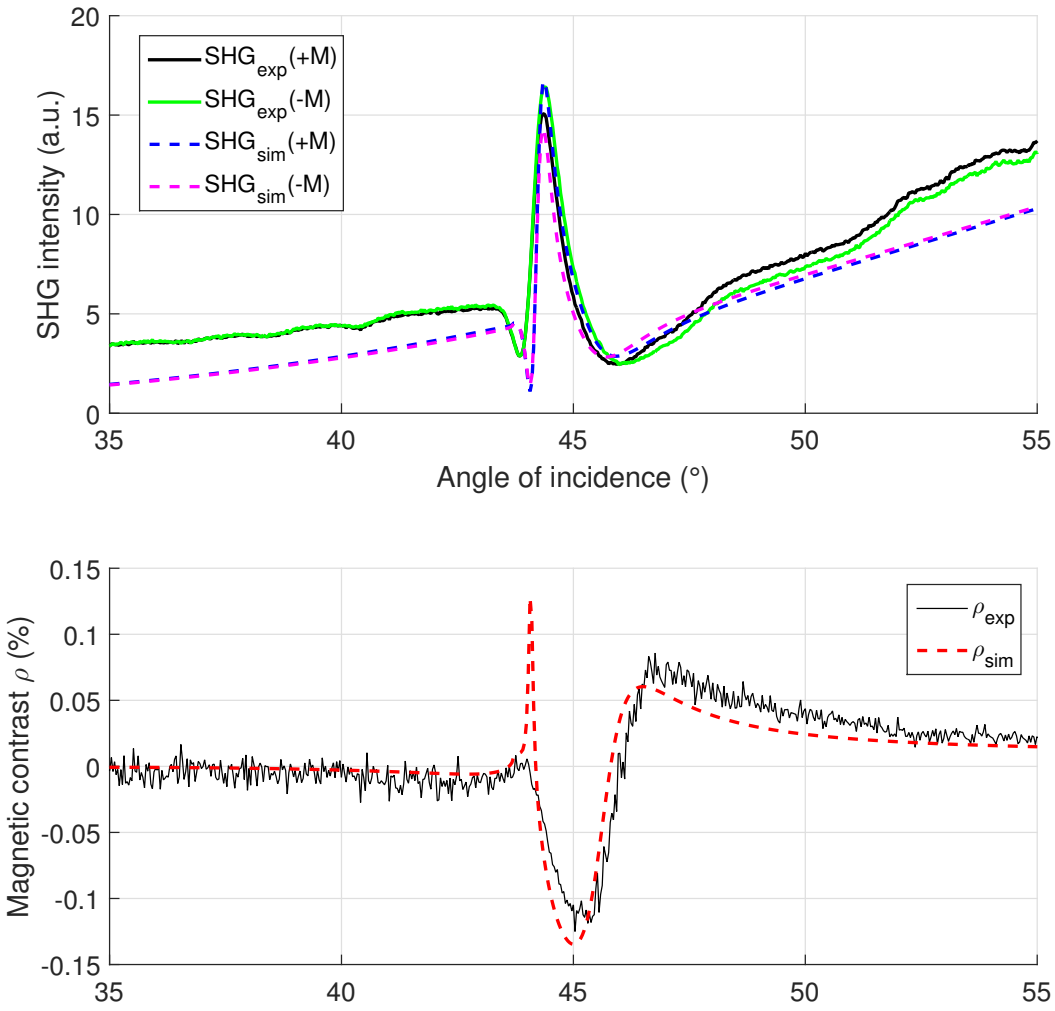

Figure 3.14 – Forward approach: (a) Simulated curves (dashed lines) are fitted with the experimental mSHG($\pm M$) (solid lines) measured for the structure (5 nm)Au/ (10 nm)Co/ (25 nm)Ag excited at fundamental wavelength 1200 nm. (b) Comparison of the experimental (black) and simulated (red) magnetic contrasts. In the simulation, only one dominant $\chi^{(2)}$-component is considered at each interface, referring to Eq. 3.23.

$$\begin{aligned}\phi &= \frac{\Delta I_{2\omega}}{\sqrt{I_{2\omega}(m=0)}} \\ &= 2\Re\{|b+Ld|e^{i\varphi}\} \\ &= 2\Re\{|(\frac{b}{d}+L)d|e^{i\varphi}\} \\ &= 2\Re\{(\xi+L)\chi_{xxx,2}E_xE_xe^{i\varphi}\}\end{aligned} \tag{3.24}$$

where ξ is the complex ratio between the non-resonant and resonant magnetic susceptibilities $\xi = \chi_{xxx,1}/\chi_{xxx,2}$.

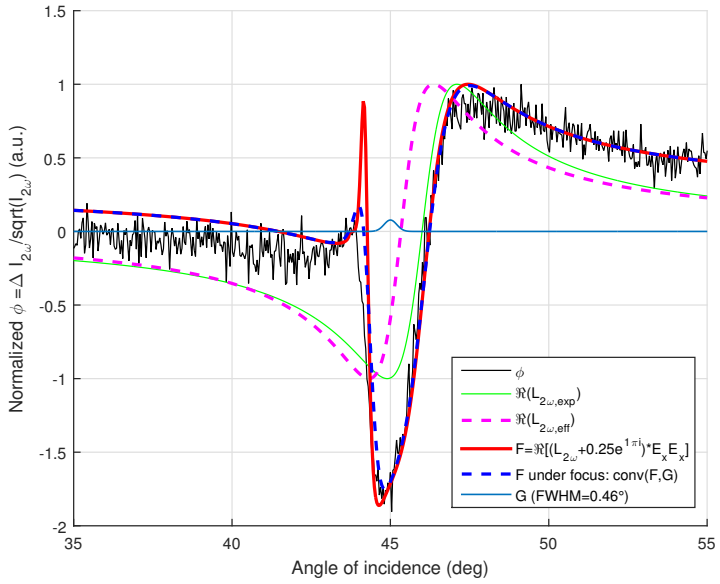

Figure 3.15 – Reverse approach: fit the magnetic contrast ϕ to estimate the Lorentzian function. $\phi = \frac{dI(\pm M)}{\sqrt{I}}$ (black solid) is well fitted with $F = \Re\{(b+Ld)\}$ (red solid) in the structure of (5 nm)Au/ (10 nm)Co/ (25 nm)Ag. The measurement was performed at the fundamental wavelength 1200 nm.

This magnetic contrast ϕ is deduced experimentally by

$$\phi = \frac{I_{2\omega}(+M) - I_{2\omega}(-M)}{\sqrt{I_{2\omega}(+M) + I_{2\omega}(-M)}} \tag{3.25}$$

Fig. 3.15 illustrates the magnetic contrast ϕ normalized to unity for the sample (5 nm)Au/ (10 nm)Co/ (25 nm)Ag. The experimental ϕ (black solid) is fitted by the numerical contrast F calculated by Eq. 3.24 (red solid). The convolution of F with a Gaussian function G (blue curve), which imitates the focusing condition in the experiments, gives the blue dashed curve, a closer fit to the experimental ϕ (black solid).

From the experimental ϕ (black line), one can obtain the Lorentzian function of the form

$$L(\theta) = \frac{\Gamma}{(\theta-\theta_0)+i\Gamma}$$

taking the resonant angle θ_0 where the angular derivative $\delta\phi/\delta\theta$ is highest. The slope of the normalized ϕ gives us an estimation for the angular broadening of the Lorentzian function Γ. Γ, estimated by this experimental approach, has the value of $\Gamma_{exp} \approx 1.1\,\text{deg}$, which is very close to that calculated for the same structure $\Gamma_{cal} \approx 1.02\,\text{deg}$ using effective medium approximation.

The Lorentzian function $L_{exp}(\theta) = \frac{1.1^\circ}{(\theta - 46^\circ) + i1.1^\circ}$ can be substituted for $L_{nl}(2\omega)$ in the Eq. 3.23 in order to fit for the $I_{2\omega}(\pm M)$. The conventional magnetic contrast ρ can then be deduced according to Eq. 2.50. The reverse approach is advantageous because magnetic contrast is a stable quantity, which depends on the relative phase between magnetic and non-magnetic components, and is not affected by the scattering of SHG. Ideally, it permits to predict the nonlinear SPP coupling condition when the dielectric function of a material consisted in the multilayer structure is unknown, an usual case for ultra-thin layers.

3.4.3 Conclusion about two simulation approaches

In Fig. 3.15, the green solid line shows the real part of the Lorentzian function estimated by the reverse approach, with the resonant angle $\theta_{exp} \approx 46\,\text{deg}$ and the angular broadening $\Gamma_{exp} \approx 1.1\,\text{deg}$. In contrast, the magenta dashed line shows the real part of the Lorentzian function calculated by the forward approach using effective medium approximation, with $\theta_{cal} \approx 45.3\,\text{deg}$ and $\Gamma_{cal} \approx 1.02\,\text{deg}$. Comparing between the two approaches, one sees that the angular broadening Γ does not differ much, but the resonant angle θ_0 in the reverse approach experiences a noticeable shift towards larger angles.

The forward approach helps to guess the dominant susceptibility components at different interfaces, i.e. non-magnetic χ_{zxx} or χ_{xzx} at Au/air and magnetic χ_{xxx} at Co/Au interface. On the other hand, the reverse approach allows to estimate the nonlinear SPP coupling efficiency $L_{2\omega}$ directly from the experimental magnetic contrast, without knowing the dielectric functions and thickness of individual layer. The forward approach has been employed in a prior research [6] to simulate the magnetization-induced SHG, while the reverse approach is introduced exclusively in this work.

3.5 Dispersion of Lorentzian function

From the effective dielectric function $\epsilon_{eff}(\lambda)$ estimated using effective medium approximation, one can get the dispersion of the Lorentzian function

$$L(\lambda) = \frac{\Gamma(\lambda)}{\Big(\theta - \theta_0(\lambda)\Big) + i\Gamma(\lambda)}$$

for the structure (5nm)Au/ (10nm)Co/ (25nm)Ag, as shown in the graph 3.16. It is seen that the resonant angle θ_0 does not vary a lot at the infrared spectral range. In contrast, the angular broadening of Lorentzian function Γ increases for shorter fundamental wavelength and peaks at 650 nm (SHG at 325 nm) due to the interband transition threshold of silver (at ≈3.8 eV).

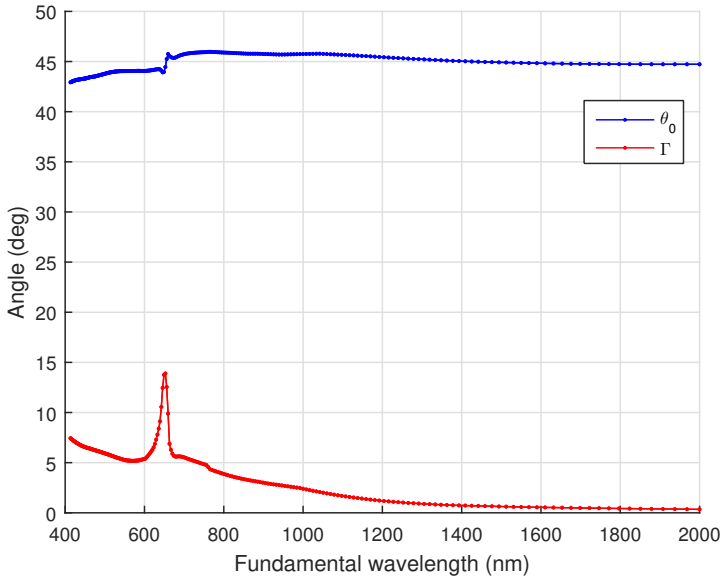

Figure 3.16 – Dispersion of the Lorentzian function is shown via $\theta_0(\lambda)$ (blue) and $\Gamma(\lambda)$ (red).

Even though the dispersion of magnetic contrast does not depend only on the dispersion of Lorentzian function L but also on the fundamental field $E_x(\omega)$ according to Eq. 3.24, the dispersion of the Lorentzian function is the main factor that affects the SH magneto-optical effects. The experimental data of the conventional magnetic contrast ρ are shown at different fundamental wavelengths in Fig. 3.17. It is clear that shorter fundamental wavelengths cause angular broadening in the SH magnetic contrast, in consistence with the increased Γ in Fig. 3.16.

3.6 Discussion

3.6.1 Bilayer structures

Now we return to the nonlinear magneto-plasmonics on sample (20nm)Au/ (30nm)Co/ sapphire, which has been discussed briefly in section 3.2.1. The experimental SH intensities at opposite magnetizations are shown in Fig. 3.18a as green and black dots. The measured SH magnetic contrast ρ is plotted in Fig. 3.18b as magenta dots. Using the reverse approach, one can obtain the experiment-extracted Lorentzian L_{fit}, shown as the violet dashed line in Fig. 3.18c. Applying L_{fit} in Eq. 3.23, the simulated SHG($\pm M$) are deduced and plotted as the green and black solid lines in Fig. 3.18a. The parameters used in the fitting are summarized in Table 3.4. The simulated curves reproduce all the features of the angular dependence of the mSHG, such as the peak at 35.4°, the dip at 36.1° and the background. The magnetic contrast ρ is given by substituting the simulated SHG($\pm M$) into Eq. 2.50, and then plotted as the magenta solid line in Fig. 3.18b. Except the small peak at 35.1°, the calculated contrast is in

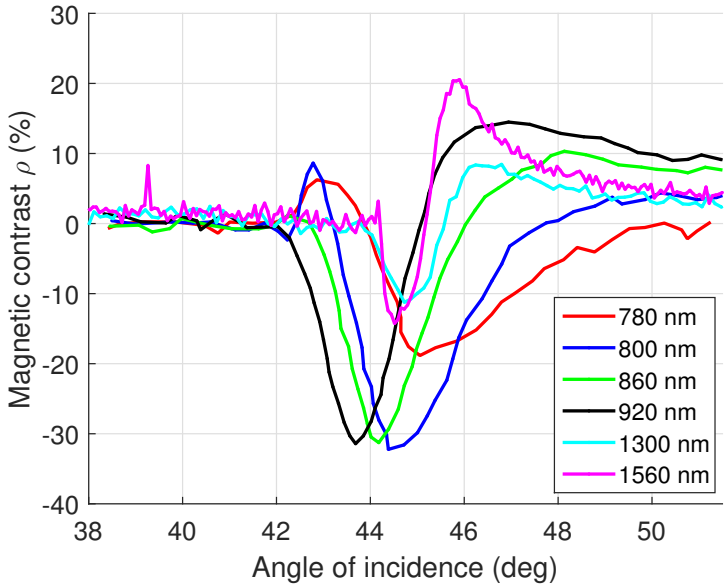

Figure 3.17 – The angular dependence of the conventional magnetic contrast ρ is broadened at short fundamental wavelengths. The graph combines the data from Ref. [6] (780-920 nm) and the data measured in this work (1300-1560 nm) for the sample of (5nm)Au/ (10nm)Co/ (25nm)Ag.

Interface	**Non-resonant**	**Resonant**
Au/air (3)	0	$\chi_{zzz,3}E_{3z}E_{3z}$
Co/Au (2)	$\chi_{zzz,2}E_{2z}E_{2z}$	$\pm\chi_{xxx,2}E_{2x}E_{2x}$
Co/sapphire (1)	$\chi_{xzx,1}E_{1z}E_{1x}$ $\pm\chi_{xxx,1}E_{1x}E_{1x}$	0

Table 3.4 – Parameters used for the simulation of mSHG in bilayer Au/Co. E_1, E_2 and E_3 represent for the fundamental field $E(\omega)$ taken at the interface Co/sapphire (Co side), Co/Au (Co side) and Au/air (Au side), respectively.

high agreement with the experimental data (magenta dots), espcially the double-dip and the background contrast of 60%.

Fig. 3.18c shows the Lorentzian functions $L_{lin}(\omega)$, $L_{lin}(2\omega)$ and $L_{nl}(2\omega)$ calculated based on the forward approach (Eq. 3.5 and 3.22). Each of them represents for a different SPP momentum-matching condition. We can see that the experimentally extracted Lorentzian L_{fit} (violet dashed line) is highly consistent with the calculated $L_{nl}(2\omega)$ (yellow solid line). Importantly, the angles of the double zero-dips feature in the magnetic contrast ρ (Fig. 3.18b) coincide with the resonant angles of the linear Lorentzian at fundamental wavelength $L_{lin}(\omega)$ and the second-harmonic Lorentzian $L_{nl}(2\omega)$. These are the evidences for the destructive interference of the SPPs and the magnetic second-harmonic field.

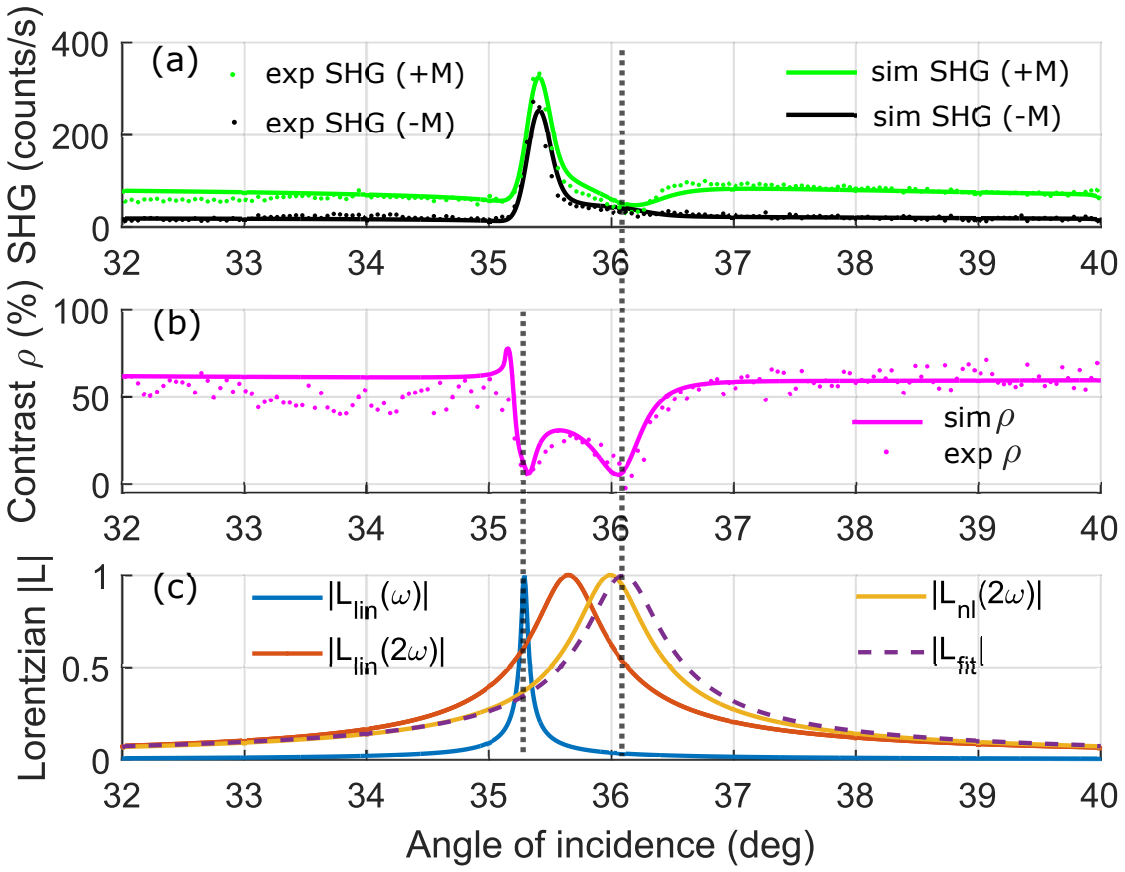

Figure 3.18 – Angular dependence for the bilayer (20 nm)Au/ (30 nm)Co excited at the fundamental wavelength 1560 nm. **(a)** SHG intensity upon the reversal of magnetization ±M (dots) and their corresponding simulations (solid lines) and **(b)** transversal SH magnetic contrast ρ in **(c)** The Lorentzian functions $L_{lin}(\omega)$, $L_{lin}(2\omega)$ and $L_{nl}(2\omega)$ are calculated based on the forward approach, and each of them represents for a different SPP momentum-matching condition. L_{fit} was estimated based on the reverse approach.

Interface	Non-resonant	Resonant
Effective Co/Au/air (2)	0	$\chi_{zxx,2}E_{2x}E_{2x}$ $\pm\chi_{xxx,2}E_{2x}E_{2x}$
Ag/silica (1)	$\chi_{zzz,1}E_{1z}E_{1z}$	0

Table 3.5 – Dominant SH field components assumed for the mSHG in trilayer Au/ Co/ Ag. E_1 and E_2 correspond to the fundamental field $E(\omega)$ taken at the bottom interface of Ag/ silica (Ag side) and the effective top interface of Co/ Au/ air, respectively.

3.6.2 Trilayer structures

Similar simulation can be performed for the mSHG in the trilayer of Au/Co/Ag. Here the sample (5 nm)Au/ (10 nm)Co/ (25 nm)Ag is taken as an example. Following the reverse approach described in the previous section, the experimental Lorentzian L_{fit} (blue dashed line) can be extracted from the magnetic contrast ϕ defined in Eq. 3.19 (black dots), as shown in Fig. 3.19a. Compared to the Lorentzian $L_{nl}(2\omega)$ (green solid line) calculated based on the effective medium approximation, L_{fit} has similar angular width, but its resonant angle shifts to 46°. The shift of 0.7° of the L_{fit} might result from the error in the input refractive indices of metallic layers and substrate. In the calculation, the natural corrosion of the metallic layers, especially cobalt, was not taken into account. In fact, the cobalt layer in the trilayer is protected by only 3-5 nm-thick gold layer, and is more vulnerable to the oxidation than that in the bilayer structure. Thus, the experimentally extracted nonlinear Lorentzian function L_{fit} appears to be a good assumption to fit the data when the quality of the structure is not clear. L_{fit} Fig. 3.19. Fig. 3.19b shows the experimental SH emission $SHG_{exp}(\pm M)$ (green and black lines) and the simulated ones (magenta lines). In this simulation, only two interfaces are considered: the effective top interface including Co/Au/air, and the bottom interface Ag/silica. Unlike the case of bilayer, there is only one source of magnetic SH emission considered in the trilayer, which is the top surface. The dominant SH field components assumed for the simulation of the mSHG in Fig. 3.19b are summarized in Table. 3.5. The figure shows agreement between the experimental data and the calculation based on the reverse approach, as good as the fitting based on the forward approach in Fig. 3.14. The conventional SH magnetic contrast ρ can also be calculated from the simulated $SHG_{sim}(\pm M)$, and is shown as the red solid curve in Fig. 3.19c. The experimental contrast, presented as black dots, is well fitted by the simulated one.

The high consistence between the numerical simulation and the experimental data shows the validity of the reverse approach, which estimates the resonance of the nonlinear SPP(2ω) based on the new magnetic contrast $\phi = \frac{\Delta I}{\sqrt{I}}$. Furthermore, it confirms the fingerprint of the nonlinear SPP coupling efficiency, represented by the Lorentzian function $L_{nl}(2\omega)$, on the magnetization-induced SHG.

As shown before in Eq. 3.24, the factors affecting the nonlinear magnetic contrast in the plasmonic structures include the second-harmonic SPP excitation $L_{nl}(2\omega)$, the fundamental field at magnetic interface $E_x(\omega)$ and the phase difference φ between even and odd second-harmonic fields. In order to see the reason why the magnetic contrast

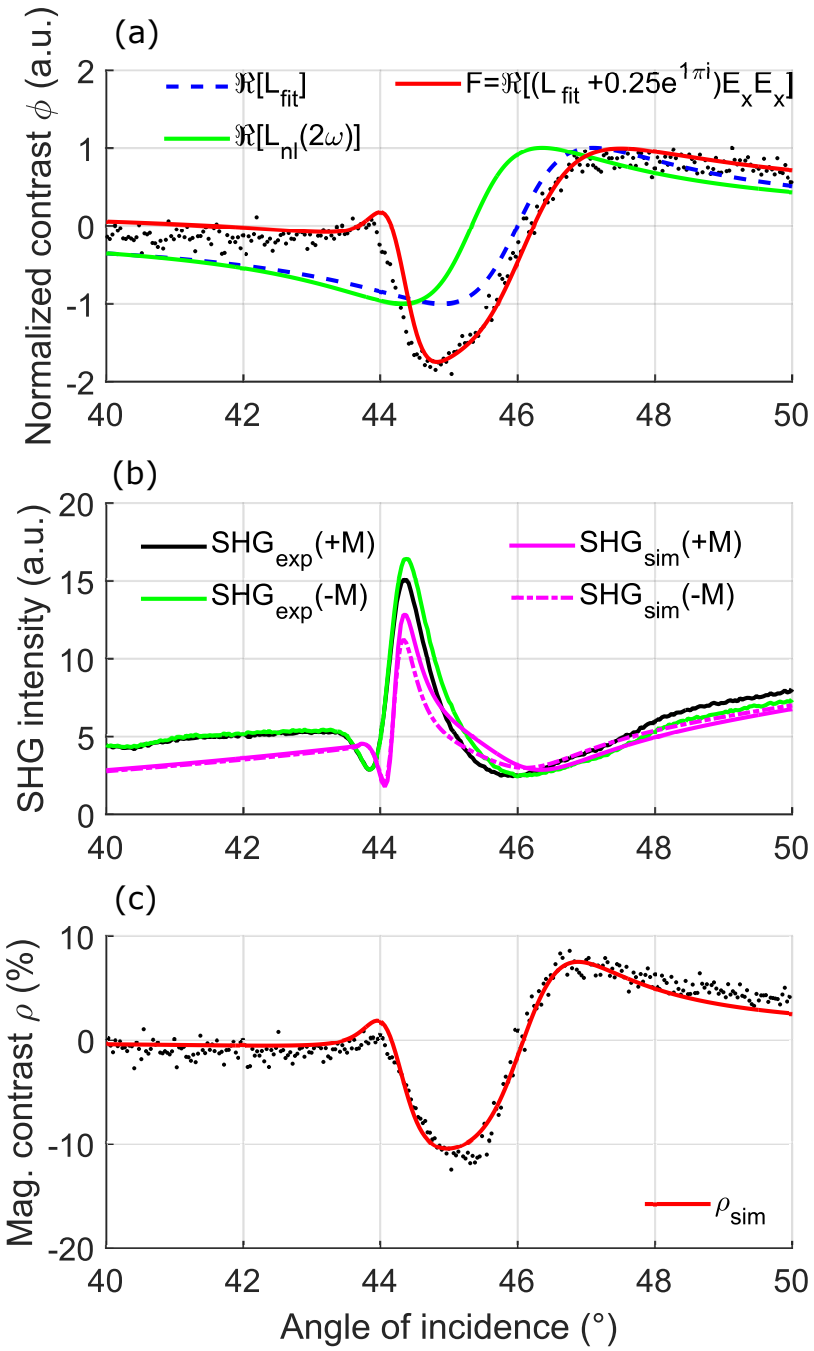

Figure 3.19 – Angular dependence of the SH intensity and magnetic contrasts of trilayer (5 nm)Au/(10 nm)Co/(25 nm)Ag excited at the fundamental wavelength 1200 nm. **(a)** L_{fit} (blue dashed line) in the nonlinear Lorentzian function estimated based on the reverse approach. $L_{nl}(2\omega)$ (green solid line) is the Lorentzian function calculated based on the forward approach. The normalized magnetic contrast ϕ (black dots) is in agreement with F applying L_{fit} to the Eq. 3.24. Similarly, L_{fit} can be used to fit the SHG(±M) **(b)** and the conventional magnetic contrast ρ **(c)**.

in the trilayer of Au/Co/Ag is stronger when the Ag layer is thinner, we will inspect the dependence of the aforementioned factors on the Ag thickness. Fig. 3.20a shows the Lorentzian function $L_{nl}(2\omega)$ calculated for the set of trilayer (5 nm)Au/ (10 nm)Co/ (15-25-35 nm)Ag, where only the thickness of Ag layer is varied. Fig. 3.20b shows the product of $E_x(\omega)E_x(\omega)$ calculated based the MTM for the three samples. One can see in Fig. 3.20a that the variations in the resonant angle and the angular width of the Lorentzian $L_{nl}(2\omega)$ in the three samples are negligible. In contrast, Fig. 3.20b shows a strong dependence of the field amplitude on the thickness of Ag, the SPP active layer. Thus we can conclude that the main reason behind the high magnetic contrast of sample (5 nm)Au/ (10 nm)Co/ (15 nm)Ag is the strong concentration of fundamental field component $E_x(\omega)$ at interface Co/Au, i.e. the field enhancement of linear SPP(ω).

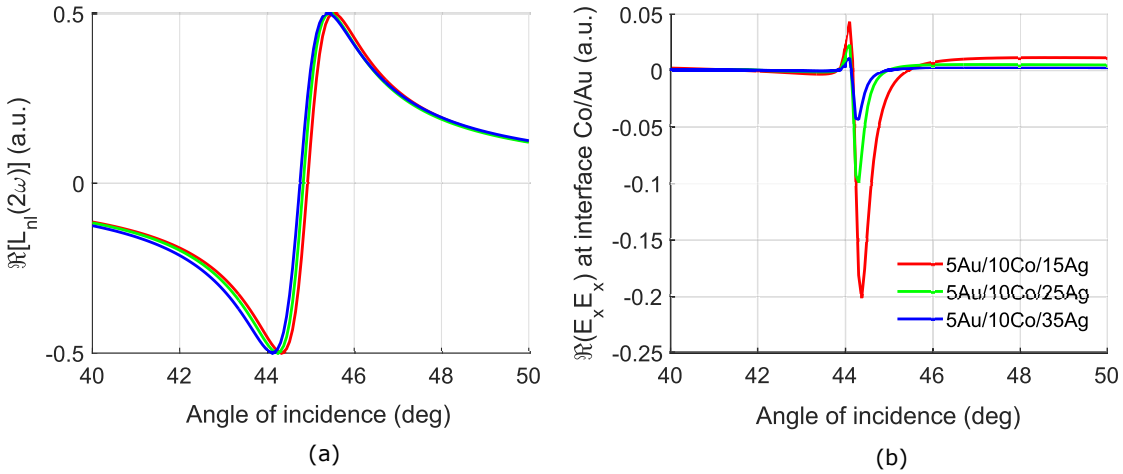

Figure 3.20 – Real part of **(a)** the nonlinear Lorentzian $L_{nl}(2\omega)$ and **(b)** the product E_xE_x at the magnetic interface Co/Au calculated for trilayer (5 nm)Au/ (10 nm)Co/ (15-25-35 nm)Ag.

3.6.3 SHG due to instantaneous change of damping constant

From the simulations of both the bilayer and the trilayer, one can see that χ_{xxx} is the dominant magnetic SH susceptibility, which corresponds for the magnetic polarization localized at the Co/Au interface. This cannot be simply explained by the model of anharmonic oscillator in section 2.3 because the motion of electrons along metallic surface driven by $E_x(\omega)$ should not encounter any potential wall[7]. Thus, another explanation is introduced for this case.

First, we consider the case when an external magnetic field is introduced and not parallel to the initial velocity of electron $\boldsymbol{B} \nparallel \boldsymbol{v}$. The oscillation of electrons in different metals experience different damping constants due to the direction of the magnetic field ($\pm B_y$). Fig. 3.21 shows the illustration of a charge dragged by E_x along the interface

[7]The model of anharmonic oscillator can explain for the case of electrons driven by $E_z(\omega)$, leading to χ_{zzz} for example.

between two metals. When the magnetic field B_y is applied, the trajectory $\boldsymbol{r}$ of the charge is deflected due to the Lorentz force. The direction of the moving change changes upon the reversal of the magnetic field.

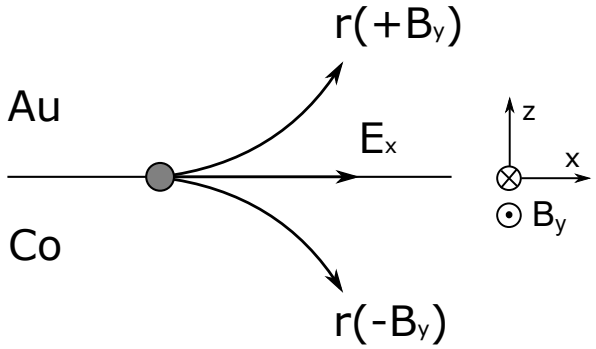

Figure 3.21 – Illustration of a charge at the boundary between two conducting media Co and Au. The trajectory of the moving charge is deflected towards different directions when the external magnetic field is reversed.

Now we consider the electrons travelling across the interface between the ferromagnetic Co and noble metal Au. According to Eq. 2.31 and 2.35, the trajectory of electrons at the fundamental frequency ω in Au and Co are

$$\begin{aligned} z_{Au}(t) &= \frac{1}{2}\frac{q}{m} \times \frac{E(\omega)}{\omega^2 + i\gamma_{Au}\omega}\left(\mathrm{e}^{-i\omega t} + \mathrm{e}^{i\omega t}\right) \\ z_{Co}(t) &= \frac{1}{2}\frac{q}{m} \times \frac{E(\omega)}{\omega^2 + i\gamma_{Co}\omega}\left(\mathrm{e}^{-i\omega t} + \mathrm{e}^{i\omega t}\right) \end{aligned} \tag{3.26}$$

where $\gamma_{Au} = 1/\tau_{Au}$ and $\gamma_{Co} = 1/\tau_{Co}$ are damping contansts in Au and Co, respectively. The trajectory of electrons in these two media at the excitation wavelength 1560 nm (ω=0.8 eV) are shown in Fig. 3.22, assuming that the scattering time of electron in Au $\tau_{Au} = 27\ fs$ and in Co $\tau_{Co} = 17\ fs$ [81]. The difference between the trajectories, shown by the yellow curve, is very small but it modulates at the doubled frequency. It is assumed that upon crossing the interface between Co and Au, an instantaneous change in the damping constant results in a nonlinear optical susceptibility. If the electrons are driven by the normal component of the incident field E_z, their trajectories should be affected by the external magnetic field $\pm B_y$ in a similar way. However, at the metal/ferromagnet interface, the coupled SPP can enhance E_x much stronger than E_z (see Fig. 3.12). This is most likely the reason for the dominance of the magnetization-induced SH polarization $P_x(2\omega, \pm M) \propto \chi_{xxx}E_x(\omega)E_x(\omega)$ in the magneto-plasmonic structures.

3.7 Conclusion

In this chapter, the SPP-induced second harmonic generation and magneto-optical effects have been described using physical expressions. Based on that, two simulation methods, forward and reverse approaches, have been proposed, and both have

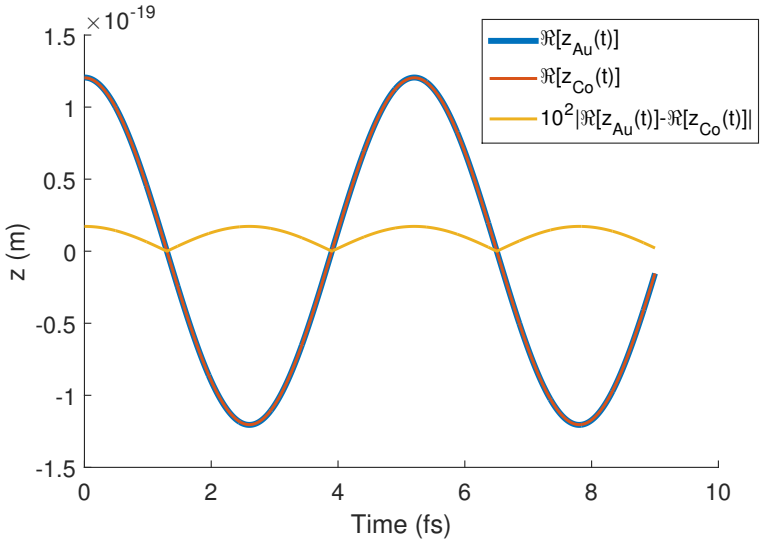

Figure 3.22 – The trajectory of electrons in the Au and in the Co bulk, assuming that the scattering time of electron in Au τ_{Au}=27 fs and in Co τ_{Co}=17 fs[81]. The difference between two trajectories has the doubled frequency.

demonstrated high consistencies with experimental signals. One important part in this chapter is the discussion about the excitation condition of different SPP modes, their coupling efficiency $L(\theta)$ and dispersion. The models successfully explain the effect of linear and nonlinear SPP modes on second-harmonic magneto-optical responses in different multilayer structures, the trilayer Au/Co/Ag and the bilayer Au/Co.

It was also demonstrated experimentally that it is possible to tune the nonlinear magnetic signals by varying the thickness of the plasmonic layer, which is a way to tailor the SPP field. It represents the first step towards the new generation of nonlinear magneto-plasmonic devices for light modulation at the nano-scale. Besides, the new observation of magneto-plasmonics on bilayer Au/Co opens many opportunities for our research. Since the bilayer metal/ferromagneti structure has been shown to be a "perfect" structure for ultrafast acousto-plasmonics [7] and exchange-coupled magnonics [31], the combination of ultrafast magnonics and plasmonics can be expected. Their outstanding heat conduction properties allow the nonlinear (magnetic SHG and femtosecond time-resolved pump-probe) optical measurements to be performed at high radiation powers, resulting in the significant increase of spatially transient electron and lattice temperature in ferromagnetic cobalt.

Chapter 4

Nonlinear magneto-optics in diffraction anomalies

We have discussed in chapter 2 that propagating surface plasmon polaritons can be excited in metallic gratings. In this geometry, the discrepancy between the incident wave-vector and the SPP wave-vector is compensated by a multiples of grating wave-vectors G. The advanced technologies in nano-fabrications now allow to go further. Periodic structures with sub-wavelength periodicity, so-called optical meta-surfaces, can be produced with high precision and regularity. Besides the delocalized surface modes, surrounding the nanosized metallic objects is the localized surface plasmon resonances (LSPRs) [3, 56, 114, 115]. Under certain conditions, the arrays of nanostructures permit the hybridization of the LSPRs and the Wood's anomaly across the surface, causing spectrally narrow resonances, commonly referred to as surface lattice resonances (SLRs) [46, 47, 52, 53]. This chapter is devoted to present the experimental observation of the second-harmonic nonlinear Wood's anomaly in nickel nanodimers arrays.

4.1 Nonlinear Wood's anomaly

4.1.1 Diffraction on grating

A conventional diffraction grating requires the grating periodicity Λ to be larger than a half of the optical free space wavelength λ_0 ($\Lambda > \lambda_0/2$) to ensure the presence of at least one diffraction order. On Fig. 4.1 are illustrated the cases of diffraction on a grating in the linear and nonlinear-optical regimes. For gratings with opaque substrates, the diffraction orders can be observed in reflection as in Fig. 4.1. For transparent substrates, the diffraction can also occur in transmission, but at smaller diffraction angles due to the dispersion in the substrate. Fig. 4.1a-b show the case of a regular grating with the periodicity $\Lambda \geq \lambda/2$ irradiated at an angle of incidence θ in the free space and reciprocal space, respectively. The phase-matching conditions for diffraction can be conveniently illustrated in the reciprocal space (Fig. 4.1b).

The emergence and direction of a diffraction order m_{lin} rely on the phase-matching

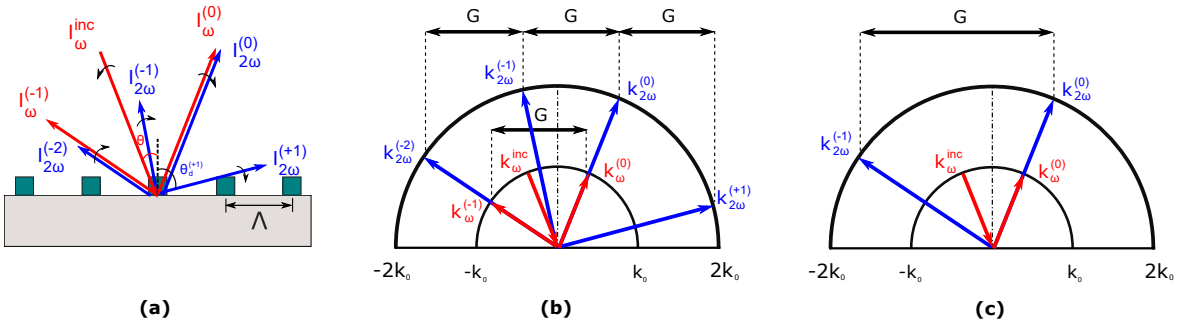

Figure 4.1 – (a) Linear (red) and nonlinear (SH, blue) diffraction orders in reflection on a grating with a periodicity $\Lambda > \lambda/2$. When the angle of incidence θ of the fundamental radiation I_ω^{inc} increases in the counter-clockwise direction, all diffraction orders rotate clock-wise. (b-c) In the reciprocal space, linear and nonlinear diffraction orders are shifted by a multiple of the grating wavevector $G = 2\pi/\Lambda$. (b) For $G \leq 2k_0$ or $\Lambda \geq \lambda/2$, both linear and second-order nonlinear diffraction orders can be observed. (c) When $2k_0 < G < 4k_0$ or $\lambda/4 < \Lambda < \lambda/2$, besides the specular $m = 0$, only the second-order nonlinear diffraction order with $m_{nl} = -1$ appears.

condition between the wavevectors, as following:

$$k_x^{inc}(\omega) + m_{lin}G = k_x^d(\omega) \tag{4.1}$$

where $k_x^{inc} = k_0 \sin\theta$ and $k_x^d = k_0 \sin\theta_d$ are in-plane (x-) components of the incident wavevector k^{inc} and the diffracted wavevector k^d, respectively. Here, $k_0 = 2\pi/\lambda_0$, θ is the angle of incidence, θ_d is the diffracted angle of the corresponding diffraction order (see Fig. 4.1), and $G = 2\pi/\Lambda$ is the wavevector of the grating. m_{lin} is an integer, which represents the linear diffraction order. A similar condition can be written for the nonlinear (SH) diffraction [116]:

$$2k_x^{inc}(\omega) + m_{nl}G = k_x^d(2\omega) \tag{4.2}$$

where another integer $m_{nl} \neq m_{lin}$ is introduced to indicate the nonlinear diffraction order.

These phase-matching conditions require the linear wavevector k_ω (red) and the SH wavevectors $k_{2\omega}$ (blue) to rotate within the semicircles with the radii k_0 and $2k_0$, respectively. The linear and nonlinear diffraction orders are shifted by a multiple of the grating wavevector G. Comparing Eq. 4.1 and Eq. 4.2, one can see that a linear diffraction order m_{lin} is always accompanied by a SH diffraction order $m_{nl} = 2m_{lin}$ once $k_x^d(2\omega) = 2k_x^d(\omega)$. Indeed, the parallel wavevectors of the linear diffraction order $m_{lin} = -1$ and the SH diffraction order $m_{nl} = -2$ in Fig. 4.1b ensure that these diffraction orders can be excited at the same angle of incidence θ and observed at the same diffraction angle θ_d.

In the nonlinear regime, one can extend G to be larger than $2k_0$ ($\Lambda < \lambda/2$) and still observe the presence of the diffraction orders, which is the case illustrated in Fig. 4.1c. Besides the specular $m = 0$, there is no other linear diffraction order, but the nonlinear diffraction order $m_{nl} = -1$ can be observed. Thus it becomes possible to combine the

meta-surfaces, which are characterized by a much smaller periodicity than the free space wavelength $\Lambda \ll \lambda$ [50, 57, 58], and the nonlinear diffraction. Indeed, the same periodic structure can serve as a meta-surface for the fundamental light at λ, and as a regular grating for the harmonic radiations with wavelengths λ/n ($n > 1$). Overall, the condition for this transition regime $\lambda \gg \Lambda > \lambda/2n$ is expected to be easily fulfilled in the visible and near-infrared optical range.

4.1.2 Wood's anomaly

"Wood's anomaly" is defined as the redistribution of the light energy between different diffracted beams upon the emergence of a new diffraction order propagating along the grating surface [1]. In other words, it occurs when one of the diffraction orders is parallel to the grating surface, i.e. the in-plane component of the diffraction wavevector k_x^d is highest. In the case of transparent substrate, there would be two Wood's anomalies of the same order; one travels along the interface between grating and open space (air for simplicity), and the other occurs at the interface between grating and substrate. Even though SPP can be excited where there is high relative content of the metal (despite high optical losses in ferromagnetic transition metals), the large distance between the nanostructures can prohibit the propagation of the mode. Thus, using the terms "propagating SPP" is not rigorous and besides the historical reason, "Wood's anomaly" would be a better term to portray the surface mode excited in the periodic structures, which depletes the energy from the other diffraction orders upon its emergence.

The excitation of this surface mode should fulfill the following phase-matching condition:

$$k_x(\omega) + m_{lin}\frac{2\pi}{\Lambda} = k_s(\omega) \tag{4.3}$$

in the linear regime. Here $k_s(\omega)$ is the surface mode wavevector, corresponding to the linear Wood's anomaly with order m_{lin}. One can recognize that Eq. 4.3 is similar to the phase-matching condition of SPP on the grating surface described in Eq. 2.60 in section 2.4.2, even though SPP is not supposed to be excited in this structure. This comes from the fact that SPP is itself a type of electromagnetic surface waves [22] that can be excited by the momentum conservation. Following the highly similar formalism of the nonlinear SPP excitation in chapter 3 and the previous research [6, 99, 101, 116], we can outline the nonlinear excitation condition for the Wood's anomaly with order m_{nl}:

$$2k_x(\omega) + m_{nl}\frac{2\pi}{\Lambda} = k_s(2\omega). \tag{4.4}$$

In this work, the nonlinear-optical technique of magneto-induced second harmonic (SH) generation is employed to study the Wood's anomaly, i.e. the intrinsic property of an optical grating in the nonlinear transition regime.

4.2 Experimental methods

The angle-dependent SH spectroscopy with tunable femtosecond laser source was performed on a rectangular array of nickel dimers featuring a nanoscale gap, similar to

that studied in Ref. [46]. The purpose of this study is to observe the nonlinear Wood's anomaly (Fig. 4.1c and Fig. 4.2a) and compare its nonlinear-optical properties with the general case where linear and nonlinear Wood's anomalies coexist (Fig. 4.1b).

The sample under investigation was designed and built by our collaborator at Departement of Physics and Astronomy, Uppsala University, Sweden. It is an array of nickel nanodimers deposited on a Si substrate, shown in Fig. 4.2. Good heat conductivity of Si (≈100 W/m·K at 100 °C [117]) ensures the sample damage resilience at high peak optical fluences required for sizeable nonlinear-optical effects. The nickel film was DC sputtered directly on the Si[100] substrate, and then the structure was patterned using electron beam lithography. The nanodisks (average diameter 145 nm, height 60 nm) are grouped into dimer cells with the air gap of about $15 - 60$ nm (in average 35 nm), as shown in Fig. 4.2c. Nickel structure is covered by a layer of natural oxide NiO, which is about 1-2 nm in thickness. The two axes of the array are denoted as p_L (longitudinal) and p_T (transverse), illustrated in Fig. 4.2 b. Along p_L, the average distance between two adjacent dimer cells is $\Lambda_L \approx 445$ nm. Along p_T, the periodicity is $\Lambda_T \approx 265$ nm (see Fig. 4.2c).

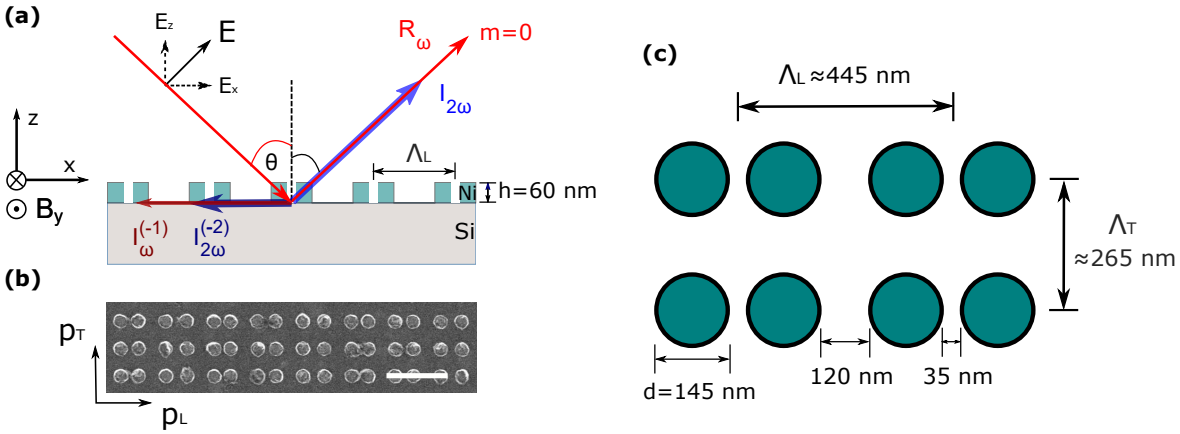

Figure 4.2 – (a) Schematic for the co-excitation of linear and nonlinear Wood's anomalies, denoted as $I_{\omega}^{(-1)}$ and $I_{2\omega}^{(-2)}$ respectively, in an array of nickel nanodimers. An external magnetic field is applied perpendicular to the plane of incidence. (b) Scanning electron microscopy image of the nickel nanodimers. The scale bar is 600 nm long. (c) Dimensions of the two-dimensional nanodisks array.

Assuming an isotropic interface and the p-polarized incident fundamental radiation, six nonlinear susceptibility components remain non-zero [37, 41], as summarized in Table. 3.2 in chapter 3. The SH fields generated through these components give rise to a far-field magnetization-dependent SH intensity $I_{2\omega}(\pm M)$. Originating in the interference of the odd and even SH sources, the variations of the SH intensity upon reversal of the in-plane magnetization M_y is conventionally quantified by the nonlinear magnetic contrast ρ defined in Eq. 2.50, similar to the study of the nonlinear transversal MOKE in the hybrid thin films (chapter 3).

To study Wood's anomalies in these nonlinear processes, we investigate the dependence of the far-field magnetization-induced SH intensity $I_{2\omega}(\pm M)$ on the in-plane

fundamental wavevector $k_x(\omega)$, which is related to the angle of incidence θ through $k_x = k_0 \sin(\theta)$. According to the definition, Wood's anomalies are the "uneven distribution of light"[1] between different diffraction orders. Putting the detectors at the output of the specular (zero diffraction order $m = 0$), it is expected to observe a drop in the linear reflectivity R_ω when a Wood's anomaly is excited at the fundamental frequency, and a drop in the SHG intensity $I_{2\omega}$ when the diffraction anomaly is excited at the double frequency.

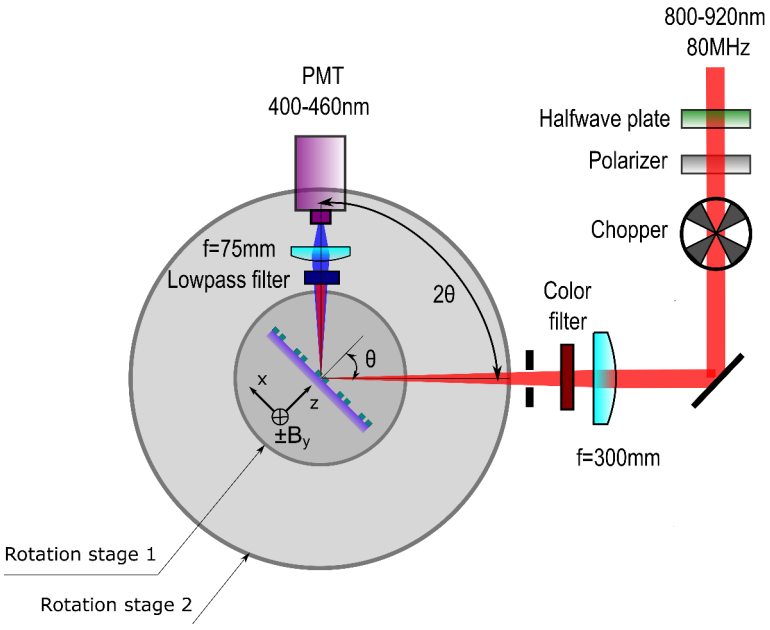

Figure 4.3 – The top-view of the experimental setup for nonlinear Wood's anomaly in the periodic structures.

The experiment was conducted on a goniometric platform which allows measuring the reflected signals at different angles of incidence, as illustrated in Fig. 4.3. Basically, it is similar to the setup utilized in chapter 3, but without the prism. The fundamental radiation is produced by a Ti:Sa laser (MaiTai HP from Spectra Physics), tunable in the spectral range between 690 and 1040 nm, with a pulse duration of ∼100 fs, repetition rate of 80 MHz. The p-polarized (TM) fundamental radiation was loosely focused on the sample surface (spot diameter 80 μm). The linear reflectivity R was measured using a biased silicon photodiode (Newport). The SH output was spectrally separated by a color BG-39 filter (Schott), collected by a lens and registered with a photomultiplier tube (Hamamatsu) operating in the photon counting regime. The external transverse magnetic field $B_y \geq$100 mT, was applied perpendicular to the plane of incidence, saturating the magnetization of the nanodimers.

The measurements were performed for two azimuthal angles of the sample (0° and 90°) corresponding to the two orientations of the spatial periodicity of the array with respect to the in-plane fundamental electric field and the magnetization direction ($E_x \parallel p_T$ and $E_x \parallel p_L$). In Ref. [56], it has been demonstrated that the electric field is highly localized in the dimer gap when E_x is oriented along longitudinal dimer axis

($E_x \parallel p_L$). When $E_x \parallel p_T$, the plasmon mode in the gap is strongly suppressed.

4.3 Results and discussions

4.3.1 Nonlinear Wood's anomaly and MOKE in nanodimers

The specular (zero diffraction order $m = 0$) linear reflectivity R_ω, the magnetization-dependent SH intensity $I_{2\omega}(\pm M)$, and the nonlinear magnetic contrast ρ were measured as function of the angle of incidence θ. Fig. 4.4a and Fig. 4.4b show the experimental data obtained at the fundamental wavelength $\lambda_0 = 820$ nm for the two different configurations $E_x \parallel p_T$ and $E_x \parallel p_L$, respectively.

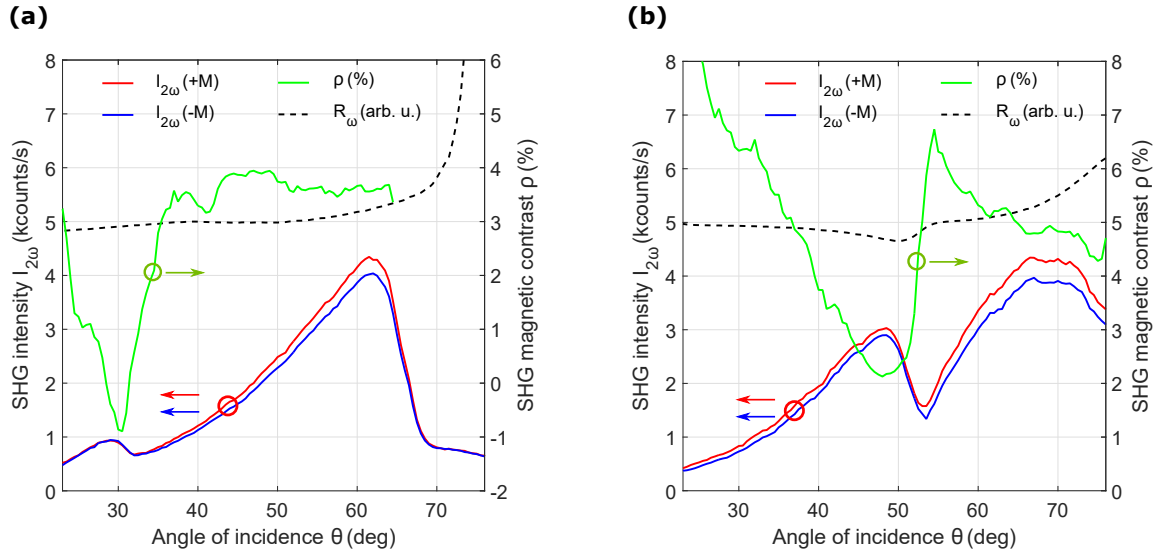

Figure 4.4 – The angular dependence of the linear reflectivity R_ω (dashed black), the SH intensity $I_{2\omega}(\pm M)$ for the two opposite directions of magnetization (solid red and blue), and the SHG magnetic contrast ρ (solid green) at the fundamental wavelength of 820 nm, measured for the case of (a) $E_x \parallel p_T$ and (b) $E_x \parallel p_L$.

In these plots, the high values of R_ω beyond $60° - 70°$ are a result of the normalization, where the raw data were divided by relatively small values near the Brewster's angle. Leaving aside this artificial effect, no significant drop of R_ω was observed in the case of $E_x \parallel p_T$ (Fig. 4.4a). It means that the linear Wood's anomalies are not excited in this configuration, which is consistent with the case illustrated in Fig. 4.1c, where $\Lambda_T < \lambda_0/2$ and no linear diffraction is allowed except the zero order. In contrast, in the $E_x \parallel p_L$ geometry with the spatial periodicity $\Lambda_L \approx$ 445 nm ($\Lambda_L > \lambda_0/2$), a dip of R_ω was observed at 50° (Fig. 4.4b) as a fingerprint of the linear Wood's anomaly excitation at around this angle.

In the nonlinear regime, the angular dependence of the SH intensity shows a recognizable minimum in both configurations, $E_x \parallel p_T$ and $E_x \parallel p_L$. The SH output is more than 10^3 counts/s, which is nearly an order of magnitude higher than the SH

signal from a bare silicon substrate ($\approx$ 600 counts/s). In fact, the SH output from these arrays are comparable to the SPP-enhanced SH yields observed in the thin films in chapter 3 and in prior research [6, 7]. The pronounced characteristic drops of the SH signals, appearing at 32° for $E_x \parallel p_T$ in Fig. 4.4a and 53.5° for $E_x \parallel p_L$ in Fig. 4.4b, originate in the destructive interference of the SH fields. In thin continuous metal films, the SH peak is usually observed at the same angle of incidence as the dip in the linear reflectivity. And so, the most efficient SPP excitation at the fundamental frequency ω is accompanied by the most prominent enhancement of the electric field E_ω.

A deviation from this highly intuitive picture, manifesting in the experiment as a noticeable angular shift of the SH intensity peak, is indicative of a highly lossy plasmon-polariton mode [100, 102]. However, nonlinear excitation of the Wood's anomaly in nanodimer arrays can enable SH enhancement even in the absence of the resonance in the linear reflectivity. Indeed, when the linear Wood's anomaly is excited in the $E_x \parallel p_L$ geometry, the first SHG peak appears at 48.5°, deviating from the reflectivity minimum at 50°. Furthermore, in the case of $E_x \parallel p_T$ the SH enhancement in the vicinity of $\theta = 30°$ occurs in the absence of any noticeable features in the linear reflectivity at all. The discrepancies between the linear reflectivity and the SHG thereby illustrate a striking difference between the nonlinear properties of the SPP and Wood's anomaly modes.

Sizable angular variations of the magnetic contrast ρ in SH are seen for both orientations of the sample. The characteristic magnitude of the resonant variation is around 5 % (Fig. 4.4), one-order of magnitude higher than the usual linear transverse MOKE signal generated in magneto-plasmonic thin films[3]. A drop in the angular dependence of the nonlinear magnetic contrast appears near the angle corresponding to the first SH output peak, namely 30° for $E_x \parallel p_T$ and 48.5° for $E_x \parallel p_L$.

4.3.2 Spectral analysis

Further insights in the nature and nonlinear properties of the Wood's anomalies can be obtained from the spectral measurements. To that end, we performed similar angular measurements of the linear reflectivity and magnetization-dependent SH output at various fundamental wavelengths. As a result, we observed a pronounced wavelength-dependence of the angular features in the linear reflectivity as well as SH intensity and magnetic contrast. The data for the two sample geometries are summarized in Fig. 4.5.

In Fig. 4.5a-b, the linear reflectivities were normalized to the reflectivity in the bare silicon substrate. Within the wavelength range of the $800 - 900$ nm and angles of incidence $25° - 75°$, the angle of the reflectivity minimum increases with the wavelength. The drop of reflectivity is about 7% for all wavelengths in the case of $E_x \parallel p_L$. In the $E_x \parallel p_T$ configuration, the reduced spatial periodicity $\Lambda_T = 265$ nm denies linear access to the surface modes, and thus no resonant variations of the reflectivity were registered.

A considerably richer picture can be recovered from the SH angular spectra (Fig. 4.5c-d). The dependence of SH output on the angle of incidence and wavelength in the $E_x \parallel p_T$ geometry exhibits a strong SHG peak at $\theta \approx 61.5°$, independent on the wave-

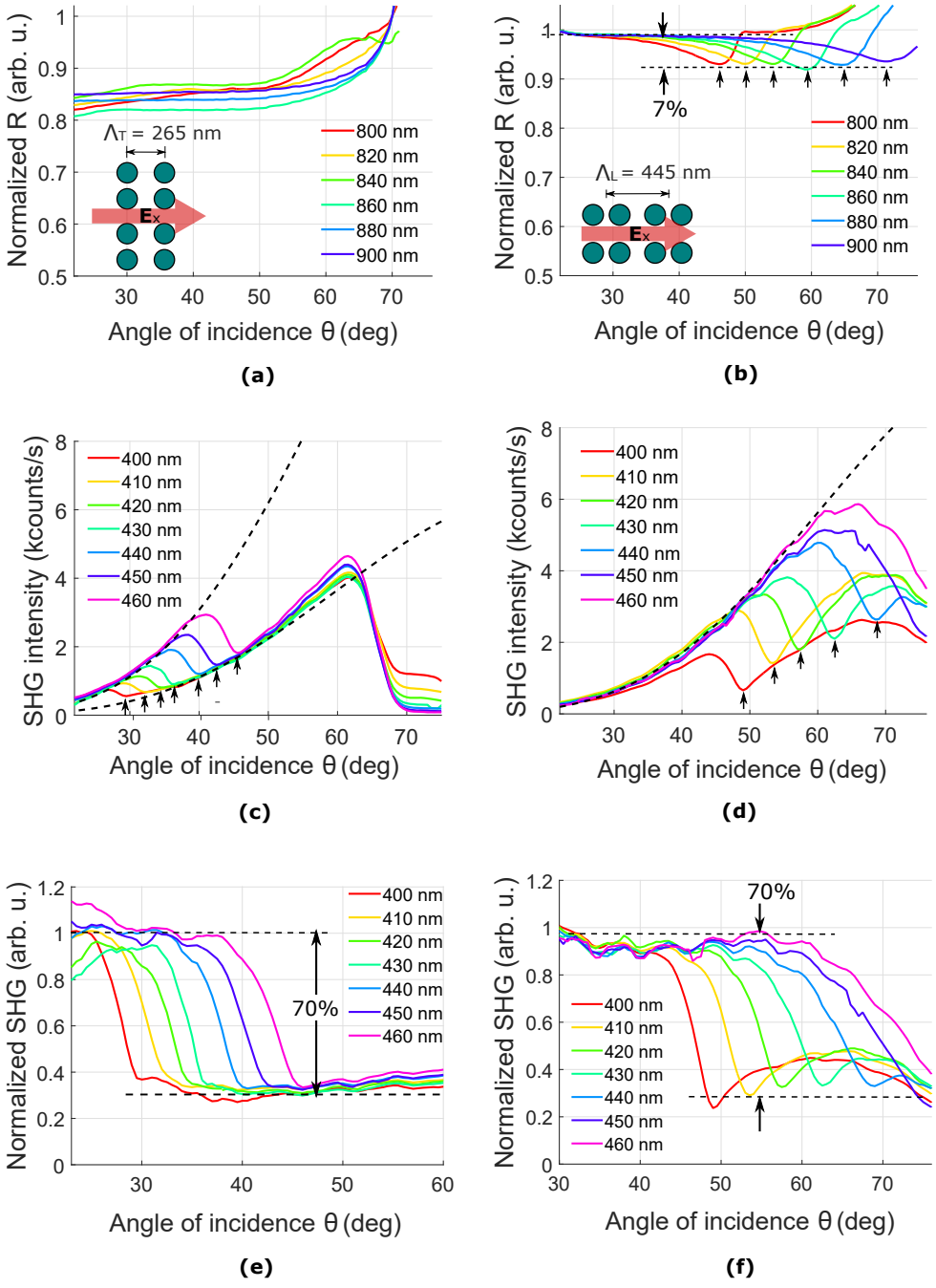

Figure 4.5 – The left column (a, c, e) shows the analysis for $E_x \parallel p_T$. The right column (b, d, f) presents the data for the case of $E_x \parallel p_L$. (a, b) Angular dependence of the linear reflectivity at different wavelengths. (c, d) Angular dependence of SHG intensity at different SHG wavelengths. The black dashed line illustrates the empirical guideline for normalization of SHG in panels e-f. Small arrows mark the SHG dips. (e, f) Normalization of SHG intensities at different wavelengths shows the distribution of SHG between different diffraction orders. The empty dots show the Wood's angles at each wavelength.

length. In contrast to that, the small-angle SH peak shifts towards larger angles of incidence for longer fundamental wavelengths. A similar dispersive shift of the SH features is observed in the other geometry ($E_x \parallel p_L$), in that case for larger angles. This dissimilar behaviour of the two geometries is again consistent with the unequal spatial periodicity along the two directions. It is worth mentioning that, in the $E_x \parallel p_L$ geometry, the LSPR can be excited, characterized with an enhancement of the electric field concentrated within the dimer gap. This LSPR excitation on the SH output can be speculated to skew the wavelength dependence at a fixed angle of incidence θ. However, as seen in Fig. 4.5d, it is difficult to disentangle the impact of LSPR from other contributions. Comparing Fig. 4.5c and d, when the LSPR is respectively disable and enable, it is unlikely that the qualitative shapes of the curves in Fig. 4.5d are strongly modified by the LSPR mode. Furthermore, the nickel content (the filling fraction of the surface) is 29%, sufficiently low so that propagating surface plasmon-polaritons cannot be efficiently excited.

The transfer of SH intensity between the nonlinear diffracted orders and the specular $m = 0$ is illustrated in Figs. 4.5e-f, where the SH outputs were normalized to an empirical model ($\propto \sin^4\theta$) for the angular dependence of SHG at the thin film surface (the black dashed lines in Fig. 4.5c-d). It shows that the nonlinear Wood's anomaly light coupling is extremely efficient. In both geometries, about 70% of the optical energy at the double frequency is dissipated at large angles of incidence for a multitude of fundamental wavelengths. Notably, the percentage of the energy pumped into the second-order $m_{nl} = -2$ in the configuration $E_x \parallel p_L$ is not consistent with the 7% drop of the reflectivity R_ω measured for the linear diffraction anomaly (see Fig. 4.5b). Thus, our results evidence the"uneven distribution of light" between SH diffraction orders, extending the Wood's picture onto the nonlinear-optical domain and demonstrating the immense capabilities and sensitivity of SH spectroscopy for these effects. It is worth noticing that the 70% drop of the SHG intensity is almost identical for the case of purely nonlinear case ($E_x \parallel p_T$ in Fig. 4.5e) and the case of mixed linear-nonlinear Wood's anomaly ($E_x \parallel p_L$ in Fig. 4.5f). Based on this observation we speculate that in the mixed case the nonlinear Wood's anomaly dominates.

4.3.3 Specifying the order of Wood's anomaly

From Eq. 4.3, one can derive:

$$\sin\theta + m_{lin}\frac{\lambda_0}{\Lambda} = n_{eff}(\omega) \tag{4.5}$$

where the wavevector of the surface mode $k_s(\omega)$ was represented as $k_s(\omega) = k_0 n_{eff}(\omega)$, with $n_{eff}(\omega)$ the effective refractive index of the mode at the fundamental frequency. $n_{eff}(\omega)$ can be understood as the weighted refractive index of the metal and the dielectric (air) at both sides of the interface, which is sampled by the evanescent field of the surface waves [22]. The nonlinear phase-matching condition in Eq. 4.4 can be rewritten as:

$$\sin\theta + \frac{m_{nl}}{2}\frac{\lambda_0}{\Lambda} = n_{eff}(2\omega) \tag{4.6}$$

From Eq. 4.5-4.6 above, the sine of the resonant angle of incidence θ is linearly proportional to the normalized fundamental wavelength λ/Λ, where the slope is the diffraction order and the offset is the effective refractive index. In Fig. 4.6, the sine of the angles, where the pronounced intensity dips in the linear reflectivity R_ω and the SHG $I_{2\omega}$ are observed at each fundamental wavelength, are marked by empty dots.

In Fig. 4.6, three groups of data can be seen. The dips in the linear reflectivity R observed in the $E_x \parallel p_L$ geometry (red diamond dots) fit with the dispersion curve of the linear Wood's anomaly with order $m_{lin} = -1$ and $n_{eff}(\omega) \approx 1.07$ (red solid line). Occurring at the same condition, the SHG minima in the $E_x \parallel p_L$ geometry (blue empty circles) correspond to the second-order nonlinear anomaly with order $m_{nl} = -2$ and $n_{eff}(2\omega) \approx 1.04$ (blue solid line). The co-excitation of the linear Wood's anomaly with order $m_{lin} = -1$ and the second-harmonic Wood's anomaly with order $m_{nl} = -2$ is the direct result of the nonlinear optical diffraction discussed in section 4.1. The small deviation in n_{eff} indicates negligibly small dispersion of the surface mode.

In the $E_x \parallel p_T$ configuration, there was no pronounced dip in the linear reflectivity, as expected for the case of $\Lambda_T < \lambda_0/2$, with the fundamental wavelength λ_0 in the range of 800-920 nm. The dips in the angular dependence of SHG (magenta empty circles) conform with the nonlinear Wood's anomaly with order $m_{nl} = -1$ and $n_{eff}(2\omega) \approx 1.01$ (green solid line). The lower $n_{eff}(2\omega)$ might come from the fact that there is almost no highly concentrated LSPR mode involved in this configuration.

Following the Eq. 4.4, it is expected that the $E_x \parallel p_L$ configuration can support another second-order nonlinear Wood's anomaly with $m_{nl} = +1$, which is plotted as the black dashed line in Fig. 4.6a. However, according to our simulation, this mode can only be excited at small angle of incidence ($\theta \leq 8°$), out of the angular range in the registered setup ($20 - 75°$).

Fig. 4.6b-c summarize the SH data in Fig. 4.5c-d into false color two-dimensional maps, where the smoothed wavelength dependence takes into account the spectral width of the fundamental radiation (on the order of $5 - 7$ nm). In both configurations, the minimum of the specular SH output (registered in the zero diffraction order) is well correlated with the calculated dispersion of the nonlinear Wood's anomalies based on Eq. 4.4 (white lines). We can recall that the drastic difference between two geometries is that linear excitation of Wood's anomaly and LSPR with the electric field enhancement in the dimer cell are together active only when $E_x \parallel p_L$. The similarity of the SH angular spectra obtained in the two orthogonal geometries with unequal linear optical properties strongly corroborates the dominant role of the nonlinear anomaly excitation.

4.3.4 Impact of Wood's anomaly on nonlinear MOKE

Having identified the modes observed in the linear and SH spectra as well as their dispersion, we now turn to the resonant magneto-optical effects in SH. The fingerprint of the Wood's anomalies on the nonlinear magneto-optical signals is shown in Fig. 4.7. There, the drop of the magnetic contrast ρ (dark area) is well correlated with the calculated dispersion of the nonlinear diffraction anomalies (white solid lines), which are $m_{nl} = -1$ for $E_x \parallel p_T$ (Fig. 4.7a) and $m_{nl} = -2$ for $E_x \parallel p_L$ (Fig. 4.7b). This behaviour is similarly observed in both configurations, regardless of the excitation of

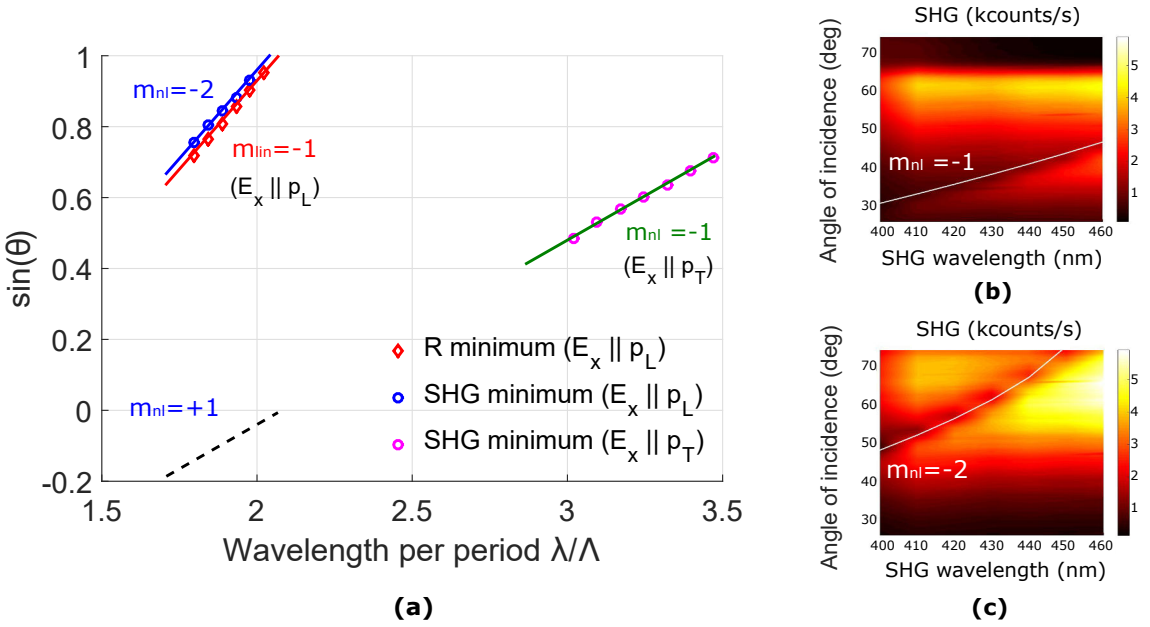

Figure 4.6 – (a) The lines show the theoretical dispersion of the Wood's anomalies excited in the two-dimensional nanoarrays. The empty dots show the sine of the angle where the angular spectrum of linear reflectivity $R(\omega)$ and average SH output $I_{2\omega}$ reach minimum in corresponding configuration. (b) In $E_x \parallel p_T$ configuration, the first-ordered nonlinear diffraction anomaly $m_{nl} = -1$ (white line) can be excited, matched with the dip (dark region) in the angular dependence of SHG. (c) In the case when $E_x \parallel p_L$, the SHG minima (dark region) fit in the nonlinear Wood's anomaly with $m_{nl} = -2$ (white line).

linear anomalies and LSPR field enhancement within the dimer. In particular, since both linear Wood's anomaly excitation and LSPR field enhancement are inactive when $E_x \parallel p_T$, the angular dependence of the SH magnetic contrast is attributed to the nonlinear Wood's anomalies.

While the linear excitation of Wood's anomaly has low or almost no impact on the nonlinear MOKE, the nonlinear mechanism for the surface mode excitation in ferromagnetic nanostructured arrays has significantly larger potential for the variations of nonlinear magneto-optical signals. Interestingly, this result is inherently consistent with our previous findings in the case of nonlinear magneto-SPP excitation in thin metal films [6, 7]. From the nonlinear-optical point of view, the similarity between the two situations is related to the strong variations of the electric field at the double frequency 2ω, as opposed to the fundamental field $E(\omega)$. The generality of this effect has a potential of becoming a very interesting and relevant question of nonlinear photonics and requires further investigation.

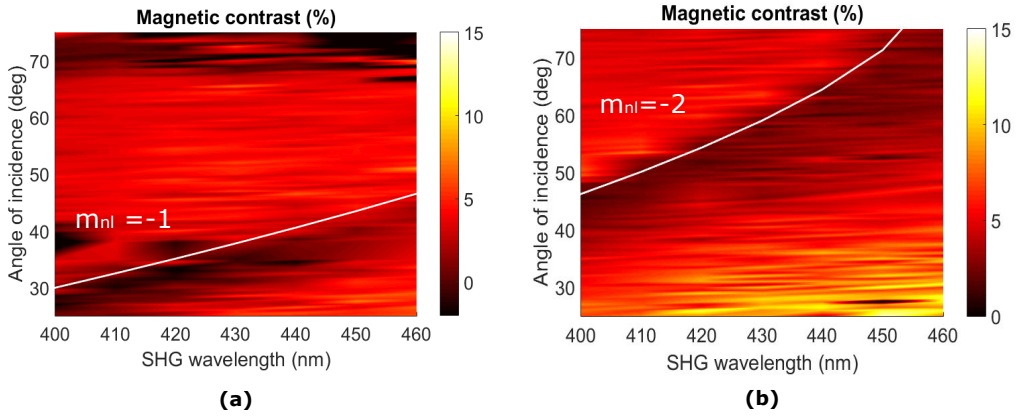

Figure 4.7 – The false-color images of the SH magnetic contrast for (a) $E_x \parallel p_T$, where the white line shows the theoretical dispersion for the second-harmonic anomaly $m_{nl} = -1$, and (b) $E_x \parallel p_L$, where the white line marks the dispersion of $m_{nl} = -2$.

4.4 Conclusion

In this chapter, the impact of Wood's anomalies on the SH output and nonlinear MOKE in the two-dimensional arrays of nickel nanodimers have been investigated. The angular spectra of the linear reflectivity and the magnetic SH intensity $I_{2\omega}(\pm M)$ were measured for a series of fundamental wavelengths in the two sample orientations. A detailed comparison of these two sets of data highlighted the relevant linear and nonlinear mechanisms of the excitation of the Wood's anomaly.

The results suggest that the linear Wood's anomaly has little influence on the SH yield. The decrease of specular SHG intensity $I_{2\omega}^{(0)}$ upon the emergence of the new $m_{nl} = -1$ or $m_{nl} = -2$ diffraction orders in the nonlinear regime is 70%, i.e. an order of magnitude larger than 7% reflectivity variations in its linear counterpart. The SHG magnetic contrast also shows a fingerprint of the nonlinear diffraction anomaly, which

is the main factor contributing to the $\sim 5\%$ angular variation of the SHG magnetic contrast ρ around the Wood's anomaly. Nonlinear magneto-optical effects can thus be utilized as a measure of the efficiency of diffraction gratings in periodic arrays of magnetic nanoparticles.

In the investigated array of nickel nanodimers, the large difference in the lattice period between transversal and longitudinal configurations determines the character of Wood's anomalies. In future, possible contributions of LSPRs in nanodimers resulting in the excitation of SLRs upon interference with Wood's anomalies might be identified in similar experiments using structures with identical longitudinal and transverse lattice periods. In general, depending on the grating constant, one can excite the diffraction anomalies in the fundamental and (second-order, third-order, etc.) nonlinear regimes, which emerge either in the air or substrate interface. This property allows to select the preferred diffraction order and combine it with the optical meta-surfaces by geometrical design.

Chapter 5

Femtosecond time-resolved nonlinear magneto-plasmonic cross-correlation measurements

Chapter 3 and 4 describe the coupling of the magnetization-induced second-harmonic generation (mSHG) with the nonlinear surface waves in the static regime, which is the integration over time of the phenomenon. In this chapter, the dynamics of the nonlinear magneto-plasmonics will be explored. The field enhancement of SPP makes it a sensitive probe for the ultrafast phenomena occurring within the optical skin depth of metallic surfaces[112, 118, 119]. The temporal evolution of the SPP field can be recorded by interferometry[120, 121]. Taking advantage of the SPP propagation length along the metallic interface, the plasmonic interferometry can be performed directly on the metallic surface [30, 113], and is proved to be magnetization-sensitive when a magnetic layer is introduced within the field skin depth[12, 110]. In this work, the auto-correlation and cross-correlation of the mSHG pulse are performed on the Kretschmann geometry, where the SPPs can be coupled in both the linear and the nonlinear regimes.

5.1 Fluence dependence of the mSHG

The first section is devoted to the experimental observations of the fluence dependence of the nonlinear magneto-plasmonics on Kretschmann geometry. The setup is the same as in Fig. 3.3 in the chapter 3, the only variable is the average power of the radiation coming from a femtosecond laser source (centered wavelength 1560 nm, pulse duration sub-120 fs, repitition rate 80 MHz). The incident power is tuned by a set consisting of a half-wave plate and an analyzer. Fig. 5.1 shows the angular dependence of the mSHG intensity and the magnetic contrast for the bilayer of (20nm)Au/ (35nm)Co (Fig. 5.1a) and the trilayer of (5nm)Au/ (10nm)Co/ (15nm)Ag (Fig. 5.1b) using the p-polarized fundamental excitation at wavelength 1560 nm. When the power of the incident light increases, remaining below the damage threshold of the sample, the intensity of the mSHG increases quadratically with the pump power, as illustrated in

Fig. 3.5. However, it has been observed that the nonlinear magnetic contrast ρ, defined in Eq. 2.50, reduces gradually as the pump power increases. For the sample of (20nm)Au/ (35nm)Co bilayer deposited on sapphire, the reduction of the SH magnetic contrast occurs not only at the angles where linear and nonlinear SPPs are excited but also at off-resonant angles. In contrast, for the trilayer of (5nm)Au/ (10nm)Co/ (15nm)Ag deposited on fused-silica substrate, the reduction of the SH magnetic contrast is only observable around the angle of 46.6°, where the nonlinear coupled SPP(2ω) takes effects (refer to the section 3.6).

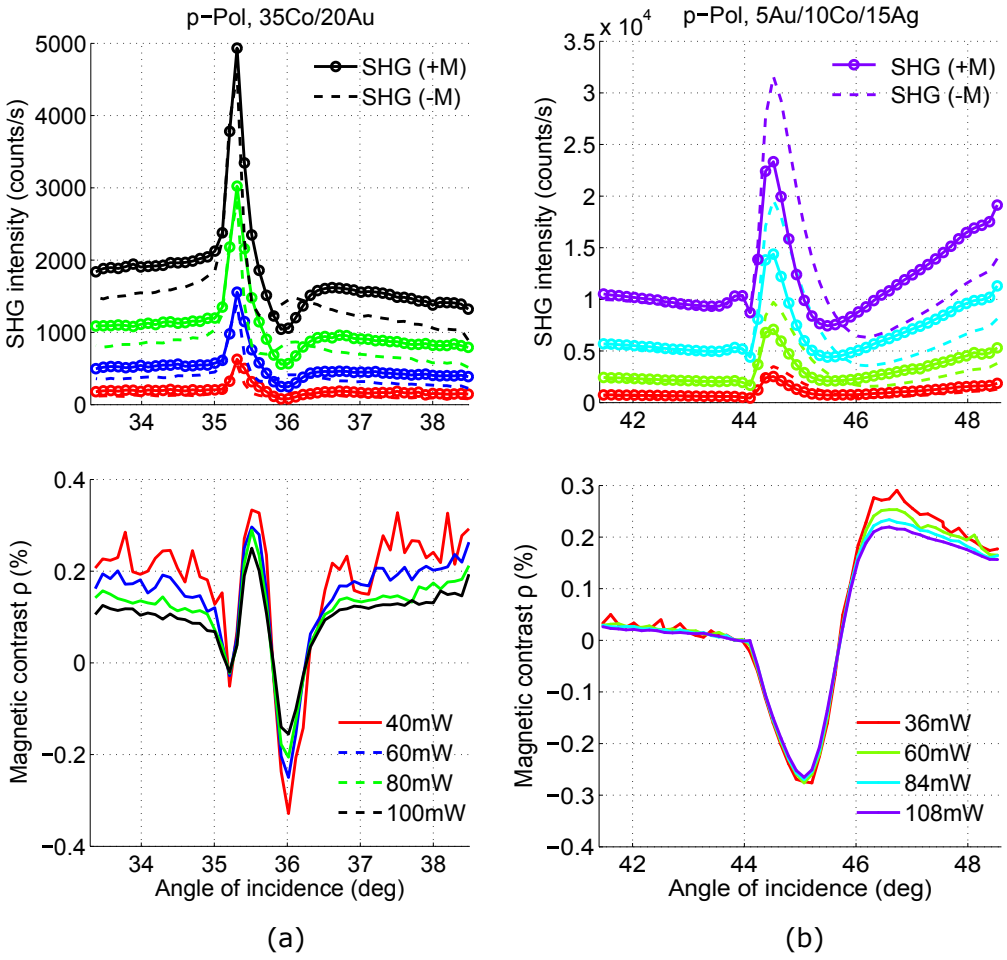

Figure 5.1 – The angular dependence of the mSHG intensity and the SH magnetic contrast ρ in (a) the bilayer (20 nm)Au/ (35 nm)Co/ sapphire and (b) the trilayer (5 nm)Au/ (10 nm)Co/ (15 nm)Ag/ fused-silica at different pump powers, represented by different colors. The fundamental wavelength in both cases is 1560 nm. In the top row, the dotted lines illustrate the SHG(+M) while the dashed lines are used for SHG(-M).

This phenomenon implies that the generated SH field depends on the temperature of the sample. Since the SH field is the interference of the non-magnetic and magnetic

SH fields as in Eq. 2.49, it can be written as:

$$E_{2\omega}(\pm M) = \boldsymbol{E}_{2\omega}^{nm} \pm \boldsymbol{E}_{2\omega}^{mag} \propto \left(\chi_{nm}^{(2)} \pm \chi_{mag}^{(2)} M\right) \boldsymbol{E}_{\omega} \boldsymbol{E}_{\omega}$$

where $\chi_{nm}^{(2)}$ and $\chi_{mag}^{(2)}$ are the non-magnetic (even) and the magnetic (odd) SH nonlinear susceptibilities, respectivily. One considers $\chi_{mag}^{(2)}(M) = \chi_{mag}^{(2)} M$ at the first-order (linear) approximation. From this formulation, the thermal dependence of the mSHG might come from the SH susceptibility[1] $\chi^{(2)}$, the magnetization M or the fundamental field E_{ω}.

Keeping in mind the relaxation dynamics of laser-excited electrons in metallic multilayers [31, 113], the optical properties of the structure can be influenced by a high power optical pulse below the damage threshold. Hot electrons, which acquired high energies above the Fermi-level by absorbing photons from a strong pump pulse, transfer heat by electron-electron thermalization and electron-phonon scattering [122–124]. The thermal equilibrium established a few picoseconds after the laser pump [113] might cause the temperature dependence of the effective dielectric function ϵ_{eff}. In order to see whether the effective dielectric function ϵ_{eff} of the metallic structure depends on temperature, the fluence dependence of the linear reflectivity is verified. Fig. 5.2 shows the angular dependence of the linear reflectivity in (a) the bilayer of (20 nm)Au/ (35 nm)Co and (b) the trilayer of (5 nm)Au/ (10 nm)Co/ (15 nm)Ag at different optical powers. Even though there is slight change in the scale of the linear reflectivity, the angular position and angular broadening of the peak do not seem to depend on the incident power. Thus, one can conclude that the linear dielectric function ϵ_{eff} does not vary significantly within the limit of registered setup.

The temperature dependence of the optical properties in the nonlinear regime can be verified by the fluence dependence. If the second-order nonlinear susceptibilities $\chi^{(2)}$ were sensitive to temperature, the far-field SHG intensity

$$I_{2\omega} \propto |E_{2\omega}|^2 \propto |\chi^{(2)} E_{\omega} E_{\omega}|^2$$

would be no longer proportional to the squared intensity of the fundamental light I_{ω}^2. Here, the quadratic dependency at a constant magnetization, like in Fig. 3.5, is preserved at all angles of incidence for both the bilayer Au/Co and the trilayer Au/Co/Ag. Similar to ϵ_{eff}, the pump power within our measurement range does not seem to have significant effects to the nonlinear susceptibility $\chi^{(2)}$ in the near-infrared spectral range. Even when the strength of the electric field is high, i.e. at the angles of incidence where the linear SPP(ω) and nonlinear SPP(2ω) are excited, the scaling $I_{2\omega} \propto I_{\omega}^2$ holds.

Ruling out all other factors, the dependence of the magnetic contrast ρ on the pump power seems to be the result of thermal demagnetization $M(T)$. Apparently, there are two noteworthy effects that can cause demagnetization: (i) an increase of the average temperature or heat accumulation caused by absorption of multiple pump pulses during the time of open chopper and (ii) ultrafast demagnetization [125–127] induced by

[1] here the general notation of $\chi^{(2)}$ can be understood as either the magnetic or the non-magnetic susceptibily.

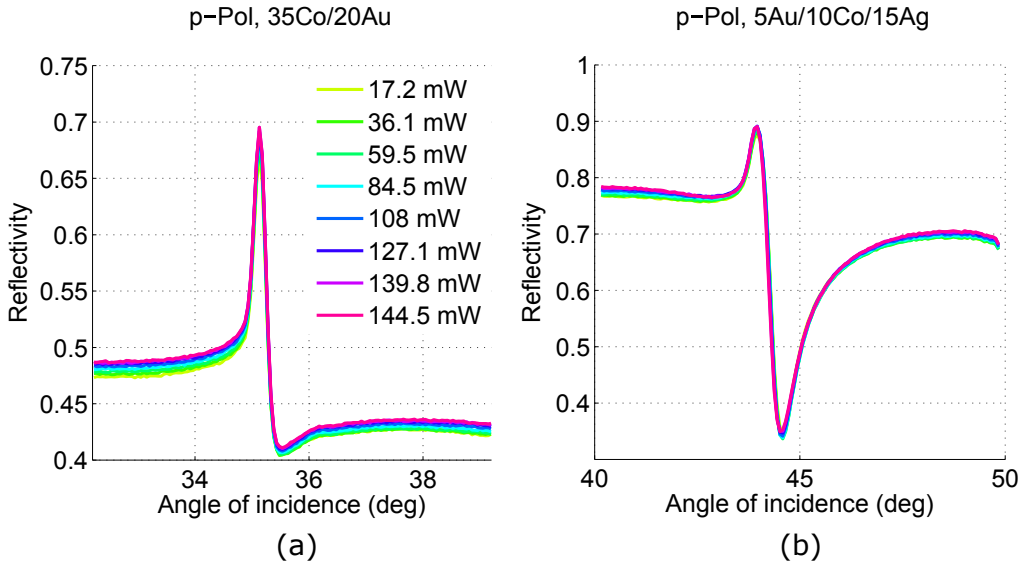

Figure 5.2 – The angular dependence of the linear reflectivity in (a) the sample (20 nm)Au/ (35 nm)Co/ sapphire and (b) the sample of (5 nm)Au/ (10 nm)Co/ (15 nm)Ag/ fused-silica at different pump powers, represented by different colors. The excitation is centered at wavelength 1560 nm and p-polarized.

single pulse where the first half of the pulse changes the conditions for magnetic SHG generated by its second half. The heat accumulation, which should scale linearly with the number of pulses transmitted by the mechanical chopper during its opening time, can be reduced by increasing the chopper frequency. Variation of the chopping rate[2] up to 4.45 kHz (see specifications in AppendixA) does not seem to reduce the thermal effect on the SH magnetic contrast suggesting that heat accumulation is not the primary reason for demagnetization. The reason why the SH magnetic contrast ρ in the trilayer Au/Co/Ag reduces exclusively when the nonlinear SPP(2ω) is excited can not be explained either. One would envisage pump-probe experiments in Kretschmann configuration to clarify the role of SPP-excitation on the dynamics of magnetization.

5.2 Magneto-plasmonic auto-correlation

Sub-picosecond pulses cannot be measured by high speed photo detectors because their rise and fall time, in picosecond to nanosecond scale, is still longer than the pulse duration. Thus the ultrashort pulse is used to gate itself in the auto-correlation and cross-correlation measurements, where the information of the pulse can be obtained [128]. The nonlinear optical effects are employed in the intensity auto-correlation and cross-correlation because they are instantaneous phenomena, which occur exclusively upon the temporal overlap of the fundamental pulses. Both the nonlinear auto-correlation in this section and the spectrally-resolved cross-correlation in the next section were performed in corporation with LS Leitenstorfer at University of Konstanz, where the

[2]considering that the heating of sample is linear with time.

ultrashort sub-10 fs laser, center wavelength 1200 nm (bandwidth ≈400 nm) with repetition rate 40 MHz was employed.

All the measurements in this part were performed on the trilayer of (5 nm)Au/ (5 nm)Co/ (15 nm)Ag deposited directly on UV fused-silica prism, prepared by Dr. Denys Makarov (HZDR, Dresden). This sample exhibits the largest mSHG intensity and magnetic contrast, based on the discussion on the trilayers in chapter 3. The purpose of direct deposition is to avoid the parasitic thermal effect coming from the heating of phase-matching liquid, which has been used for sample attachment. Compared to those deposited on flat substrate, the sample exhibits stronger SHG signal and sharper angular dependence.

5.2.1 Magneto-plasmonics auto-correlation setup

The objective of the magnetically-controlled autocorrelation performed in Kretschmann geometry is to observe the influence of propagaring SPPs on the mSHG pulse. The linear reflectivity at ω is measured by an integrating sphere (made of GaAs for infrared wavelength and Si for visible wavelength). The SHG is detected using PMT (Hamamatsu R955) coupled with a High Frequency Lock-in Amplifier (Zurich Instruments) working at 40 MHz, the repetition rate of the laser, which permits to reduce the $1/f$-noise. Unlike the photon counting regime described in chapter 3, this detection scheme can keep away the signal from cosmic rays due to much higher statistics, but is vulnerable to electronic noise.

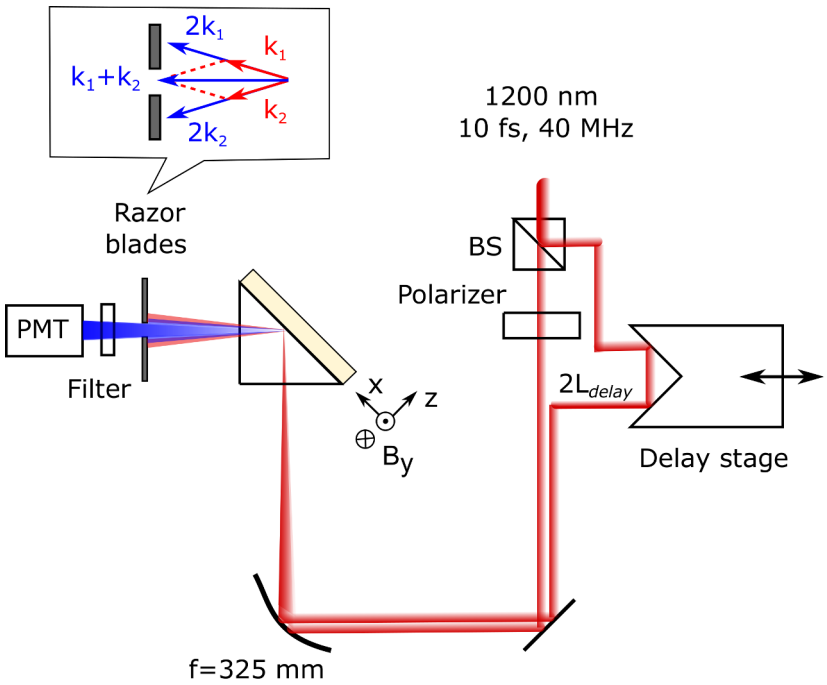

Figure 5.3 – A simplified schema for the setup of the magneto-plasmonic auto-correlation. The inset shows the wavevectors of incident beams and the SH emitted beam.

Fig. 5.3 illustrates the intensity auto-correlation of the mSHG performed in Kretschmann configuration. The external magnetic field is perpendicular to the plane of incidence as in the transverse MOKE geometry. The magnetic field strength is around 200 mT at the focused spot on the sample, enough to saturate the in-plane magnetization of cobalt thin film. The p-polarized fundamental fs beam is splitted into two pulse trains, denoted as $E_\omega(t-\tau)$ and $E_\omega(t)$. The time delay $\tau = 2L_{delay}/c$ between two pulses is adjusted by a retro-reflector mounted on a linear translation stage. It depends on the travelling distance $2L_{delay}$ of the delay stage and the speed of light c. In this setup, τ is varied in the range from -25 fs to +25 fs, with an increment of 1 fs. The two beams are directed to a spherical mirror (focal length f=325 mm), symmetric to the plane of incidence with vertical beam separation of approximately 2 mm. They are focused on the same spot on the sample surface. Small beam separation, hence small solid angle, ensures a large k_x (and very small k_z) wave vector component for SPP excitation.

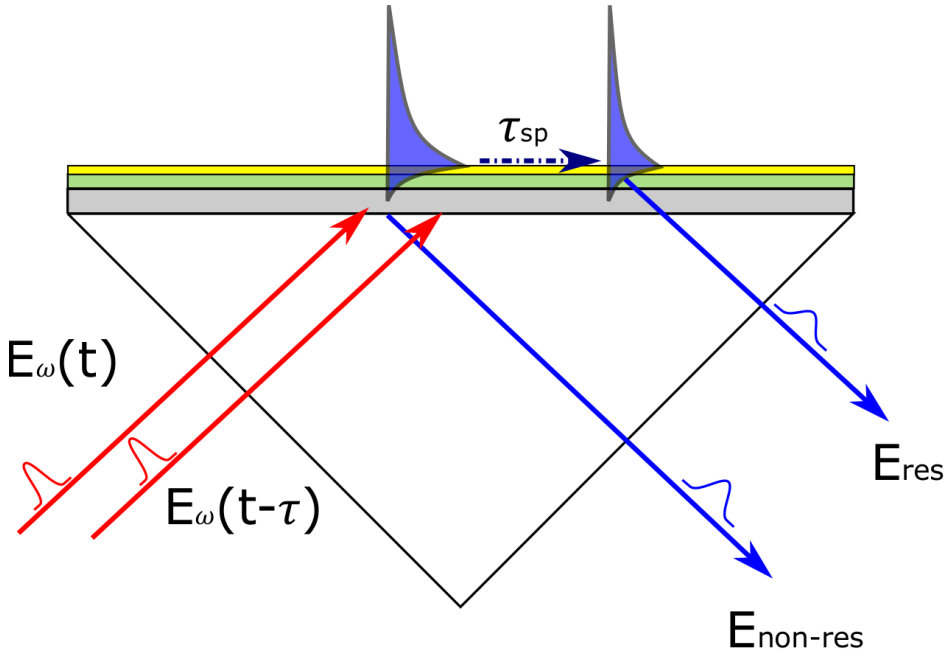

Figure 5.4 – In the Kretschmann configuration, two fundmental pulses, delayed by time τ, generate cross-product SH field $E_\omega(t)E_\omega(t-\tau)$ at bottom and top interfaces of the multilayer. $E_{non-res}$ is the SH field at the bottom interface. E_{res} refers to the coupling of SH polarization at the top interface and the radiative SPP(2ω). The propagation of SPP along the metal/air interface cause the delayed arrival of the resonant pulse.

The conventional intensity auto-correlation usually considers a single source of SHG, such as a thin BBO crystal. In Kretschmann configuration, one has to consider the non-resonant SH field generated in the bottom interface and the radiative SPP at the double-frequency coming from the upper interface, as discussed in chapter 3. Here the auto-correlation measurement has been performed in the non-collinear fashion, different momentum-matching conditions are valid for the generation of SH fields, such as $2k_1(\omega) = k_1(2\omega)$, $2k_2(\omega) = k_2(2\omega)$ and $k_1(\omega) + k_2(\omega) = k(2\omega)$, where k_1 and k_2 refer to the wavevectors of two incident beams. The SH fields generated

by different paths are separated in space, as shown by the inset in Fig. 5.3. Using the aperture made of a pair of razor blades, fundamental pulses at frequency ω and any SH signals created by individual input beams (both non-resonant and resonant SH fields) are blocked. Only the SH fields generated by two incident pulses, corresponding to the phase-matching condition $k_1(\omega) + k_2(\omega) = k(2\omega)$, are retained. In quantum-optical picture, it means that a SH photon is emitted upon the annihilation of two fundamental photons coming from two different pulses. The cross-product SH fields $E_{2\omega}(t,\tau) \propto \chi^{(2)} E_\omega(t-\tau) E_\omega(t)$ can be generated both at the bottom and top interfaces of metallic multilayer. The SH field at the bottom interface, $E_{non-res}$, does not interact with the SPP field at the metal/air interface because the distance to the open surface is larger than the field skin depth. In contrast, E_{res} is the result of the SH polarization in the upper interface coupled to the nonlinear SPP at 2ω, as proven in chapter 3. The time it takes for the radiative SPP pulse to propagate along the metallic surface is arbitrary $\tau_{sp} = L_{sp}/c$[3]. Besides that, there is a phase difference between $E_{non-res}$ and E_{res} due to the difference in the optical path lengths inside the prism, which is $L_{sp}/\sqrt{2}$ for an angle of incidence $\approx 45°$.

Non-resonant $E_{non-res}$ and SPP-resonant E_{res} SH fields along x read:

$$\begin{aligned} E_{non-res}(t,\tau) &\propto E_\omega(t) E_\omega(t-\tau) \exp\left(i2k_x x - i2\omega t\right) \\ E_{res}(t,\tau) &\propto E_\omega(t) E_\omega(t-\tau) \exp\left[ik_{sp}\Big(x - \frac{L_{sp}}{\sqrt{2}}\Big) - i2\omega(t+\tau_{sp}) - \frac{t}{\tau_{sp}}\right]. \end{aligned} \tag{5.1}$$

We note that $2k_x(\omega) = k_{sp}(2\omega)$ due to the nonlinear phase matching condition in Eq. 3.6, and $\exp -t/\tau_{sp}$ represents for the decay of the SPP field along x during the time τ_{sp}. The total SH intensity is the interference of these two fields, as defined in Eq. 3.11. Thus one obtains

$$\begin{aligned} I_{2\omega}(t,\tau) &= |E_{non-res}(t,\tau) + LE_{res}(t,\tau)|^2 \\ &= |E_{non-res}(t,\tau)|^2 + |LE_{res}(t,\tau)|^2 + LE_{non-res}(t,\tau) E_{res}(t,\tau) \cos\varphi_{nr,res}\,, \end{aligned} \tag{5.2}$$

where $\varphi_{nr,res}$ is the phase difference between the non-resonant $E_{non-res}$ and resonant LE_{res} SH fields. Recall that L is the normalized Lorentzian function defined in chapter 3, which depends on the angle of incidence. Referring to Eq. 3.8, $L = 1$ at the angle θ_0 where SPP(2ω) is excited by the nonlinear mechanism. Deviated from this angle, L decays within a certain angular width Γ decaying to zero at non-resonant angles.

In the vicinity of the resonant angle of SPP(2ω) and $L \neq 0$, the signal collected by

[3]Considering that the group velocity of SPP is close to its phase velocity c.

the detector (PMT in this case) is the time integral of $I_{2\omega}(t,\tau)$

$$\begin{aligned} S_{2\omega}(\tau) &= \int_{-\infty}^{+\infty} I_{2\omega}(t,\tau)dt \\ &= \int_{-\infty}^{+\infty} |E_{non-res}(t,\tau)|^2 dt \\ &+ \int_{-\infty}^{+\infty} |LE_{res}(t,\tau)|^2 dt \\ &+ \int_{-\infty}^{+\infty} LE_{non-res}(t,\tau)E_{res}(t,\tau)\cos\varphi_{nr,res}dt \\ &= S_{non-res}(\tau) + S_{res}(\tau) + S_{mix}(\tau) \end{aligned} \tag{5.3}$$

In this equation, the non-resonant part is

$$\begin{aligned} S_{non-res}(\tau) &= \int_{-\infty}^{+\infty} |E_{non-res}(t,\tau)|^2 dt \\ &= \int_{-\infty}^{+\infty} |E_{\omega}(t)E_{\omega}(t-\tau)|^2 dt \\ &= \int_{-\infty}^{+\infty} I_{\omega}(t)I_{\omega}(t-\tau)dt \end{aligned} \tag{5.4}$$

$S_{non-res}(\tau)$ is the same as the intensity auto-correlation function obtained in case of a single SH source.

The resonant intensity is

$$\begin{aligned} S_{res}(\tau) &= \int_{-\infty}^{+\infty} |LE_{res}(t,\tau)|^2 dt \\ &= \int_{-\infty}^{+\infty} \left| LE_{\omega}(t)E_{\omega}(t-\tau)\exp\left[ik_{sp}\Big(x-\frac{L_{sp}}{\sqrt{2}}\Big) - i2\omega(t+\tau_{sp}) - \frac{t}{\tau_{sp}}\right]\right|^2 dt \end{aligned} \tag{5.5}$$

The last term

$$S_{mix}(\tau) = \int_{-\infty}^{+\infty} LE_{non-res}(t,\tau)E_{res}(t,\tau)\cos\varphi_{nr,res}dt$$

is equivalent to the spectrum of SH field in the SH interferogram. At the angles of incidence where SPP(2ω) is not excited, i.e. $L = 0$, $S_{res}(\tau)$ and S_{mix} in Eq. 5.2 vanish, leaving only the non-resonant SH signal $S_{non-res}(\tau)$.

As an external magnetic field is present in the system, the SH fields generated from the magnetic (odd) $\chi^{(2)}$ components are sensitive to the reversal of the magnetization. As E_{res} originates from the upper interface, and the ferromagnetic cobalt layer is buried within the SPP field skin depth, it is expected that the magnetic properties primarily modify the E_{res}. Furthermore, LE_{res} is responsible for the angular dependence of the SH magnetic contrast ρ, according to the discussion in chapter 3. The magnetization-induced components in $E_{non-res}$, if the evanescent field can leak through the bottom silver film to reach the cobalt layer, would have a rather small effect on the magnetic contrast.

5.2.2 Results and discussion

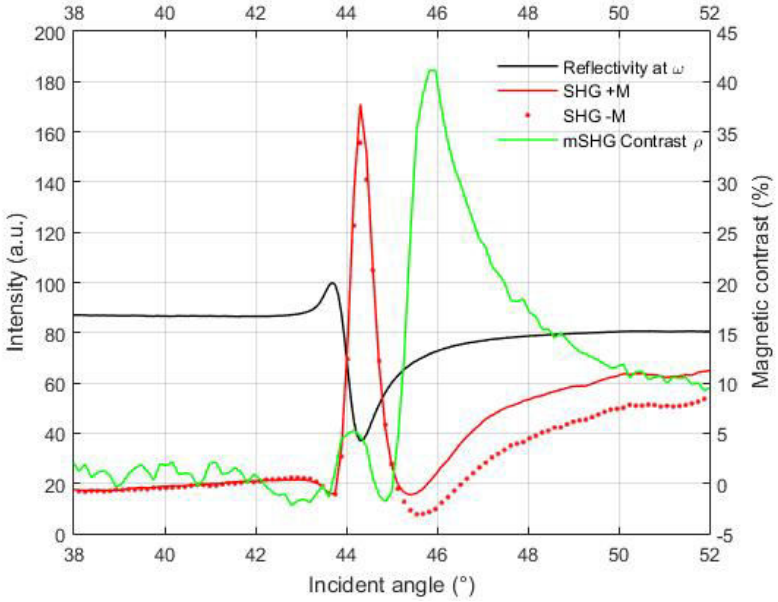

Figure 5.5 – The time-integrated (static) measurements of the linear reflectivity (black solid line), the mSHG outputs at different magnetizations (red solid line and dotted line) and the corresponding SH magnetic contrast (green solid line) in the Kretschmann geometry for the trilayer (5 nm)Au/ (10 nm)Co/ (15 nm)Ag deposited directly on a fused-silica prism.

The angular dependence of the linear reflectivity at the fundamental wavelength, mSHG($\pm M$) and the magnetic contrast of the sample (5 nm)Au/ (10 nm)Co/ (15 nm)Ag are shown in Fig. 5.5. The dip of the linear reflectivity at ω (black solid line) corresponds to the peaks of the mSHG intensities (red solid line and dotted line) at the angle 44.3°, signifying the excitation of the linear SPP(ω) by the p-polarized incident beams. The magnetic contrast (green solid line) is not in the form of the real part of a Lorentzian function as in chapter 3. However, based on the reverse approach, one can estimate that the SPP(2ω) is coupled by the nonlinear mechanism at around 46°.

Fig. 5.6a shows the magnetization-dependent auto-correlation in the same sample at four different angles of incidence: 34.7°, 44.3°, 46° and 55.3°. Besides the important angles 44.3° and 46° mentioned above, the two others are off-resonance angles, where no modes of SPPs are involved. Fig.5.6a shows that the intensity auto-correlation at angle 44.3° is the highest, while that at angle 46° is the smallest, in agreement with the peak and dip of the mSHG output in the time-integrated regime (red curves in Fig. 5.5). One can also see that the pulse has little dependence on the magnetization M, except at angle 46°, where the SH magnetic contrast is maximized and the nonlinear coupling to the SPP(2ω) is dominant. Fig.5.6b normalizes the intensity auto-correlation to unity for the same magnetization.

At the angles where the radiative SPP(2ω) is not coupled, such as 34.7°, 44.3° and 55.3°, the Lorentzian $L = 0$ and $S_{non-res}(\tau)$ is the only remaining signal in Eq. 5.3. The

auto-correlation functions at these angles have the Gaussian shape with FWHM≈10 fs. It corresponds to a Gaussian pulse with the pulse duration of ≈7 fs[4], as expected with the incident optical pulse. It is noteworthy that at angle 44.3°, where the linear SPP(ω) is excited, the auto-correlation intensity is very high due to the SPP-enhancement of the fundamental fields, $E_\omega(t)$ and $E_\omega(t-\tau)$. However, there is no obvious influence of the linear SPP(ω) to the shape of the auto-correlation function.

In contrast, the auto-correlation at the angle 46° has different shape from those at the other angles, with two supplementary wings symmetric at both side of the main Gaussian function. The smaller Gaussian functions are separated from the main function by a fixed time, thus both the non-resonant $S_{non-res}(\tau)$ and the $S_{res}(\tau)$ related to the radiative SPP(2ω) are present in this auto-correlation[5]. The interference of the two SH fields in $S_{mix}(\tau)$ should be present in the auto-correlation function when $L \neq 0$. However, from the time-integrated measurement in Fig. 5.5, there is dip of the SH intensity near angle 46°, meaning that the $E_{non-res}$ and E_{res} interfere destructively around this angle. Apparently, the phase $\cos\varphi_{nr,res} \approx 0$, and the effect of $S_{mix}(\tau)$ to the auto-correlation at angle 46° is unnoticeable.

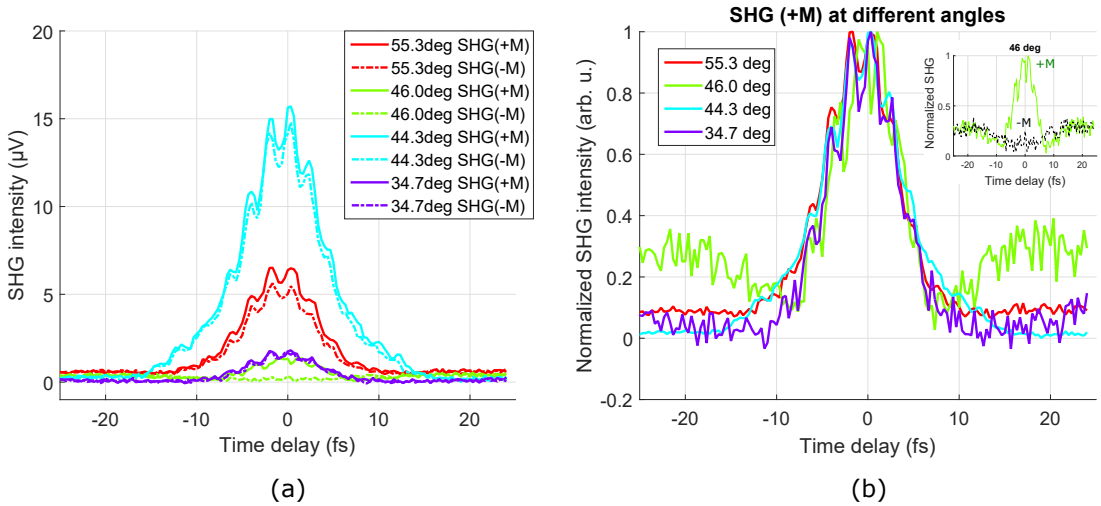

Figure 5.6 – (a) Intensity auto-correlation in the layer (5 nm)Au/ (10 nm)Co/ (15 nm)Ag employing the Kretschmann configuration. Each color represents for a different angle of incidence. The solid and dashed lines are the signals for $+M$ and $-M$, respectively. (b) The intensity auto-correlation of the SHG (+M) pulses at different angles of incidence are normalized to unity. The inset shows the normalized intensity at angle 46° for opposite magnetizations.

From the auto-correlation function at opposite magnetization, the τ-dependent SH magnetic contrast ρ can be calculated based on Eq. 2.50, and shown in Fig. 5.7a. The contrast ρ becomes strong exclusively at angle 46° where the SPP(2ω) is excited by

[4]For a sech^2 pulse, the relation between the width of the intensity auto-correlation $\Delta\tau_A$ and the pulse duration $\Delta\tau_p$ is $\Delta\tau_A = 1.54\Delta\tau_p$. For a Gaussian pulse, the ratio is $\sqrt{2}$.

[5]The signals are symmetric about the zero delay time due to the temporal symmetry of the auto-correlation $S(\tau) = S(-\tau)$.

the nonlinear mechanism, and is suppressed at other angles. This observation agrees with the expectation in the previous section that the SH magnetic properties are attributed to the radiative nonlinear SPP E_{res}, which is generated at the upper interface. At non-resonant angles, such as 44.3° and 55.3°, $S_{non-res}(\tau)$ does not carry the magnetic information, causing zero magnetic contrast as shown in Fig. 5.7a. At angle 46°, the presence of the magnetization-dependent $S_{res}(\tau, \pm M)$ (and possibly $S_{mix}(\tau, \pm M)$) causes a large SH magnetic contrast exceeding 70% on sub-10 fs timescales. Normalized intensity autocorrelation at angle 46° (inset of Fig. 5.6b) reveals that the the supplementary wings remain unchanged regardless of the magnetization M, but the central Gaussian function around $\tau = 0$ extinguished completely when the magnetization is reversed. To be able to understand the effect, it would be better to enlarge the auto-correlation time window, which is unfortunately unattainable in the registered setup.

However, it is clear that the giant nonlinear contrast, $\rho(\tau) > 70\%$, observed at angle 46° on short timescales is suppressed by approximately a factor of 2 in the time-integrated measurements, $\rho \approx 40\%$ in Fig. 5.5. Such behavior points to the coherent nature of the mSHG signal and, possibly, to the detrimental role the electron-phonon scattering plays in reducing the observable magnetic contrast in the time-integrated measurements. At different time delays, the angular dependence of the SH magnetic contrast resembles the shape at the time-integrated measurement, as seen in Fig. 5.7b. The maximal contrast is achieved when the two beams overlaps temporally, $\tau = 0$. It again confirms the dynamics of the SH magnetic contrast ρ and the magnetization-dependent radiative SPP $E_{res}(\pm M)$ excited by the nonlinear mechanism.

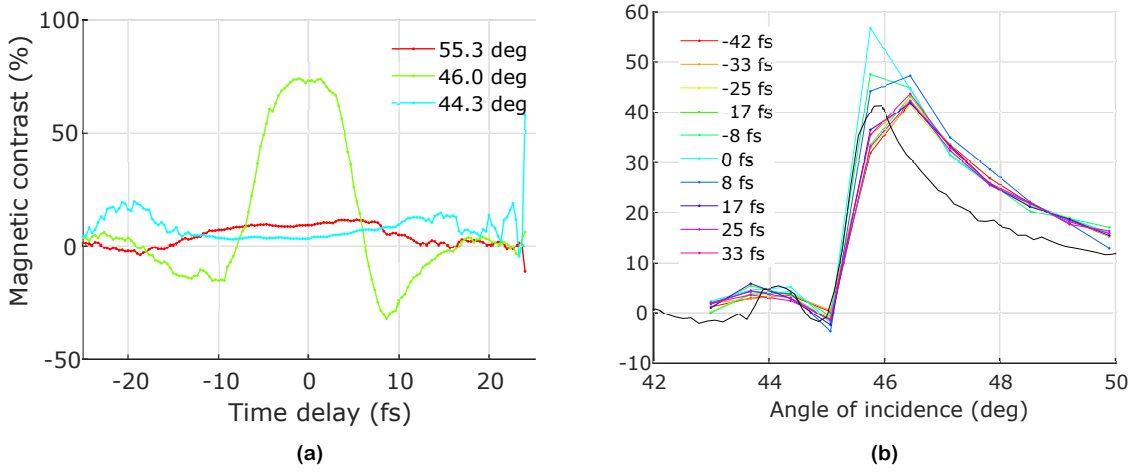

Figure 5.7 – Time-resolved second-harmonic magnetic contrast ρ of the trilayer (5 nm)Au/ (10 nm)Co/ (15 nm)Ag.

5.3 Magneto-plasmonic cross-correlation

5.3.1 Magneto-plasmonic cross-correlation setup

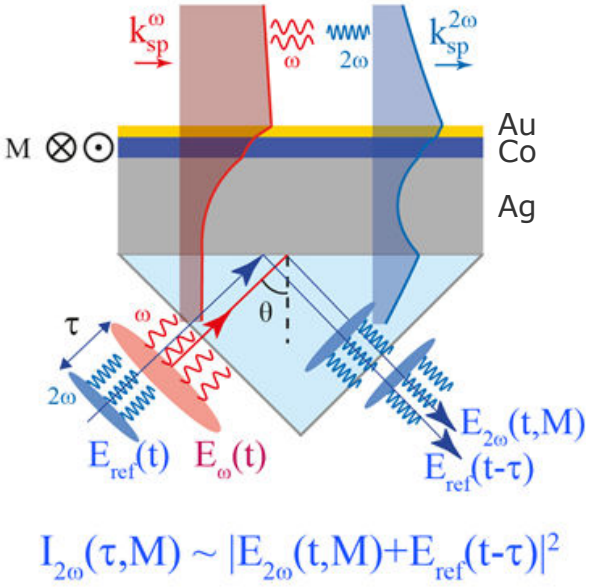

Figure 5.8 – The mSHG cross-correlation on the Kretschmann configuration.

The idea of a mSHG cross-correlation is sketched in Fig. 5.8. A pump at fundamental frequency $E_\omega(t)$ and a reference signal, so-called local oscillator, $E_{2\omega}(t-\tau)$ delayed by a time τ, are focused on the sample in a co-linear geometry. The external magnetic field is perpendicular to the plane of incidence as in the tranversal MOKE configuration. A magnetization-dependent SH field $E(2\omega, t, M) \propto \chi^{(2)} E_\omega(t) E_\omega(t)$ is generated in the Kretschmann trilayer structure (5 nm)Au/(10 nm)Co/(15 nm)Ag. To check for possible spectral phase of the emitted mSHG signals from this structure, the spectrally-resolved cross-correlation measurements were performed. Toward this end, the mSHG signal $E_{2\omega}(t, M)$ was linearly mixed with the reference field $E_{ref}(t-\tau)$

$$\begin{aligned} I_{2\omega}(\tau, \pm M) &\propto |E_{2\omega}(t, \pm M) + E_{ref}(t-\tau)|^2 \\ &\propto |E_{2\omega}(t, \pm M)|^2 + |E_{ref}(t-\tau)|^2 \\ &+ 2E_{2\omega}(t, \pm M) E_{ref}(t-\tau) \cos\varphi_{\pm M} \end{aligned} \tag{5.6}$$

Comparing the phase $\varphi_{\pm M}$ when the magnetization M is reversed, one expects to recover the phase difference $\varphi = \varphi_{+M} - \varphi_{-M}$ between the magnetic and the non-magnetic SH fields, illustrated in the phasor diagram in Fig. 3.11 (chapter 3).

A simplified setup for the experiment is shown in Fig. 5.9. Same as the previous experiment of auto-correlation, the fundamental spectrum is centered at 1200 nm, with FWHM=275 nm. The local oscillator, generated by a Beta barium borate (BBO) crystal, has the wavelength centered at 600 nm, with FWHM=70 nm. The broad spectral

range of the fundamental and the reference pulses (see AppendixA) are necessary for the spectral-resolved measurements. After the polarizing beam splitter, the fundamental beam goes through a chopper and then a delay stage for delay time τ. Meanwhile the reference beam goes through a polarizer, then reflects several times through the two parallel mirrors (the chirp compensator) before joining the fundamental beam after upon reflection on the glass plate. The two beams are focused on the thin film in the Kretschmann geometry using a spherical mirror (f=325 mm). The reference beams co-propagates through the sample structure ensuring robustness of the phase-resolved measurement. The dispersion of the reference beam (blue beam) in the fused-silica prism is pre-compensated by the chirp compensator. The experiment is carried out at the angle of incidence 46.4°, where the SH magnetic contrast is highest. After the prism, a low-pass filter is used to collect the SH signal. Both the mSHG output and the reference field are p-polarized. Linear interference of the mSHG signal and the reference wave is spectrally resolved via a grating-based spectrometer equipped with a fast CCD camera. Amplitude modulation of the fundamental wave allows for the high sensitivity measurement of the differential spectra $\Delta T/T$.

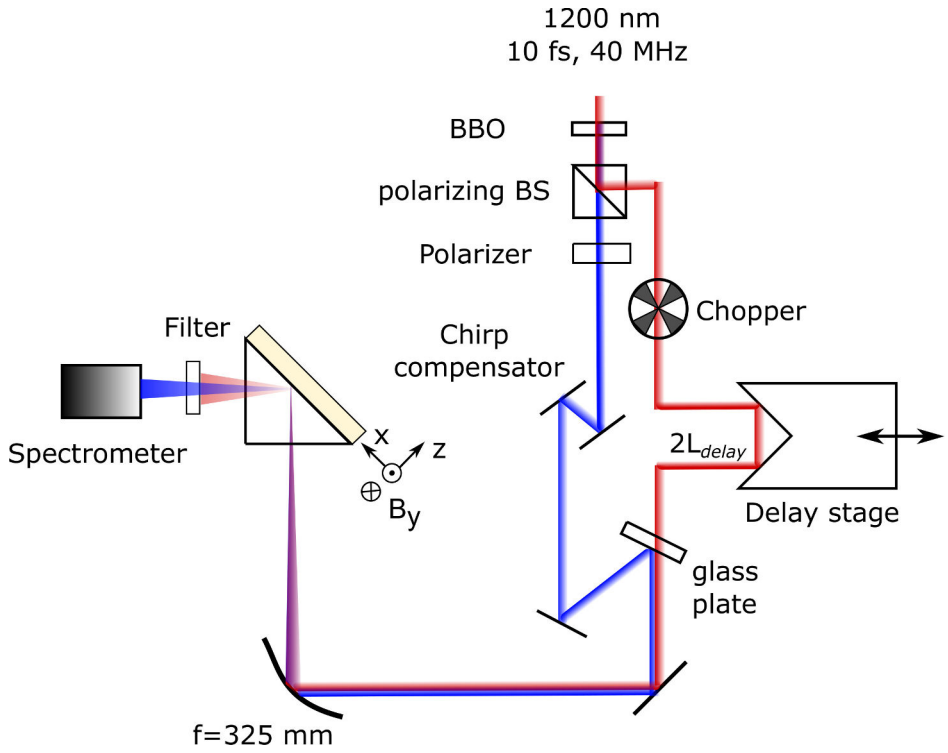

Figure 5.9 – A simplified scheme for the cross-correlation of mSHG on the Kretschmann geometry.

5.3.2 Results and discussion

The interference patterns of the mSHG signal and the reference local oscillator at different time delay are shown in Fig. 5.10. The interference fringes are clear. Red

and blue colors illustrate the two opposite magnetizations of the mSHG $E_{2\omega}(t, \pm M)$. At a fixed delay between the fundamental and local oscillator fields, the observed spectrally-resolved interference shows no visible dependence on the direction of the external magnetic field. It can be concluded that there exists no noticeable structure in the phase spectrum of the mSHG signal. This result refers to a phase-matched broadband nature of the generation process of the nonlinear signal and suggests no significant spectral interference arising from the propagation aspects of the SPP within the multilayer structure. No phase shift when the magnetization is reversed, i.e. $\varphi_{+M} = \varphi_{-M}$, means zero phase difference $\varphi = 0$ between the magnetic SH field $E_{2\omega}^{mag}$ and the non-magnetic one $E_{2\omega}^{nm}$. This result is controversial. There is also a possibility that the noise signal is too high that the real phase shift could not be recovered.

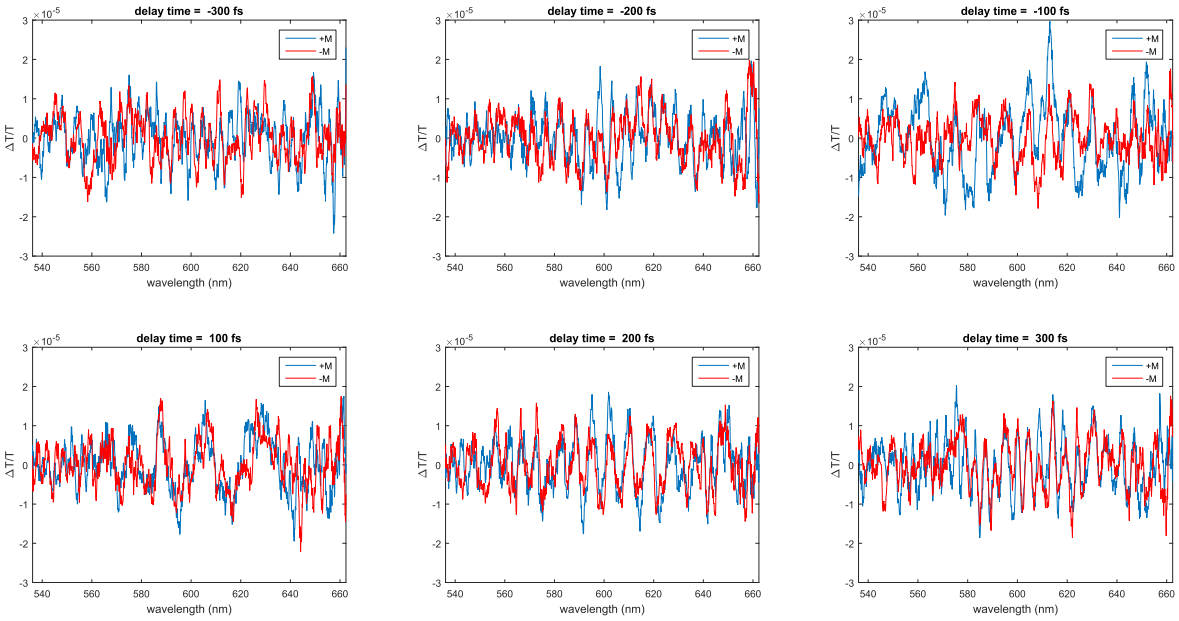

Figure 5.10 – Spectrally-resolved linear cross-correlation of a reference wave with the mSHG signal for opposite directions of the magnetization M (red and blue lines) at different fixed time delays.

5.4 Conclusion

In this chapter I have described an explorative part of collaborative research, aiming at understanding the transition from the static to the dynamic regime in nonlinear magneto-plasmonics. The power dependence of the SH magnetic contrast has been discussed, which is believed to be a result of the demagnetization of the structure. The effect is obvious as it manifests itself as a 50% reduction of the SH magnetic contrast dropping even further at high pump intensities. Although the microscopic picture of this power dependence is still unclear, it is an effect worth exploring.

The magnetically controlled femtosecond time-resolved auto-correlation measurements in Kretschmann configuration display the dynamic magnetic contrast exceeding

70% at the angle of incidence 46°, where the mSHG output at one orientation of magnetization is almost suppressed. At this angle we have observed a qualitative change in shape of the auto-correlation function and a huge magnetic contrast. These effects are related to the excitation of SPP(2ω) by the nonlinear phase-matching mechanism discussed in chapter 3. However, further modelling of autocorrelation functions should be conducted in order to quantify the contribution of SPP(2ω) to the autocorrelation function. Spectrally-resolved cross-correlation of the mSHG provides measurable interference fringes in the spectral domain. The difficulties of this experiment were related to the compensation of dispersion of the reference field in the prism and to obtain spatial and temporal overlap between the generated SH field and reference fields. Though the experiment was successful in the sense that spectral interference fringes displayed dynamics on ultrafast time scales, and also resolving the phase of the mSHG from a hybrid multilayer structures, the expected phase shift between the magnetic (odd) and non-magnetic (even) SH fields could not be observed. Sophisticated interferometric phase reconstruction algorithms should be applied in order to discriminate physical effects from the artifacts of spatio-temporal interferometric measurements in such a complex experimental geometry.

Chapter 6

Summary and conclusion

Surface electromagnetic (EM) waves propagating along metallic interfaces and excited in various geometries enabling their phase-matched excitation, can enhance the linear and nonlinear magneto-optical effects in metal-ferromagnet multilayer structures. This work investigates the phenomena in the nonlinear regime, specifically the influence of surface EM waves on the magnetization-induced SHG in Kretschmann configuration combined with the geometry of the transverse magneto-optical Kerr effect. A goniometric magneto-optical setup has been constructed to discriminate between distinct surface waves excited by different phase-matching conditions. The thesis focuses on three aspects of the nonlinear magneto-optics mediated by the surface EM waves:

- nonlinear magneto-plasmonics on Kretschmann metal/ferromagnet multilayers
- nonlinear Wood's anomaly on periodic arrays of nickel nanodimers
- nonlinear magneto-plasmonics in the dynamic regime

Performed on different systems or different measurement setups, these studies help to identify the role of nonlinear phase-matching conditions for surface EM waves at the double SHG frequency and to quantify their contributions to the giant magnetic SHG contrast.

Nonlinear magneto-plasmonics in metal-ferromagnet multilayers

In order to excite SPPs at a free surface of metal-ferromagnet multilayers, the conventional Kretschmann geometry was employed. In various experiments, the excitation efficiency of different SPP modes has been represented by the Lorentzian function accounting for their phase-matched excitation. In this work, the Lorentzian function $L(\theta)$ has been derived theoretically from the coupling of the SH polarization to SPP's electric field at the double-frequency. It is also demonstrated that the SH magnetic contrast can provide direct experimental access to the parameters of $L(\theta)$, especially the one related to the nonlinear coupling of SPP(2ω). This finding allowed us to propose a reverse approach, which estimates the nonlinear SPP coupling efficiency by the experimental method.

The role of linear and nonlinear SPPs was clarified while inspecting angular-dependencies of the mSHG output and the magnetic contrast. The linear SPP(ω) enhances the fundamental electric field, and thus results in the characteristic peak in the angular dependence of the SHG in metallic thin films. The nonlinear SPP(2ω) is excited via the nonlinear phase-matching condition and is detected through the interference of its radiative emission into the glass prism with the non-resonant SH sources located at various interfaces. The pronounced dip in the angular dependence of the SH emission results from the destructive interference between the non-resonant SH and the resonant SPP(2ω) fields. A comparative study of two distinct metal-ferromagnet systems, i.e. the trilayer of (5 nm)Au/ (10 nm)Co/ (15-25-35 nm)Ag and the bilayer of (20-30-40 nm)Au/ (30 nm)Co, suggests that the SPP-enhanced SH emission in the trilayer is typically an order-of-magnitude stronger than that in the bilayer. It means that the field enhancement of the linear SPP in the trilayer Au/Co/Ag is larger. In terms of magnetic properties, the SH magnetic contrast in the bilayer Au/Co is influenced both by the linear and the nonlinear SPPs. On the other hand, the position of the maximum SH magnetic contrast in the trilayer Au/Co/Ag is determined by the nonlinear SPPs, while its magnitude depends on the fundamental field strength, and is enhanced by the linear SPP(ω). It thus suggests that nonlinear magneto-optical signals can be tuned by tailoring SPP fields. Indeed, it has been demonstrated in this work that varying the thickness of the plasmonic (silver) layer in trilayers can boost the SH magnetic contrast up to 60%, almost twise as large as compared to the previously reported values. Therefore, the trilayer Au/Co/Ag represents a physical system for nonlinear-optical proof-of-concept studies such as the modulation of light at the nano-scale by an external magnetic field.

Nonlinear Wood's anomaly on nickel nanodimers

In periodic structures where the surface filling factor of metals is low, the phased-matched excitation of surface EM waves is based on the principle of Wood's anomaly, which occur when a diffraction order emerges along the surface of the grating. The possibility to co-excite linear and nonlinear Wood's anomalies is governed by the ratio between the optical wavelength λ and the periodicity of the grating Λ. For example, the linear and the second-harmonic Wood's anomaly can be excited simultaneously when $\Lambda \geq \lambda/2$, but only the SH diffraction anomaly at the order $m_{nl} = -1$ is allowed when $\lambda/4 < \Lambda < \lambda/2$. In this work, Wood's anomalies have been investigated in a rectangular 2D-array of nickel nanodimers with different sizes of a unit cell: one is greater and the other is less than half of the fundamental wavelength.

The results show that the linear Wood's anomaly has little influence on the SH yield, which differs significantly from the linear SPP in metallic multilayers and from Wood's anomaly on plasmonic gratings [4]. However, similar to the SPP case, the magnetic contrast shows a fingerprint of the SH Wood's anomaly excited through the nonlinear phase-matching mechanism. The nonlinear-optical framework is further sketched for the analysis of periodic structures with smaller periodicities and argue that nonlinear-optical and magneto-optical effects can be utilized as a highly sensitive measure of the efficiency of diffraction gratings in periodic arrays of magnetic nanoparticles.

The nickel nanodimers structures were originally designed to observe any possible contributions of localized surface plasmon resonance (LSPR), which can be excited in the dimer gap within the spectral range 500-1000 nm, to the SH yield and magnetic contrast. Under specific conditions, this mode can be coupled to the Wood's anomalies forming a hybrid mode called surface lattice resonance (SLR). At the current stage, it was difficult to disentangle these effects from the mSHG signal, except for a minor change in the effective refractive index of the surface EM waves. The idea of hybrid magneto-plasmonic SLRs might be revised in future in experiments with a different sample design. Another outlook is to excite nonlinear Wood's anomaly in different meta-surfaces, such as periodic arrays of sub-wavelength holes, where one can speculate about the phenomenon of magnetization-controlled extraordinary optical transmission in the nonlinear regime.

Nonlinear magneto-plasmonics in the dynamic regime

While previous sections describe the interaction of surface EM waves and their nonlinear magneto-optical effects in the time-integrated regime, this section takes the first step to explore the dynamics of the phenomena. It is an exploratory part of the thesis, where open questions could inspire further investigations.

Pump-power dependence of SH magnetic contrast in metal-ferromagnet multilayers at power levels indicates on the ultrafast demagnetization. This finding urges us to investigate the dynamics of magneto-plasmonic interactions. Using the Au/Co/Ag trilayer system as the second-order nonlinear medium, the auto-correlation of ultrashort pulses has been measured in Kretschmann configuration. In this case, two sources of SHG must be considered, which are non-resonant and resonant to the nonlinear SPP field propagating at metal-air interface. Between them, the resonant source exhibits the magnetization dependence, due to the ferromagnet layer buried within the SPP field skin depth. The intensity auto-correlation trace shows a normal Gaussian shape at the non-resonant angles of incidence. However, the complexity escalates when radiative SPP(2ω) are excited and interfere with the non-resonant SH fields. The presence of long-living wings in the auto-correlation function is the result of this interference. Interestingly, the central peak in the auto-correlation can be completely suppressed upon the reversal of the magnetization. The fact that the nonlinear magnetic contrast observed on short timescales is reduced by approximately a factor of two in the time-integrated measurements implies the coherent nature of the mSHG signal.

Carried out on the same sample, the spectrally resolved cross-correlation measurements attempt to retrieve the phase of mSHG in the dynamic regime. The broadband nature of the generation process of the nonlinear signal suggests no significant spectral interference arising from the propagation aspects of the SPP within the multilayer structure, in agreement with preliminary experimental results. However, more detailed studies and application of sophisticated interferometric phase reconstruction algorithms are necessary to confirm these premature conclusions.

Appendix A

Technical specifications

A.1 Verify film thickness using ATIR

When the precise thickness of each layer is unknown, one can compare the angular dependences of reflectivity calculated by Matrix-Transfer-Method (MTM) and measured experimentally to estimate the relative thickness between layers. Using this method, the relative thickness of each sample can be estimated as in Table. A.1.

Samples	**Estimation using MTM**
(15nm)Ag/(5nm)Co/(5nm)Au	(15nm)Ag/(10nm)Co/(4nm)Au
(25nm)Ag/(5nm)Co/(5nm)Au	(28nm)Ag/(10nm)Co/(5nm)Au
(35nm)Ag/(5nm)Co/(5nm)Au	(41nm)Ag/(9nm)Co/(5nm)Au

Table A.1 – Employing the known database for the refractive indices of gold, silver (Johnson and Christy 1972) and cobalt (Artem 1968), the relative thicknesses between different layers in the hybrid structure can be estimated. The right column is the designed thicknesses of the samples, but they were not confirmed by electron microscope. The left column is the approximation of the relative thickness by fitting the experimental angular dependence of reflectivity using MTM.

Inversely, knowing the thickness of the layer, one can use this SPP-based ellipsometry to estimate the effective dielectric function of the multilayer. The limits of the method are polarization (p-polarized light) and the wavelength of the incident radiation (infrared spectral range), where the SPP-dip is distinguishable.

A.2 Technical specifications

Properties	**Output 1560 nm**	**Output 780 nm**
Average power at output (mW)	390	170
Estimated energy per pulse (mJ)	9.75×10^{-6}	4.25×10^{-6}
Peak power (mW)	9.75×10^{7}	4.25×10^{7}
Number of photons per pulse	7.65×10^{10}	1.67×10^{10}
Typical beam diameter (mm)	3.5	1.2
Focused by lens f=+300 mm, beam waist (μm)	170	250
Focused by lens f=+300 mm, spot area (mm^2)	2.28×10^{-2}	4.84×10^{-2}
Focused by lens f=+300 mm, fluence ($\mu J/cm^2$)	42.8	8.78
Focused by lens f=+300 mm, Rayleigh length (μm)	170	250

Table A.2 – Techinical specification of Toptica fiber laser for nonlinear magneto-plasmonic setup

Settings	**Optimized value**
PMT voltage supply	900 V
Trigger frequency	4450 Hz
Gates per counting period	5000
Gate width	80 μs
Gate A delay	45 μs
Gate B delay	155 μs
Channel discrimination level	-2 mV
Trigger discrimination level	100 mV

Table A.3 – Technical specifications of the photon counting regime

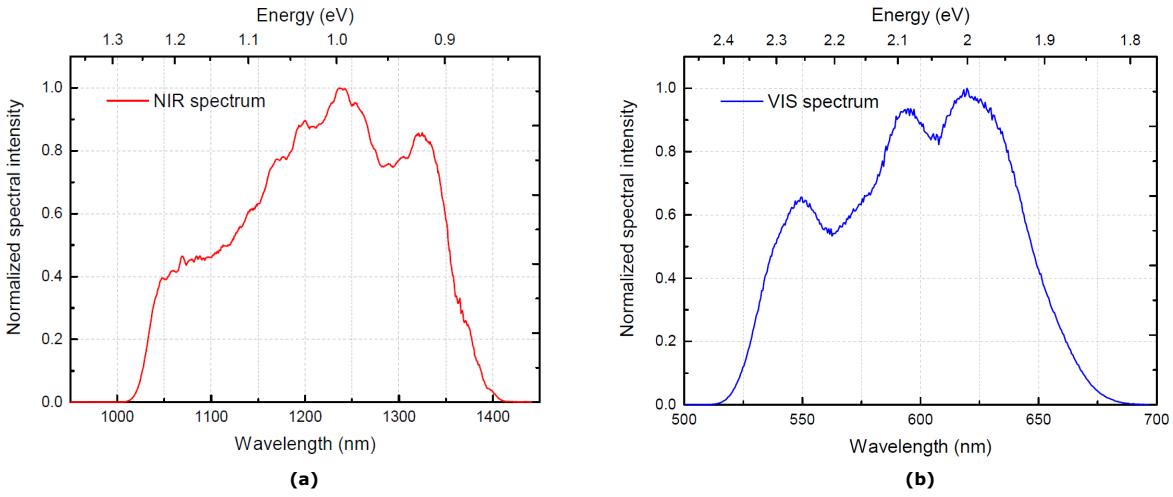

Figure A.1 – Spectra of the fundamental and reference (local oscillator) radiations for the cross-correlation experiment in Konstanz.

Appendix B

Third-harmonic generation in metallic thin film

B.1 Estimation of Third-harmonic generation (THG) in Au film

Pulse energy of the laser

The laser source at 1560 nm have an average power of 100 mW after the mirrors, half waveplate and filter. This corresponds to a pulse energy:

$$E_p = \frac{\text{Average power}}{\text{Repetition rate}} = \frac{P_{ave}}{f_{rep}} = \frac{100 \times 10^{-3}\ W}{4 \times 10^7\ Hz} = 2.5 \times 10^{-9}\ J \tag{B.1}$$

Peak power of a pulse:

$$P_1 = \frac{\text{Pulse energy}}{\text{Pulse duration}} = \frac{E_p}{\tau} = \frac{2.5 \times 10^{-9}\ J}{100\ fs} = 2.5 \times 10^4\ W \tag{B.2}$$

Note that each photon at 1560 nm has energy of $1.27 \times 10^{-19}\ J$ or $0.795\ eV$, number of photons per pulse:

$$N_{p1} = \frac{E_p}{E_\omega} = \frac{2.5 \times 10^{-9}\ J}{1.27 \times 10^{-19}\ J} = 1.96 \times 10^{10}\ \text{photons/pulse} \tag{B.3}$$

Focusing condition

Under the focused Gaussian condition, one can estimate the beam waist, or focal spot size, $2w_0$ according to:

$$2w_0 = \frac{4\lambda}{\pi}.\frac{F}{D} \tag{B.4}$$

where $\lambda = 1.56 \times 10^{-6}\ m$, focal length of the lens $F = 300\ mm$ and beam diameter before the lens $D = 4\ mm$. The beam waist radius is hence $w_0 = 74.5\ \mu m$

Field strength of incident pump

Intensity of the incident beam at the focal spot can be calculated from the power:

$$I_1 = \frac{P_1}{\pi w_0^2} = \frac{2.5 \times 10^4\ W}{\pi \times (74.5 \times 10^{-6}\ m)^2} = 1.43 \times 10^{12}\ W/m^2 \tag{B.5}$$

The field strength A_1 of incident field relates to the intensity via $I = 2n\epsilon_0 c|A|^2$.

$$|A_1| = \sqrt{\frac{I_1}{2n_1\epsilon_0 c}} = 5 \times 10^6\ V/m \tag{B.6}$$

where refractive index of gold at 1560 nm: $n_1 = 0.53005 + 10.82i$ (Johnson & Christy), vacuum permittivity $\epsilon_0 = 8.854 \times 10^{-12}\ F/m$ and speed of light $c = 3 \times 10^8\ m/s$.

Field strength of THG

The field strength of THG estimated according to Eq. 2.10.11 [1]:

$$A_3 = \frac{i3\omega}{2n_3 c}\chi^{(3)} A_1^3 J_3(\Delta k, z_0, z) \tag{B.7}$$

where $\Delta k = 3k_1 - k_3$ and $J_3(\Delta k, z_0, z)$ represents the integration of complex amplitude $A_3(z)$ over the length of interaction region from z_0 to z. In the limiting case where the interaction region is much smaller than the depth of focal region $|z_0|, |z| \ll b = \frac{2\pi w_0^2}{\lambda}$, J_3 reduces to:

$$J_3(\Delta k, z_0, z) = \int_{z_0}^{z} e^{i\Delta k z} dz' = \frac{e^{i\Delta k z} - e^{i\Delta k z_0}}{i\Delta k} \tag{B.8}$$

or:

$$|J_3(\Delta k, z_0, z)|^2 = L^2 \mathrm{sinc}^2(\frac{\Delta k L}{2}) \tag{B.9}$$

where $L = z - z_0$ is length of the interaction region.

For the perfect phase matching, $\Delta k = 0$, $\mathrm{sinc}(\frac{\Delta k L}{2}) = 1$ and thus $J_3(\Delta k, z_0, z) = L$. So Eq. B.7 becomes:

$$A_3 = \frac{i3\omega}{2n_3 c}\chi^{(3)} A_1^3 L \tag{B.10}$$

Taking the interaction region L as the skin depth of the field upon reflection $L \approx 10\ nm$, refractive index of gold at 520 nm: $n_3 = 0.63512 + 2.0721i$ (Johnson & Christy), $\omega = \frac{2\pi c}{\lambda_1} = 1.21 \times 10^{15}\ rad/s$ and $\chi^{(3)} = 2.45 \times 10^{-19}\ m^2/V^2$, we have $|A_3| = 0.85\ V/m$

[1] Chapter 2.10, Nonlinear Optics 3rd edition, R. W. Boyd

Power of THG

Again, intensity of THG:

$$I_3 = 2n_3\epsilon_0 c|A_3|^2 = 2.4 \times 10^{-3}\ W/m^2 \tag{B.11}$$

The beam waist radius of THG is $\sqrt{3}$ times smaller than that of the incident beam. So $w_3 = w_0/\sqrt{3} = 43\ \mu m$. The THG intensity comes from a region having radius w_3, hence the power of THG pulse:

$$P_3 = I_3\pi w_3^2 = 1.41 \times 10^{-11}\ W \tag{B.12}$$

If we consider that the duration of THG pulse is similar to that of the excitation pulse, i.e. 100 fs, then the THG pulse energy:

$$E_{p3} = P_3 \times \tau = 1.41 \times 10^{-11}\ W \times 10^{-13}\ s = 1.41 \times 10^{-24}\ J \tag{B.13}$$

This is equivalent to the THG average power:

$$P_{ave3} = E_{p3} \times f_{rep} = 1.41 \times 10^{-24}\ W \times 40\ MHz = 5.66 \times 10^{-17}\ W \tag{B.14}$$

Or numbers of photons per second (not per pulse):

$$N_3 = \frac{P_{ave3}}{E_{3\omega}} = \frac{5.66 \times 10^{-17}\ W}{3.82 \times 10^{-19}\ J} = 143 \text{ photons/s} \tag{B.15}$$

Sensitivity of detector

The photomultiplier tube (PMT) Hamamatsu R955 has quantum efficiency at 520 nm 13%, meaning that the number of photoelectrons per second: $0.13 \times N_3 = 19$ electrons/s.

Besides, the PMT has an indication for the photon-limited signal to noise ratio (SNR), called equivalent noise input (ENI), which refers to the amount of light in watts to produce $SNR = 1$. For PMT R955, $ENI = 1.3 \times 10^{-16}\ W$. Compare to Eq. B.14, power of incident light is less than the noise level and can't be detected.

However, a paper [2] states that THG signal can be enhanced by $10^3 - 10^4$ times when the excitation beam is coupled to SP modes. So around the angle of resonance, we might detect some THG photons.

Unit of nonlinear susceptibility $\chi^{(n)}$

The Gaussian unit (e.s.u.) can be converted to SI units (MKS) via:

$$\chi^{(2)}(m/V) = \frac{4\pi}{3 \times 10^4}\ \chi^{(2)}(e.s.u.) \tag{B.16}$$

$$\chi^{(3)}(m^2/V^2) = \frac{4\pi}{(3 \times 10^4)^2}\ \chi^{(3)}(e.s.u.) \tag{B.17}$$

[2] T. Y. F. Tsang, Optics Letter Vol. 21, No. 4, 1996

B.2 Third-harmonic magneto-plasmonics

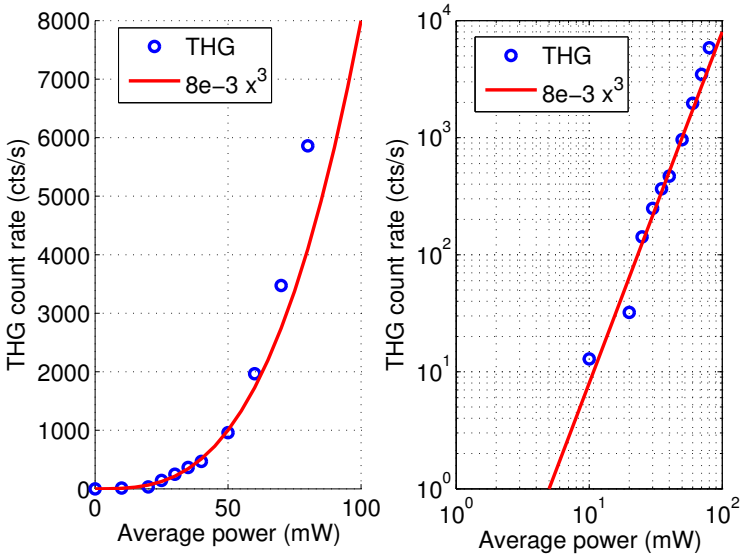

Figure B.1 – Power dependence of the THG in the trilayer (5 nm) Au/(10 nm) Co/(15 nm) Ag at angle of incidence 43.9° in the normal scale (left) and in logarithmic scale (right).

The measurement of third-harmonic magneto-plasmonics was performed on trilayer (5 nm) Au/(10 nm) Co/(15 nm) Ag, where the SPP-induced SH emission was the largest among the three samples of trilayer structure. The fundamental radiation was provided by the MaiTai laser, center wavelength 1560 nm, repetition rate 80 MHz, pulse duration < 120 fs. The setup is similar to the one described in Fig. 3.3, except that the low-pass filter in front of the PMT was changed to a band-pass filter FB520 (Thorlabs) in order to select third-harmonic emission at 520 nm.

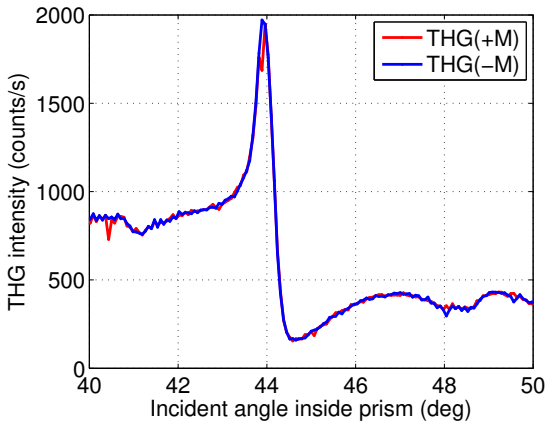

Figure B.2 – The angular dependence of the THG in the trilayer (5 nm) Au/(10 nm) Co/(15 nm) Ag at opposite magnetizations ($\pm M$).

The fluence dependence of the THG is plotted in Fig. B.1. The dependence $I_{3\omega} \propto I_{\omega}^{3}$ was preserved upto the average power of 80 mW, proving that the detected signal is the TH emission. Next, the scans over the angles of incidence were performed under an external magnetic field B_y applied perpendicular to the plane of incidence. The THG signals for the two opposite magnetizations are presented in Fig. B.2. As expected from the estimation above, the SPP-enhanced peak at angle 43.9° is an order-of-magnitude higher than the noise level, and is detectable by the registered setup. Similar to the case of the SHG peak, this characteristic peak is the result of the fundamental field enhancement of the linear SPP(ω). Recalling that the TH output involves both the bulk and the surface contributions, the nonlinear SPP(3ω) takes effect within a volumn skin depth. Thus, describing plasmonic THG would be more complicating than the SH case. We also note that there is no visible magnetization-induced variations of THG. As the bulk could be the dominant source of TH emission, the thin cobalt layer might not generate sufficient magnetic contrast. However, if the cobalt layer is too thick, the optical loss will increase accordingly, limiting the effect of the radiative SPP.

Abbreviations

ATIR	attenuated total internal reflection
EM	electromagnetic
BBO	Beta barium borate
BS	beam splitter
LSPR	localized surface plasmon resonance
mSHG	magnetization-induced second-harmonic generation
MOKE	magneto-optical Kerr effect
PMT	photomultiplier tube
SH	second-harmonic
SHG	second-harmonic generation
SLR	surface lattice resonance
SP	surface plasmon
SPP	surface-plasmon polariton
SPR	surface plasmon resonance
TE	transverse electric
TM	transverse magnetic

List of publications

- Tom Seifert, Ngoc Minh Tran, Oliver Gueckstock, Seyed Mohammedreza Rouzegar, Lukas Nadvornik, Samridh Jaiswal, Gerhard Jakob, Vasily V. Temnov, Markus Muenzenberg, Martin Wolf, Mathias Klaeui and Tobias Kampfrath: **Terahertz spectroscopy for all-optical spintronic characterization of the spin-Hall-effect metals Pt, W and $Cu_{80}Ir_{20}$**; *(Special Issue on Spin-caloritronic) J. Phys. D: Appl. Phys.* **51***(36), 364003(2018), pp8*; [DOI: 10.1088/1361-6463/aad536]; Publication Date (Online/WEB): Jul 23, 2018.

- Ngoc-Minh Tran, Ioan-Augustin Chioar, Aaron Stein, Alexandr Alekhin, Vincent Juvé, Gwenaëlle Vaudel, Ilya Razdolski, Vassilios Kapaklis and Vasily Temnov: **Observation of the nonlinear Wood's anomaly on magneto-photonic crystals of nickel nanodimers**; *Physics Review B* (submitted); [arXiv:1811.04189]

- Ngoc-Minh Tran, Christian Traum, Alexandr Alekhin, Dmitry A. Kuzmin, Vincent Juvé, Gwenaëlle Vaudel, Ilya Razdolski, Denys Makarov, Denis Seletskiy and Vasily V. Temnov: **Resonantly enhanced nonlinear magneto-plasmonic interactions in hybrid metal-ferromagnet multilayer structures**; *Physics Review Applied* (in preparation).

Bibliography

[1] R W Wood. On a remarkable case of uneven distribution of light in a diffraction grating spectrum. *Proceedings of the Physical Society of London*, 18(1):269, 1902.

[2] Stefan Alexander Maier. *Plasmonics: fundamentals and applications*. Springer Science & Business Media, 2007.

[3] Gaspar Armelles, Alfonso Cebollada, Antonio García-Martín, and María Ujué González. Magnetoplasmonics: combining magnetic and plasmonic functionalities. *Advanced Optical Materials*, 1(1):10–35, 2013.

[4] H. J. Simon, D. E. Mitchell, and J. G. Watson. Optical second-harmonic generation with surface plasmons in silver films. *Phys. Rev. Lett.*, 33:1531–1534, Dec 1974.

[5] Markus B Raschke, Samuel Berweger, and Joanna M Atkin. Ultrafast and nonlinear plasmon dynamics. In *Plasmonics: Theory and Applications*, pages 237–281. Springer, 2013.

[6] Ilya Razdolski, Denys Makarov, Oliver G. Schmidt, Andrei Kirilyuk, Theo Rasing, and Vasily V. Temnov. Nonlinear surface magnetoplasmonics in kretschmann multilayers. *ACS Photonics*, 3(2):179–183, 2016.

[7] Vasily V Temnov, Ilya Razdolski, Thomas Pezeril, Denys Makarov, Denis Seletskiy, Alexey Melnikov, and Keith A Nelson. Towards the nonlinear acousto-magneto-plasmonics. *Journal of Optics*, 18(9):093002, 2016.

[8] P Haefner, E Luck, and E Mohler. Magnetooptical properties of surface plasma waves on copper, silver, gold, and aluminum. *physica status solidi (b)*, 185(1):289–299, 1994.

[9] Yakov M. Strelniker and David J. Bergman. Transmittance and transparency of subwavelength-perforated conducting films in the presence of a magnetic field. *Phys. Rev. B*, 77:205113, May 2008.

[10] B. Sepúlveda, J. B. González-Díaz, A. García-Martín, L. M. Lechuga, and G. Armelles. Plasmon-induced magneto-optical activity in nanosized gold disks. *Phys. Rev. Lett.*, 104:147401, Apr 2010.

[11] Juan Bautista González-Díaz, Antonio García-Martín, G Armelles, José Miguel García-Martín, C Clavero, Alfonso Cebollada, RA Lukaszew, JR Skuza, DP Kumah, and Roy Clarke. Surface-magnetoplasmon nonreciprocity effects in noble-metal/ferromagnetic heterostructures. *Physical Review B*, 76(15):153402, 2007.

[12] Vasily V Temnov, Gaspar Armelles, Ulrike Woggon, Dmitry Guzatov, Alfonso Cebollada, Antonio Garcia-Martin, Jose-Miguel Garcia-Martin, Tim Thomay, Alfred Leitenstorfer, and Rudolf Bratschitsch. Active magneto-plasmonics in hybrid metal–ferromagnet structures. *Nature Photonics*, 4(2):107, 2010.

[13] Diana Martín-Becerra, Juan B González-Díaz, Vasily V Temnov, Alfonso Cebollada, Gaspar Armelles, Tim Thomay, Alfred Leitenstorfer, Rudolf Bratschitsch, Antonio García-Martín, and María Ujué González. Enhancement of the magnetic modulation of surface plasmon polaritons in au/co/au films. *Applied Physics Letters*, 97(18):183114, 2010.

[14] Jorge F Torrado, Juan B González-Díaz, Antonio García-Martín, and Gaspar Armelles. Unraveling the relationship between electromagnetic field intensity and the magnetic modulation of the wave vector of coupled surface plasmon polaritons. *New Journal of Physics*, 15(7):075025, 2013.

[15] V. V. Pavlov, G. Tessier, C. Malouin, P. Georges, A. Brun, D. Renard, P. Meyer, J. Ferré, and P. Beauvillain. Observation of magneto-optical second-harmonic generation with surface plasmon excitation in ultrathin au/co/au films. *Applied Physics Letters*, 75(2):190–192, 1999.

[16] VI Belotelov, IA Akimov, M Pohl, VA Kotov, S Kasture, AS Vengurlekar, Achanta Venu Gopal, DR Yakovlev, AK Zvezdin, and M Bayer. Enhanced magneto-optical effects in magnetoplasmonic crystals. *Nature Nanotechnology*, 6(6):370, 2011.

[17] Jessie Yao Chin, Tobias Steinle, Thomas Wehlus, Daniel Dregely, Thomas Weiss, Vladimir I. Belotelov, Bernd Stritzker, and Harald Giessen. Nonreciprocal plasmonics enables giant enhancement of thin-film faraday rotation. *Nat. Commun.*, 4:1599, 2013.

[18] Alexander L Chekhov, Alexander I Stognij, Takuya Satoh, Tatiana V Murzina, Ilya Razdolski, and Andrzej Stupakiewicz. Surface plasmon-mediated nanoscale localization of laser-driven sub-terahertz spin dynamics in magnetic dielectrics. *Nano letters*, 18(5):2970–2975, 2018.

[19] T W Ebbesen, H J Lezec, H F Ghaemi, T Thio, and P A Wolff. Extraordinary optical transmission through sub-wavelength hole arrays. *Nature*, 391:667, feb 1998.

[20] Henri J Lezec, A Degiron, E Devaux, RA Linke, L Martin-Moreno, FJ Garcia-Vidal, and TW Ebbesen. Beaming light from a subwavelength aperture. *Science*, 297(5582):820–822, 2002.

[21] William L Barnes, Alain Dereux, and Thomas W Ebbesen. Surface plasmon subwavelength optics. *nature*, 424(6950):824, 2003.

[22] Henri J Lezec and Tineke Thio. Diffracted evanescent wave model for enhanced and suppressed optical transmission through subwavelength hole arrays. *Optics express*, 12(16):3629–3651, 2004.

[23] C Genet and TW Ebbesen. Light in tiny holes. In *Nanoscience And Technology: A Collection of Reviews from Nature Journals*, pages 205–212. World Scientific, 2010.

[24] GA Wurtz, W Hendren, R Pollard, R Atkinson, L Le Guyader, Andrei Kirilyuk, Th Rasing, II Smolyaninov, and AV Zayats. Controlling optical transmission through magneto-plasmonic crystals with an external magnetic field. *New Journal of Physics*, 10(10):105012, 2008.

[25] Jorge F Torrado, Juan B González-Díaz, María U González, Antonio García-Martín, and Gaspar Armelles. Magneto-optical effects in interacting localized and propagating surface plasmon modes. *Optics express*, 18(15):15635–15642, 2010.

[26] G Ctistis, E Papaioannou, P Patoka, J Gutek, P Fumagalli, and M Giersig. Optical and magnetic properties of hexagonal arrays of subwavelength holes in optically thin cobalt films. *Nano letters*, 9(1):1–6, 2008.

[27] Evangelos Th Papaioannou, Vassilios Kapaklis, Emil Melander, Björgvin Hjörvarsson, Spiridon D Pappas, Piotr Patoka, Michael Giersig, Paul Fumagalli, Antonio Garcia-Martin, and Georgios Ctistis. Surface plasmons and magneto-optic activity in hexagonal ni anti-dot arrays. *Optics express*, 19(24):23867–23877, 2011.

[28] Emil Melander, Erik Östman, Janine Keller, Jan Schmidt, Evangelos Th Papaioannou, Vassilios Kapaklis, Unnar B Arnalds, Blanca Caballero, Antonio García-Martín, Juan Carlos Cuevas, et al. Influence of the magnetic field on the plasmonic properties of transparent ni anti-dot arrays. *Applied Physics Letters*, 101(6):063107, 2012.

[29] I Razdolski, DG Gheorghe, Emil Melander, Björgvin Hjörvarsson, P Patoka, AV Kimel, A Kirilyuk, E Th Papaioannou, and Th Rasing. Nonlocal nonlinear magneto-optical response of a magnetoplasmonic crystal. *Physical Review B*, 88(7):075436, 2013.

[30] Vasily V Temnov. Ultrafast acousto-magneto-plasmonics. *Nature Photonics*, 6(11):728, 2012.

[31] Viktor Shalagatskyi. *Ultrafast acoustics in hybrid and magnetic structures*. PhD thesis, Université du Maine, 2015.

[32] Tobias Kampfrath, Marco Battiato, Pablo Maldonado, G Eilers, J Nötzold, Sebastian Mährlein, V Zbarsky, F Freimuth, Y Mokrousov, S Blügel, et al. Terahertz spin current pulses controlled by magnetic heterostructures. *Nature nanotechnology*, 8(4):256, 2013.

[33] Alexandr Alekhin, Ilya Razdolski, Nikita Ilin, Jan P. Meyburg, Detlef Diesing, Vladimir Roddatis, Ivan Rungger, Maria Stamenova, Stefano Sanvito, Uwe Bovensiepen, and Alexey Melnikov. Femtosecond spin current pulses generated by the nonthermal spin-dependent seebeck effect and interacting with ferromagnets in spin valves. *Phys. Rev. Lett.*, 119:017202, Jul 2017.

[34] Tom Seifert, S Jaiswal, U Martens, J Hannegan, Lukas Braun, Pablo Maldonado, F Freimuth, A Kronenberg, J Henrizi, I Radu, et al. Efficient metallic spintronic emitters of ultrabroadband terahertz radiation. *Nature photonics*, 10(7):483–488, 2016.

[35] Tom Seifert, Ngoc Minh Tran, Oliver Gueckstock, Seyed Mohammedreza Rouzegar, Lukas Nadvornik, Samridh Jaiswal, Gerhard Jakob, Vasily V Temnov, Markus Muenzenberg, Martin Wolf, et al. Terahertz spectroscopy for all-optical spintronic characterization of the spin-hall-effect metals pt, w and cu _{80} ir _{20}. *arXiv preprint arXiv:1805.02193*, 2018.

[36] H. A. Wierenga, M. W. J. Prins, D. L. Abraham, and Th. Rasing. Magnetisatization-induced optical second-harmonic generation: A probe for interface magnetism. *Phys. Rev. B*, 50:1282–1285, Jul 1994.

[37] Ru-Pin Pan, HD Wei, and YR Shen. Optical second-harmonic generation from magnetized surfaces. *Physical Review B*, 39(2):1229, 1989.

[38] Andrei Kirilyuk and Theo Rasing. Magnetization-induced-second-harmonic generation from surfaces and interfaces. *JOSA B*, 22(1):148–167, 2005.

[39] J Reif, JC Zink, C-M Schneider, and J Kirschner. Effects of surface magnetism on optical second harmonic generation. *Physical review letters*, 67(20):2878, 1991.

[40] Robert W Boyd. *Nonlinear optics*. Elsevier, 2003.

[41] Yuen-Ron Shen. The principles of nonlinear optics. *New York, Wiley-Interscience, 1984, 575 p.*, 1984.

[42] Tony F Heinz. Second-order nonlinear optical effects at surfaces and interfaces. In *Modern Problems in Condensed Matter Sciences*, volume 29, pages 353–416. Elsevier, 1991.

[43] T. M. Crawford, T. J. Silva, C. W. Teplin, and C. T. Rogers. Subnanosecond magnetization dynamics measured by the second-harmonic magneto-optic kerr effect. *Applied Physics Letters*, 74(22):3386–3388, 1999.

[44] Wei Zheng, Aubrey T Hanbicki, Berry T Jonker, and Gunter Lüpke. Surface plasmon-enhanced transverse magnetic second-harmonic generation. *Optics express*, 21(23):28842–28848, 2013.

[45] Baptiste Auguié and William L. Barnes. Collective resonances in gold nanoparticle arrays. *Physical Review Letters*, 101(14):1–4, 2008.

[46] V G Kravets, F Schedin, and A N Grigorenko. Extremely narrow plasmon resonances based on diffraction coupling of localized plasmons in arrays of metallic nanoparticles. *Physical Review Letters*, 101(8):87403, aug 2008.

[47] Wei Zhou and T. W. Odom. Tunable subradiant lattice plasmons by out-of-plane dipolar interactions. *Nature Nanotech*, 6:423–427, 2011.

[48] Robert Czaplicki, Antti Kiviniemi, Janne Laukkanen, Joonas Lehtolahti, Markku Kuittinen, and Martti Kauranen. Surface lattice resonances in second-harmonic generation from metasurfaces. *Optics letters*, 41(12):2684–2687, 2016.

[49] Lior Michaeli, Shay Keren-Zur, Ori Avayu, Haim Suchowski, and Tal Ellenbogen. Nonlinear surface lattice resonance in plasmonic nanoparticle arrays. *Physical review letters*, 118(24):243904, 2017.

[50] Dmitry A. Kuzmin, Igor V. Bychkov, Vladimir G. Shavrov, and Vasily V. Temnov. Plasmonics of magnetic and topological graphene-based nanostructures. *Nanophotonics*, 7(3):597–611, 2018.

[51] AA Grunin, AG Zhdanov, AA Ezhov, EA Ganshina, and AA Fedyanin. Surface-plasmon-induced enhancement of magneto-optical kerr effect in all-nickel subwavelength nanogratings. *Applied Physics Letters*, 97(26):261908, 2010.

[52] Wei Zhou, Yi Hua, Mark D Huntington, and Teri W Odom. Delocalized lattice plasmon resonances show dispersive quality factors. *The journal of physical chemistry letters*, 3(10):1381–1385, 2012.

[53] M Kataja, TK Hakala, Aleksi Julku, MJ Huttunen, Sebastiaan van Dijken, and Päivi Törmä. Surface lattice resonances and magneto-optical response in magnetic nanoparticle arrays. *Nature communications*, 6:7072, 2015.

[54] AV Chetvertukhin, AA Grunin, AV Baryshev, TV Dolgova, H Uchida, M Inoue, and AA Fedyanin. Magneto-optical kerr effect enhancement at the wood's anomaly in magnetoplasmonic crystals. *Journal of Magnetism and Magnetic Materials*, 324(21):3516–3518, 2012.

[55] Valentina Bonanni, Stefano Bonetti, Tavakol Pakizeh, Zhaleh Pirzadeh, Jianing Chen, Josep Nogués, Paolo Vavassori, Rainer Hillenbrand, Johan Åkerman, and Alexandre Dmitriev. Designer magnetoplasmonics with nickel nanoferromagnets. *Nano letters*, 11(12):5333–5338, 2011.

[56] Irina Zubritskaya, Kristof Lodewijks, Nicolò Maccaferri, Addis Mekonnen, Randy K Dumas, Johan Åkerman, Paolo Vavassori, and Alexandre Dmitriev. Active magnetoplasmonic ruler. *Nano letters*, 15(5):3204–3211, 2015.

[57] Nanfang Yu and Federico Capasso. Flat optics with designer metasurfaces. *Nature Materials*, 13:139–150, 2014.

[58] Alexander V. Kildishev, Alexandra Boltasseva, and Vladimir M. Shalaev. Planar photonics with metasurfaces. *Science*, 339(6125), 2013.

[59] Robert W Wood. Anomalous diffraction gratings. *Physical Review*, 48(12):928, 1935.

[60] Daniel Maystre. Theory of wood's anomalies. In *Plasmonics*, pages 39–83. Springer, 2012.

[61] Max Born and Emil Wolf. *Principles of Optics: Electromagnetic Theory of Propagation, Interference and Diffaction of Light*. Pergamon Press, 1959.

[62] Lukas Novotny and Bert Hecht. *Principles of nano-optics*. Cambridge university press, 2012.

[63] Hendrik Antoon Lorentz. *The Theory of Electrons and Its Applications to the Phenomena of Light and Radiant Heat: A Course of Lectures Delivered in Columbia University, New York, in March and April, 1906*, volume 29. Columbia University Press, 1909.

[64] IF Almog, MS Bradley, and V Bulovic. The lorentz oscillator and its applications. *Massachusetts Institute of Technology*, 2011.

[65] Paul Drude. *The theory of optics*. Courier Corporation, 1925.

[66] A. Sommerfeld. Zur elektronentheorie der metalle auf grund der fermischen statistik. *Zeitschrift für Physik*, 47(1):1–32, Jan 1928.

[67] N. Del Fatti, C. Voisin, M. Achermann, S. Tzortzakis, D. Christofilos, and F. Vallée. Nonequilibrium electron dynamics in noble metals. *Phys. Rev. B*, 61:16956–16966, Jun 2000.

[68] Davy Gérard and Stephen K Gray. Aluminium plasmonics. *Journal of Physics D: Applied Physics*, 48(18):184001, 2014.

[69] C. Guo, G. Rodriguez, A. Lobad, and A. J. Taylor. Structural phase transition of aluminum induced by electronic excitation. *Phys. Rev. Lett.*, 84:4493–4496, May 2000.

[70] Nick N. Lepeshkin, Aaron Schweinsberg, Giovanni Piredda, Ryan S. Bennink, and Robert W. Boyd. Enhanced nonlinear optical response of one-dimensional metal-dielectric photonic crystals. *Phys. Rev. Lett.*, 93:123902, Sep 2004.

[71] J.-Y. Bigot, V. Halté, J.-C. Merle, and A. Daunois. Electron dynamics in metallic nanoparticles. *Chemical Physics*, 251(1):181 – 203, 2000.

[72] Honghua U Yang, Jeffrey D'Archangel, Michael L Sundheimer, Eric Tucker, Glenn D Boreman, and Markus B Raschke. Optical dielectric function of silver. *Physical Review B*, 91(23):235137, 2015.

[73] Zhenlin Wang, Che Ting Chan, Weiyi Zhang, Naiben Ming, and Ping Sheng. Three-dimensional self-assembly of metal nanoparticles: Possible photonic crystal with a complete gap below the plasma frequency. *Physical Review B*, 64(11):113108, 2001.

[74] P. B. Johnson and R. W. Christy. Optical constants of the noble metals. *Phys. Rev. B*, 6:4370–4379, Dec 1972.

[75] Pablo G Etchegoin, EC Le Ru, and M Meyer. An analytic model for the optical properties of gold. *The Journal of chemical physics*, 125(16):164705, 2006.

[76] MA Ordal, LL Long, RJ Bell, SE Bell, RR Bell, RW Alexander, and CA Ward. Optical properties of the metals al, co, cu, au, fe, pb, ni, pd, pt, ag, ti, and w in the infrared and far infrared. *Applied optics*, 22(7):1099–1119, 1983.

[77] J-Y Bigot, J-Y Merle, O Cregut, and A Daunois. Electron dynamics in copper metallic nanoparticles probed with femtosecond optical pulses. *Physical review letters*, 75(25):4702, 1995.

[78] C-K Sun, F Vallée, LH Acioli, EP Ippen, and JG Fujimoto. Femtosecond-tunable measurement of electron thermalization in gold. *Physical Review B*, 50(20):15337, 1994.

[79] JG Fujimoto, JM Liu, EP Ippen, and N Bloembergen. Femtosecond laser interaction with metallic tungsten and nonequilibrium electron and lattice temperatures. *Physical Review Letters*, 53(19):1837, 1984.

[80] Christophe Voisin, Natalia Del Fatti, Dimitris Christofilos, and Fabrice Vallée. Ultrafast electron dynamics and optical nonlinearities in metal nanoparticles, 2001.

[81] Daniel Gall. Electron mean free path in elemental metals. *Journal of Applied Physics*, 119(8):085101, 2016.

[82] Stefan Visnovsky. *Optics in magnetic multilayers and nanostructures.* CRC Press, 2006.

[83] Ml Freiser. A survey of magnetooptic effects. *IEEE Transactions on magnetics*, 4(2):152–161, 1968.

[84] John Kerr. Xliii. on rotation of the plane of polarization by reflection from the pole of a magnet. *The London, Edinburgh, and Dublin Philosophical Magazine and Journal of Science*, 3(19):321–343, 1877.

[85] Michael Faraday. On the magnetization of light and the illumination of magnetic lines of force. *Philosophical Transactions of the Royal Society of London*, 136:1–20, 1846.

[86] Karl Heinz Bennemann. *Non-linear optics in metals*. Number 98. Oxford University Press, 1998.

[87] J Zak, ER Moog, C Liu, and SD Bader. Universal approach to magneto-optics. *Journal of Magnetism and Magnetic Materials*, 89(1-2):107–123, 1990.

[88] JA Armstrong, N Bloembergen, J Ducuing, and PS Pershan. Interactions between light waves in a nonlinear dielectric. *Physical review*, 127(6):1918, 1962.

[89] B Koopmans, AM Janner, HA Wierenga, Th Rasing, GA Sawatzky, and F van der Woude. Separation of interface and bulk contributions in second-harmonic generation from magnetic and non-magnetic multilayers. *Applied Physics A*, 60(2):103–111, 1995.

[90] P Guyot-Sionnest and YR Shen. Bulk contribution in surface second-harmonic generation. *Physical Review B*, 38(12):7985, 1988.

[91] Victor Mizrahi and John E Sipe. Phenomenological treatment of surface second-harmonic generation. *JOSA B*, 5(3):660–667, 1988.

[92] Jerry I Dadap, Jie Shan, and Tony F Heinz. Theory of optical second-harmonic generation from a sphere of centrosymmetric material: small-particle limit. *JOSA B*, 21(7):1328–1347, 2004.

[93] Fu Xiang Wang, Francisco J. Rodríguez, Willem M. Albers, Risto Ahorinta, J. E. Sipe, and Martti Kauranen. Surface and bulk contributions to the second-order nonlinear optical response of a gold film. *Physical Review B*, 80(23):233402, 2009.

[94] G. S. G. S. Krinchik and V. A. Artem'ev. Magneto-optical properties of ni, co, and fe in the ultraviolet visible, and infrared parts of the spectrum. *Sov. Phys. JETP*, 26:1080–1085, 1968.

[95] H RAETHER. Surface plasmons on smooth and rough surfaces and on gratings. *Springer Tract in Modern Physics*, 111, 1988.

[96] Bo E Sernelius. *Surface modes in physics*. John Wiley & Sons, 2011.

[97] Erwin Kretschmann and Heinz Raether. Radiative decay of non radiative surface plasmons excited by light. *Zeitschrift für Naturforschung A*, 23(12):2135–2136, 1968.

[98] Andreas Otto. Excitation of nonradiative surface plasma waves in silver by the method of frustrated total reflection. *Zeitschrift für Physik A Hadrons and nuclei*, 216(4):398–410, 1968.

[99] Stefano Palomba and Lukas Novotny. Nonlinear excitation of surface plasmon polaritons by four-wave mixing. *Phys. Rev. Lett.*, 101:056802, Aug 2008.

[100] J. J. Burke, G. I. Stegeman, and T. Tamir. Surface-polariton-like waves guided by thin, lossy metal films. *Phys. Rev. B*, 33:5186–5201, Apr 1986.

[101] Nicolai B. Grosse, Jan Heckmann, and Ulrike Woggon. Nonlinear plasmon-photon interaction resolved by k-space spectroscopy. *Phys. Rev. Lett.*, 108:136802, Mar 2012.

[102] Jonathan J. Foley IV, Hayk Harutyunyan, Ralu Divan Daniel Rosenmann, Gary P. Wiederrecht, and Stephen K. Gray. When are surface plasmon polaritons excited in the kretschmann-raether configuration? *Sci. Rep.*, 5:9929, 2015.

[103] T Y Tsang. Surface-plasmon-enhanced third-harmonic generation in thin silver films. *Optics letters*, 21(4):245–247, 1996.

[104] Jiřı Homola, Ivo Koudela, and Sinclair S Yee. Surface plasmon resonance sensors based on diffraction gratings and prism couplers: sensitivity comparison. *Sensors and Actuators B: Chemical*, 54(1-2):16–24, 1999.

[105] Jiří Homola and Marek Piliarik. Surface plasmon resonance (spr) sensors. In *Surface plasmon resonance based sensors*, pages 45–67. Springer, 2006.

[106] Pochi Yeh. *Optical waves in layered media*, volume 61. Wiley-Interscience, 2005.

[107] Pochi Yeh, Amnon Yariv, and Chi-Shain Hong. Electromagnetic propagation in periodic stratified media. i. general theory. *JOSA*, 67(4):423–438, 1977.

[108] Zdenek Knittl. *Optics of thin films: an optical multilayer theory*, volume 1. Wiley London:, 1976.

[109] Charles Fabry. Theorie et applications d'une nouvelle methods de spectroscopie intereferentielle. *Ann. Chim. Ser. 7*, 16:115–144, 1899.

[110] Diana Martín-Becerra, Vasily V Temnov, Tim Thomay, Alfred Leitenstorfer, Rudolf Bratschitsch, Gaspar Armelles, Antonio García-Martín, and María Ujué González. Spectral dependence of the magnetic modulation of surface plasmon polaritons in noble/ferromagnetic/noble metal films. *Physical Review B*, 86(3):035118, 2012.

[111] Yu Gong, Alan G. Joly, Dehong Hu, Patrick Z. El-Khoury, and Wayne P. Hess. Ultrafast imaging of surface plasmons propagating on a gold surface. *Nano Letters*, 15(5):3472–3478, 2015.

[112] Martin van Exter and Ad Lagendijk. Ultrashort surface-plasmon and phonon dynamics. *Physical review letters*, 60(1):49, 1988.

[113] Vasily V Temnov, Keith Nelson, Gaspar Armelles, Alfonso Cebollada, Tim Thomay, Alfred Leitenstorfer, and Rudolf Bratschitsch. Femtosecond surface plasmon interferometry. *Optics express*, 17(10):8423–8432, 2009.

[114] Dmitri K. Gramotnev and Sergey I. Bozhevolnyi. Plasmonics beyond the diffraction limit. *Nature Photonics*, 4(2):83–91, 2010.

[115] Martti Kauranen, Anatoly V Zayats, Rm Osgood, L Cao, Nc Panoiu, W Fan, S Zhang, Kj Malloy, and Srj Brueck. Nonlinear Plasmonics. *Focus*, 6(October):737–748, 2009.

[116] John C. Quail and H. J. Simon. Second-harmonic generation from a silver grating with surface plasmons. *J. Opt. Soc. Am. B*, 5(2):325–329, Feb 1988.

[117] PHILIPPE Leturcq, J-M Dorkel, ANDRZEJ Napieralski, and ERIC Lachiver. A new approach to thermal analysis of power devices. *IEEE Transactions on Electron Devices*, 34(5):1147–1156, 1987.

[118] R. H. M. Groeneveld, R. Sprik, and A. Lagendijk. Ultrafast Relaxation of Electrons Probed by Sureface Plasmons at a Thin Sliver Film, 1990.

[119] Vasily V. Temnov, Christoph Klieber, Keith A. Nelson, Tim Thomay, Vanessa Knittel, Alfred Leitenstorfer, Denys Makarov, Manfred Albrecht, and Rudolf Bratschitsch. Femtosecond nonlinear ultrasonics in gold probed with ultrashort surface plasmons. *Nature Communications*, 4:1466–1468, 2013.

[120] Atsushi Kubo, Ken Onda, Hrvoje Petek, Zhijun Sun, Yun S Jung, and Hong Koo Kim. Femtosecond imaging of surface plasmon dynamics in a nanostructured silver film. *Nano letters*, 5(6):1123–1127, 2005.

[121] Atsushi Kubo, Niko Pontius, and Hrvoje Petek. Femtosecond microscopy of surface plasmon polariton wave packet evolution at the silver/vacuum interface. *Nano letters*, 7(2):470–475, 2007.

[122] JG Fujimoto, JM Liu, EP Ippen, and N Bloembergen. Femtosecond laser interaction with metallic tungsten and nonequilibrium electron and lattice temperatures. *Physical Review Letters*, 53(19):1837, 1984.

[123] S. D. Brorson, J. G. Fujimoto, and E. P. Ippen. Femtosecond electronic heat-transport dynamics in thin gold films. *Physical Review Letters*, 59(17):1962–1965, 1987.

[124] H. Petek and S. Ogawa. Femtosecond time-resolved two-photon photoemission studies of electron dynamics in metals. *Progress in Surface Science*, 56(4):239–310, 1997.

[125] E Beaurepaire, J-C Merle, A Daunois, and J-Y Bigot. Ultrafast spin dynamics in ferromagnetic nickel. *Physical review letters*, 76(22):4250, 1996.

[126] Jean-Yves Bigot, Mircea Vomir, and Eric Beaurepaire. Coherent ultrafast magnetism induced by femtosecond laser pulses. *Nature Physics*, 5(7):515, 2009.

[127] Andrei Kirilyuk, Alexey V Kimel, and Theo Rasing. Ultrafast optical manipulation of magnetic order. *Reviews of Modern Physics*, 82(3):2731, 2010.

[128] Jean-Claude Diels, Wolfgang Rudolph, Paul F Liao, and Paul Kelley. Ultrashort laser pulse phenomena: fundamentals, techniques, and applications on a femtosecond time scale, optics and photonics. *Academic, New York*, 1996.